Abdelrahman Sayed Sayed Emam Ibrahim

Risk Aware Control of Underwater Snake Robots in Confined Environments

Master's thesis in Marine Technology
Supervisor: Asgeir J. Sørensen
Co-supervisor: Ingrid Bouwer Utne
May 2023

Master's thesis

NTNU
Norwegian University of Science and Technology
Faculty of Engineering
Department of Marine Technology

NTNU
Norwegian University of
Science and Technology

Abdelrahman Sayed Sayed Emam Ibrahim

Risk Aware Control of Underwater Snake Robots in Confined Environments

Master's thesis in Marine Technology
Supervisor: Asgeir J. Sørensen
Co-supervisor: Ingrid Bouwer Utne
May 2023

Norwegian University of Science and Technology
Faculty of Engineering
Department of Marine Technology

NTNU
Norwegian University of
Science and Technology

"If you're going to try, go all the way. Otherwise, don't even start. This could mean losing girlfriends, wives, relatives and maybe even your mind. It could mean not eating for three or four days. It could mean freezing on a park bench. It could mean jail. It could mean derision. It could mean mockery –isolation. Isolation is the gift. All the others are a test of your endurance, of how much you really want to do it. And, you'll do it, despite rejection and the worst odds. And it will be better than anything else you can imagine. If you're going to try, go all the way. There is no other feeling like that. You will be alone with the gods, and the nights will flame with fire. You will ride life straight to perfect laughter. It's the only good fight there is."

Charles Bukowski, Factotum

MASTER OF TECHNOLOGY THESIS DEFINITION (30 SP)

Name of the candidate: Abdelrahman Sayed Sayed Emam Ibrahim

Field of study: Marine Cybernetics

Thesis title (Norwegian): Risikobevisst kontroll av undervanns slangeroboter i trange omgivelser

Thesis title (English): Risk Aware Control of Underwater Snake Robots in Confined Environments

Background

To reach new ocean horizons, we must learn from nature. The growing interest in ocean discovery imposes a need for inspection and intervention in confined and demanding environments. Underwater confined environments, such as shipwrecks and sunken caves, present unique challenges for exploration and study. Underwater snake robots, like Eely which is a snake robot from Eelume, are an ideal option for these environments due to their slender shape and ability to change body configurations. This allows to perform a variety of tasks including inspections, maintenance, repair, and to access areas that would be inaccessible to traditional underwater vehicles. However, operation of Eely in such environments imposes demanding requirements on the system, as it must deal with uncertain and unstructured environments, extreme environmental conditions, and reduced navigational capabilities.

This thesis will investigate how to control such robot by using Proportional–Integral–Derivative (PID) and Fractional Order PID (FOPID) controllers to obtain a robust controller for the system. Moreover, simulations are performed to evaluate the capabilities of Eely in comparison to a conventional ROV. Furthermore, a risk assessment study is used to assess the risks of losing Eely during confined environments scenarios. Relevant data are collected to perform a quantitative risk analysis. The model looks upon almost Eely's entire system to avoid potential risks.

Scope of Work

1. Perform a background and literature review to provide information and relevant references on:
   - Modelling and control of snake robotics
   - Fractional Order PID (FOPID)
   - Risk assessment methods for underwater vehicles

   Write a list with abbreviations and definitions of terms and symbols, relevant to the literature study and project report.

2. Propose a risk model based on BN to assess the risk of losing Eely for two mission scenarios

3. Implementing a Fractional Order PID (FOPID) to Eely and evaluating its performance

4. Build upon the simulator developed as part of TMR4510

5. Validate the proposed controllers in the simulator

6. Validate the results of the simulator and comparing it with actual field trials

7. Writing two conference papers, one on risk assessment of Eely and the second on control of Eely

Specifications

The student shall at startup provide a maximum 2-page week plan of work for the entire project period, with main activities and milestones. This should be updated on a monthly basis in agreement with supervisor.

Every weekend throughout the project period, the candidate shall send a status email to the supervisor and co-advisors, providing two brief bulleted lists: 1) work done recent week, and 2) work planned to be done next week.

The scope of work may prove to be larger than initially anticipated. By the approval from the supervisor, described topics may be deleted or reduced in extent without consequences with regard to grading.

The candidate shall present personal contribution to the resolution of problems within the scope of work. Theories and conclusions should be based on mathematical derivations and logic reasoning identifying the steps in the deduction.

The report shall be organized in a logical structure to give a clear exposition of background, problem/research statement, design/method, analysis, and results. The text should be brief and to the point, with a clear language. Rigorous mathematical deductions and illustrating figures are preferred over lengthy textual descriptions. The report shall have font size 11 pts., and it is not expected to be longer than 70 A4-pages, 100 B5-pages, from introduction to conclusion, unless otherwise agreed. It shall be written in English (preferably US) and contain the elements: Title page, project definition, preface (incl. description of help, resources, and internal and external factors that have affected the project process), acknowledgement, abstract, list of symbols and acronyms, table of contents, introduction (project background/motivation, objectives, scope and delimitations, and contributions), technical background and literature review, problem formulation or research question(s), method/design/development, results and analysis, conclusions with recommendations for further work, references, and optional appendices. Figures, tables, and equations shall be numerated. The contribution of the candidate shall be clearly and explicitly described, and material taken from other sources shall be clearly identified. Work from other sources shall be properly acknowledged using quotations and a Harvard citation style (e.g. natbib Latex package). The work is expected to be conducted in an honest and ethical manner, without any sort of plagiarism and misconduct, which is taken very seriously by the university and will result in consequences. NTNU can use the results freely in research and teaching by proper referencing, unless otherwise agreed.

The thesis shall be submitted with an electronic copy to the main supervisor and department according to NTNU administrative procedures. The final revised version of this thesis definition shall be included after the title page. Computer code, pictures, videos, data, etc., shall be included electronically with the report.

Start date: 05 January, 2023   **Due date:**   31 May, 2023

Supervisor: Professor Asgeir J. Sørensen
Co-advisor(s):   Professor Ingrid Bouwer Utne

Signatures:

Preface

This master thesis was written at the Norwegian University of Science and Technology (NTNU), Department of Marine Technology (IMT) and Centre for Autonomous Marine Operations and Systems (AMOS) in Trondheim between January and May 2023 as the final fulfilment of the Erasmus Mundus Joint Master Degree in Marine and Maritime Intelligent Robotics Study track 2: Safe autonomous subsea operations (Norway, NTNU).

This work builds upon the work done in the course Marine Control Systems, Specialization Project TMR4510. The work was done independently between September and December 2022 under the supervision of Prof. Asgeir J. Sørensen and co-advisor Markus Fossdal. The work was based on research about underwater snake robots control and assessing the risks associated with confined environments operations, mainly Eely underwater snake robot from Eelume. Simulations were performed using Plankton open-source simulator and ROS2. Eely model used for simulation was coded by Bendik Jørgensen, with modifications by Christopher Janjua and me.

The influence to carry out this thesis started in the summer of 2022 when I was hosted at Explore Team, Laboratoire d'informatique, de robotique et de microélectronique de Montpellier LIRMM as an intern working with A.Prof. Lionel Lapierre on the topic of underwater karst exploration. Through the work of this thesis, I have been under the supervision of Prof. Asgeir J. Sørensen and Prof. Ingrid Bouwer Utne. Their guidance and assistance have been of great help both in terms of collaboration and support.

The thesis is written as a collection of two scientific papers and a summary about them. The first paper, titled "*Risk Assessment of an Autonomous Underwater Snake Robot in Confined Operations*", is to be published at OCEANS 2023 Limerick, Ireland, and the second paper, titled "*Robust Altitude Controller for Underwater Snake Robot using Fractional Order PID Controller (FOPID)*", is a draft paper for future submission.

Acknowledgements

Abstract

The growing interest in ocean discovery imposes a need for inspection and intervention in confined and demanding environments. To tackle these demanding environments, articulated underwater robots, such as Eely, with their slender shape and adaptable body configurations, have emerged as a viable solution. However, operating Eely in such environments presents a set of complex challenges. It must navigate through uncertain and unstructured surroundings, withstand extreme environmental conditions, and overcome limited navigational capabilities.

This thesis addresses these challenges by proposing a Bayesian approach to assess the risks associated with the loss of Eely during mission scenarios. The primary goal of this thesis is to enhance Eely's performance and increase the likelihood of mission success. In addition, an altitude controller based on a nonlinear Fractional Order PID (FOPID) controller is proposed. This controller aims to regulate and stabilize the altitude of Eely underwater snake robot.

Through simulations, the proposed controller is thoroughly evaluated to demonstrate its robustness and effectiveness in controlling the altitude of Eely. The simulations provide valuable insights into the controller's performance in diverse underwater conditions, including scenarios with uncertain and unstructured environments. By leveraging the benefits of the FOPID controller, Eely showed improved altitude regulation capabilities, enabling it to navigate through challenging terrains with enhanced precision and stability. The simulation results are compared to the results obtained from field experiments in which similar tests are conducted.

Moreover, the Bayesian risk assessment approach serves as a valuable tool in quantifying the potential risks and uncertainties associated with Eely's missions. By assessing and mitigating these risks, the proposed approach contributes to increasing the overall reliability and safety of Eely's operations in demanding underwater environments.

In short, this thesis presents a comprehensive study focused on the challenges faced by Eely in confined and demanding underwater environments. By combining a Bayesian risk assessment methodology with a sophisticated FOPID altitude controller, this research aims to improve Eely's performance, enhance mission success rates, and ensure the successful exploration and intervention in sophisticated underwater landscapes. The findings and insights obtained from this study have significant implications for the future development and deployment of underwater snake robots in challenging environments.

Contents

List of Figures

List of Tables

Nomenclature

List of Abbreviations

AUV	Autonomous Underwater Vehicle
BBN	Bayesian belief network
$Bio - V$	Bio-inspired Vehicle
BN	Bayesian Network
CB	Center of Buoyancy
CO	Center of Origin
DDS	Data Distribution Service protocol
DN	Decision Network
DOF	Degree of Freedom
DP	Dynamic Positioning
DVL	Doppler Velocity Logger
$FOPID$	Fractional Order PID controller
$GNSS$	Global navigation satellite system
GPS	Global Positioning System
GV	Glider Vehicle
$HAZID$	Hazard Identification
$HiPAP$	High Precision Acoustic Positioning
$HROV$	Hybrid Remotely Operated Vehicle
NED	North-East-Down
OOI	Object of interest
PHA	Preliminary Hazard Analysis

PID	Proportional Integral Derivative
RGB	Red Green Blue
ROV	Remotely Operated Vehicle
UHI	Underwater Hyper-spectral Imaging
USV	Unmanned Surface Vehicle
UTC	Coordinated Universal Time
UUV	Unmanned Underwater Vehicles
$YAML$	YAML ain't markup language

List of Lowercase Symbols

$\dot{e}$	Derivative of the error
η	position and orientation in the NED frame
η_d	Vehicle desired pose in NED frame
λ	FOPID integrator order
μ	FOPID differentiator order
ν	velocity in the BODY frame
ϕ	roll angle
ψ	yaw angle
τ_c	Control torque
θ	pitch angle
$\{b\}$	BODY frame
$\{n\}$	NED frame
$c(.)$	cos
e	Error
$e(t')$	Time integral of the error
$f(e)$	Nonlinear function
f_{A_x}	Force due to added mass in x-direction
f_{A_y}	Force due to added mass in y-direction
$f_{D_x}^{II}$	Forces due to non-linear drag in the x-direction
$f_{D_x}^{I}$	Forces due to linear drag in the x-direction
$f_{D_y}^{II}$	Forces due to non-linear drag in the y-direction

$f_{D_y}^I$ Forces due to linear drag in the y-direction

$s(.)$ sin

$t(.)$ tan

v velocity

w_{nb}^b BODY fixed angular velocities

List of Uppercase Symbols

K_d Derivative gain

K_i Integral gain

K_p Proportional gain

R Rotation matrix

S Skew-symmetric matrix

$V_{r_x}^{\text{link}}$ Link relative velocity vector in the x-direction

$V_{r_y}^{\text{link}}$ Link relative velocity vector in the y-direction

V_x, V_y Ocean current velocity expressed in the inertial frame

$\dot{\Theta}_{nb}$ Euler rate vector

Θ_{nb} Vector containing Euler angles

J_Θ Jacobian matrix

$J_\Theta(\eta)$ Jacobian matrix relating linear and angular velocities in NED and BODY frames

R_b^n Rotation matrix from BODY to NED frame

$T(\Theta_{nb})$ Transformation matrix relates BODY fixed angular velocities and Euler rates

Chapter 1

Introduction

This chapter will give an introduction to the motivation and background, objectives, research questions, methodology and main contributions.

1.1 Background and Motivation

1.1.1 Underwater Vehicles

The development of underwater robots has a long history. In the 1990s, over 46 models of Autonomous Underwater Robots (AUVs) were created for various missions [1]. Today, there are many different types of underwater robots that have been developed for both commercial and scientific purposes. Underwater robots can be divided into several categories based on their appearance and function:

1. **Unmanned Surface Vehicles (USVs)** are deployed on the water surface and are able to receive global positioning system (GPS) signals for localization and navigation. Since their range of operation is two-dimensional, the control challenges they face may be simpler. USVs can also take advantage of wind or wave energy for propulsion. However, environmental disturbances and ships traffic can impact their performance and pose significant scientific and technological challenges.

2. **Remotely Operated Vehicles (ROVs)** are able to operate underwater and communicate with an operator via an umbilical cable, which allows for real-time control. ROVs can receive power, data, and control commands through this link. The first ROV models were created for use in the oil and gas industry for deep-sea missions. With the increasing use of underwater robots in science, many smaller ROV models have been developed for use in shallow water. However, the operating range of ROVs is limited by the length of the umbilical cable and the cumbersome link it creates.

3. **Autonomous Underwater Vehicles (AUVs)** do not have an umbilical link and are able to operate autonomously. As a result, they are able to perform a limited range of missions. AUVs are often divided into two categories: torpedo-shaped and cubic-shaped AUVs. Torpedo-shaped AUVs are typically under-actuated and

designed for long-range missions, while cubic-shaped AUVs are often fully or over-actuated and useful for short-range missions. The two types of AUVs also differ in their hovering and pivot steering capabilities and operating speed range.

4. **Hybrid Remotely Operated Vehicles (HROVs)** are a hybrid of ROVs and AUVs, but not fully so. HROVs are able to perform manipulation tasks like ROVs, but integrated into an AUV (without a tether). However, the poor quality of the acoustic communication link complicates the teleportation process and reduces its performance.

5. **Glider Vehicles (GVs)** use buoyancy variation and depth control for propulsion. Attitude is controlled through the adaptive redistribution of mass or external control surfaces. The advantages of GVs include their ability to perform long-range missions and low-cost operations.

6. **Bio-inspired Vehicles (Bio-Vs)** take inspiration from biological forms, which have been optimized through natural selection. Many Bio-Vs have been developed in recent years to mimic the shapes of living organisms. Bio-Vs are able to maneuver by changing their shape, taking advantage of the flexibility inherent in natural systems.

In general, controlling an underwater system involves managing six degrees of freedom (roll, pitch, yaw, surge, sway, and heave), but many applications only require control of three or four of these degrees of freedom, depending on the capabilities of the system and the goals of the mission. The number and placement of actuators on an underwater vehicle determines whether it is underactuated, iso-actuated, or over-actuated. This classification depends on the number and position of the actuators and the degrees of freedom that they can affect.

1.1.2 Underwater Robots in Confined Environments

Underwater confined environments, such as shipwrecks and sunken caves, present unique challenges for exploration and study. These environments often have limited access points and tight spaces, making it difficult for divers and underwater vehicles to enter and maneuver. In addition, the water pressure at these depths can be immense, requiring specialized equipment and techniques to safely operate in these environments.

Despite these challenges, studying underwater confined environments can yield valuable information about the history and geology of the area, as well as provide habitat for unique and fragile marine life. For example, shipwrecks can serve as artificial reefs, providing a rich and diverse ecosystem for marine organisms to thrive.

To explore and study these environments, divers and underwater vehicles must be equipped with specialized tools and equipment, such as lights, cameras, and instruments for measuring water quality and other conditions. In addition, careful planning and coordination is required to ensure the safety of the divers and the preservation of the environment.

The first known use of an underwater robot in a confined environment was reported in 1967, when the IFP (Institut Francais du Pétrole) used the Télénaute to explore the Fontaine de Vaucluse down to a depth of 106 meters. This marked an important milestone in the use of underwater robotics for exploring and studying karst environments [2].

One of the most advanced underwater systems for exploring karst environments is DEPTHX shown in Figure 1.1(left), developed by the University American Consortium in 2005 with funding from NASA [3]. DEPTHX is designed for autonomous exploration of unexplored environments, and is capable of generating high-resolution 3D maps, collecting biological samples, and returning to its starting point [4].

Another example is the Unexmin project shown in Figure 1.1(right) [5], an European initiative that aims to design and develop autonomous systems for exploring and mapping abandoned flooded mines. This project focuses on adapting deep-sea robotics technology for use in these environments, as well as on interpreting the geoscientific data collected.
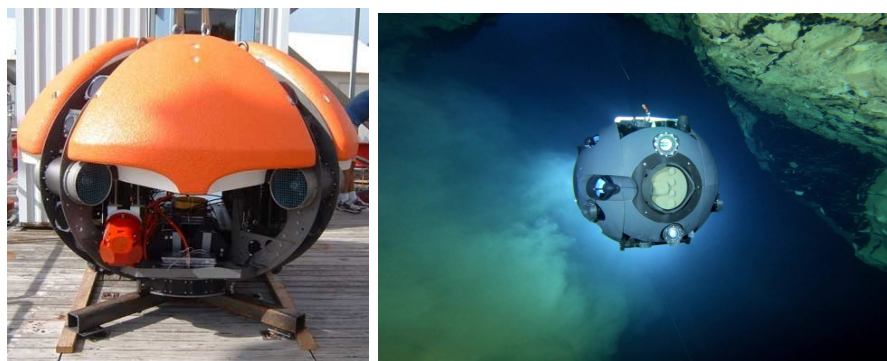
Figure 1.1: DEPTHX (left) and Unexmin (right)

The Aleyin project [6], led by the University of Montpellier, has also developed two systems for exploring karst environments: the ROV Ulysse shown in Figure 1.2(left) and the manned system Navscoot shown in Figure 1.2(right). Ulysse is equipped with a profiling sonar and a suite of navigation sensors, while Navscoot uses the same sensors mounted on an underwater scooter. These systems have been used to create 3D acoustic topographies and partial photogrammetric reconstructions
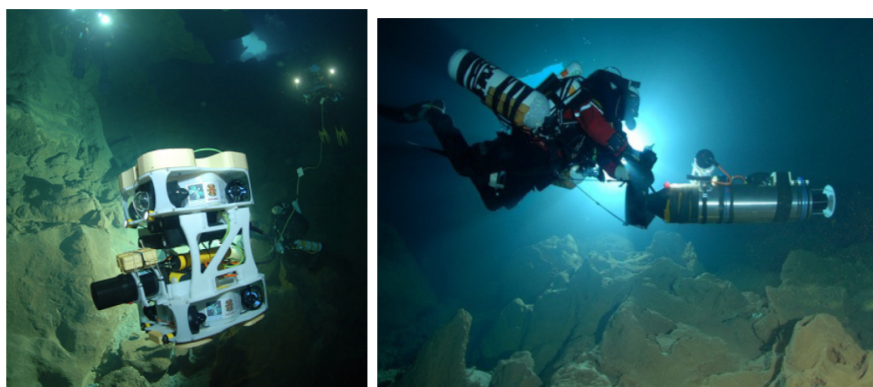
Figure 1.2: Ulysse (left) and Navscoot Underwater scooter (right)

1.1.3 Underwater Snake Robots

Underwater snake robots combine the advantages of several types of underwater vehicles. They have the range of Autonomous Underwater Vehicles (AUVs), the ability to access challenging areas like small ROVs, and the intervention capabilities of ROVs shown in Figure 1.3. These robots are inspired by the way snakes move and are able to navigate

virtually any terrain with ease. They are composed of links connected by actuated joints and are essentially robotic arms that can produce locomotion by actuating the joints to create a periodic body wave motion, allowing them to swim like a biological snake. Additionally, the snake robot's slender and flexible body allows it to cover large distances and perform inspections, maintenance, and repair in areas that would not be accessible to traditional underwater vehicles.
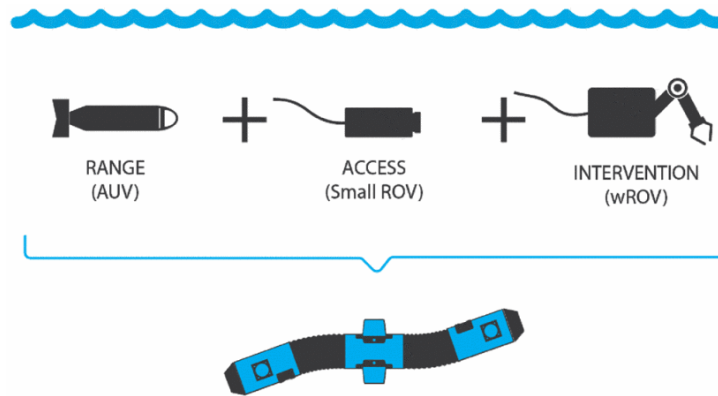
Figure 1.3: Eely Vehicle concept [7]

1.2 Research Question and Objectives

The main goal of this thesis is to investigate the high level of interdisciplinarity between control and risk assessment of autonomous underwater snake robots operating in confined environments by testing different mission/operation scenarios for Eely and validating whether or not Eely will be a suitable sensor-carrying platform for such missions in terms of adaptability and the risks associated with these missions. The main research questions of the thesis can be summarized as follows:

1. What are the advantages and disadvantages of using Eely in confined environments?

2. What are the risks associated with the operation of Eely in confined environments?

3. How to extend this BN to a DN to autonomously adapt Eely's behavior based on its belief about the current state of the risk?

4. How to robustly control the altitude of Eely?

5. In future work, how can the proposed methodology be extended to cover wider operational scenarios of Eely?

Figure 1.4 summarize the objectives and interdisciplinarity of fileds presented in the thesis.
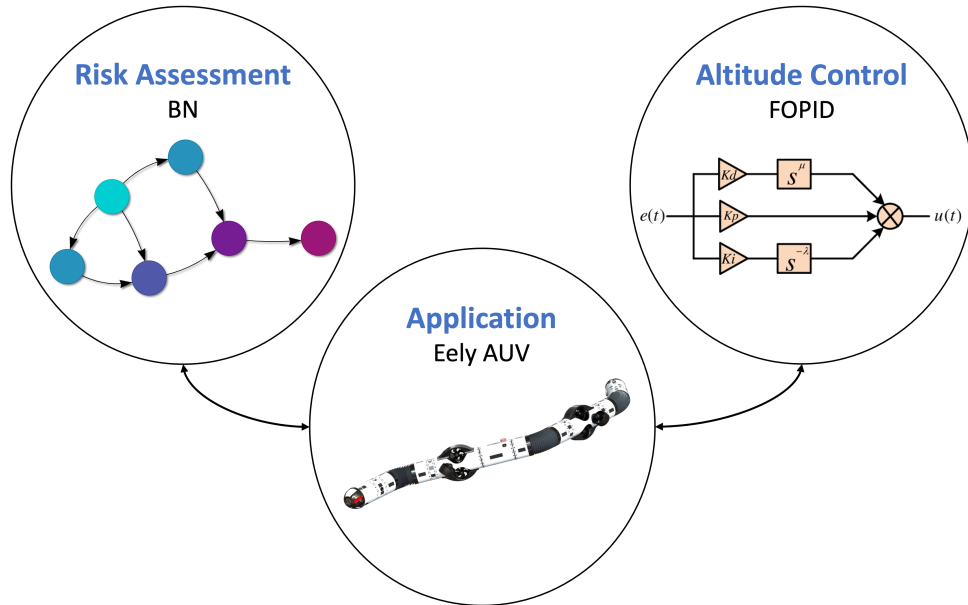
Figure 1.4: Thesis interdisciplinarity

1.3 Main Contributions

Main contributions are listed below:

- Development of a simulation model for Eely in Gazebo which allows for simulations in real time and visualization.

- An Altitude controller for Eely is proposed.

- Proposed a risk model that combines BBN with an altitude control model to assess the risk of losing Eely for three case/mission scenarios: seabed mapping, and confined environments operations.

The first two contributions, as well as the last, are mainly achieved in the papers. The individual contributions of the papers are included below for reference.

Paper 1: *The main scientific contribution [of this paper] is risk assessment of Eely in confined operations. This is important for improving Eely's performance and the likelihood of mission success. Relevant data are collected to perform a quantitative risk analysis to develop a Bayesian model that considers almost the entire system of Eely, thus avoiding potential risks. Although the model was developed specifically for Eely, it can be transferred to the operations of other autonomous underwater vehicles.*

Paper 2: *The primary scientific contribution [of this paper] is the development of an altitude controller model based on a nonlinear Fractional Order PID (FOPID) controller. The results of the study are promising for the Fractional Order PID (FOPID) controller in regulating the altitude of Eely Underwater Snake Robot. Unlike classical PID controllers, FOPID controllers have five parameters that can be adjusted to optimize their performance. This flexibility allows them to achieve better results, particularly for higher order systems where classical PID controllers may struggle.*

1.4 Thesis Outline

The thesis is divided into seven chapters describing each of the project's main aspects. The following chapters are included:

Chapter 2 - Mathematical Modeling and Sensors of Underwater Snake Robot: This chapter explains how an underwater snake robot can be modeled. In particular, the kinematics, hydrodynamics, and dynamics of an underwater snake robot. In addition to a brief overview about the main sensors used by Eely for mapping and monitoring.

Chapter 3 - Risk Assesment: This chapter proposes a risk model based on BN to assess the risk of losing Eely for two case/mission scenarios: Seabed mapping, and confined environments operations.

Chapter 4 - Altitude Control of Underwater Snake Robot: This chapter presents the altitude controller applied to Eely and the two Control methods applied to Eely, the nonlinear PID and the nonlinear FOPID.

Chapter 5 - Simulator Implementation: This chapter describes the implementation of Eely's model inside Plankton simulator and presents the simulation results.

Chapter 6 - Field Experiments: This chapter describes the field experiments with Eely in Trondheim Fjord and presents the results.

Chapter 7 - Conclusion and Further Work: This chapter covers the concluding remarks of the thesis, and presents the main challenges that is to be addressed in further work.

Mathematical Modeling and Sensors of Underwater Snake Robot

This chapter explains how an underwater snake robot can be modeled. In particular, the kinematics, hydrodynamics, and dynamics of an underwater snake robot. The last part of the chapter provides a brief overview about the main sensors used by Eely for mapping and monitoring, and their setup on the robot in the main scope of objectives.

2.1   Kinematics of Eely

The position and orientation of a marine craft moving in six Degrees of Freedom (DOF) can be described using several reference frames. The most common reference frames for underwater vehicles are:

- North-East-Down (NED) frame $\{n\} = (x_n, y_n, z_n)$

- Body-fixed (BODY) frame $\{b\} = (x_b, y_b, z_b)$

The NED frame is a flat tangential plane fixed at the Earth's surface used for local navigation, typically an area of 10×10 km, with the origin o_n. It is also assumed that the NED frame is an inertial frame. An inertial reference frame is a non-accelerating reference frame in which Newton's laws of motion apply. The NED frame rotates with the Earth and is technically not inertial, however this rotation is neglected for marine crafts moving at low speeds. The BODY frame is a moving coordinate frame that is fixed to the vehicle, and has the origin o_b. Usually, the position is expressed in the NED frame, and the velocities are expressed in the BODY frame. Each DOF can be expressed with the notation of [8], showed in Table 2.1.

Figure 2.1 illustrates the velocities in the BODY frame for Eely underwater vehicle. The generalized position and velocity coordinates are given by Equations 2.1 and 2.2 respectively:

$$\eta = [\eta_1^T \quad \eta_2^T]^T = [x \quad y \quad z \quad \phi \quad \theta \quad \psi]^T \tag{2.1}$$

Table 2.1: Degrees of freedom

		BODY		NED
DOF		Forces and moments	Linear and angular velocities	Positions and Euler angles
1	Motions in the x_b-direction (surge)	X	u	x
2	Motions in the y_b-direction (sway)	Y	v	y
3	Motions in the z_b-direction (heave)	Z	w	z
4	Rotation about the x_b-axis (roll)	K	p	ϕ
5	Rotation about the y_b-axis (pitch)	M	q	θ
6	Rotation about the z_b-axis (yaw)	N	r	ψ

$$\nu = [\nu_1^T \quad \nu_2^T]^T = [u \quad v \quad w \quad p \quad q \quad r]^T \tag{2.2}$$
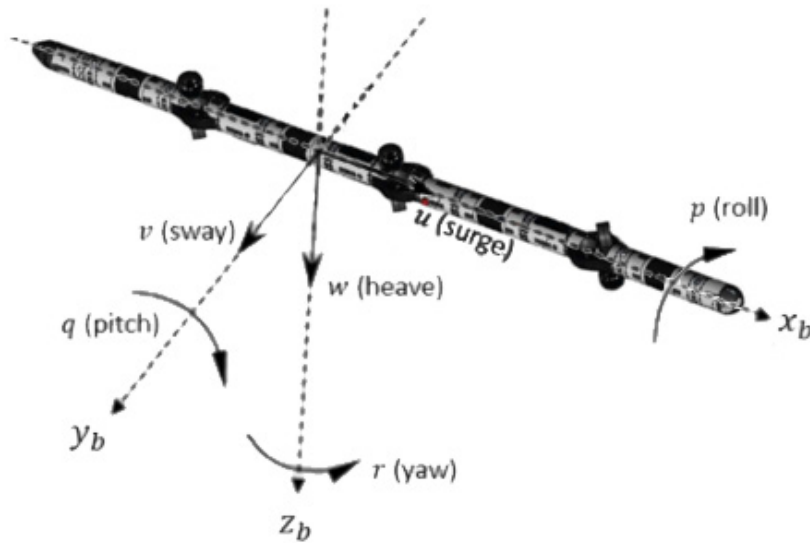
Figure 2.1: Degrees of freedom for Eely Underwater Vehicle

In order to transform between the BODY and NED frames, a rotation matrix is used. A rotation matrix $\boldsymbol{R}$ is an element in $SO(3)$, which is the special orthogonal group of order 3, shown in Equation 2.3:

$$SO(3) := \left\{ \boldsymbol{R} \mid \boldsymbol{R} \in \mathbb{R}^{3\times 3}, \ \boldsymbol{R}^{-1} = \boldsymbol{R}^\top, \det(\boldsymbol{R}) = 1 \right\} \tag{2.3}$$

The transformation between reference frames are based on the Euler angles of the vessel. These are roll (ϕ), pitch (θ) and yaw (ψ), they are defined as the orientation of the vehicle with respect to the NED frame. By using the Euler angles, it is possible to express the body fixed linear velocity vector, v_{nb}^b in the NED frame, according to the following Equation:

$$v_{nb}^n = R_b^n v_{nb}^b \tag{2.4}$$

where R_b^n is the rotation matrix from $\{b\}$ to $\{n\}$, $v_{nb}^n = \dot{p}_{nb}^n = [\dot{x}^n, \dot{y}^n, \dot{z}^n]^T$ is the velocity vector expressed in the NED-frame, and v_{nb}^n is the velocity vector expressed in the BODY-frame. R_b^n is calculated as:

$$\boldsymbol{R}_{x,\phi} = \begin{bmatrix} 1 & 0 & 0 \\ 0 & c\phi & -s\phi \\ 0 & s\phi & c\phi \end{bmatrix}, \boldsymbol{R}_{y,\theta} = \begin{bmatrix} c\theta & 0 & s\theta \\ 0 & 1 & 0 \\ -s\theta & 0 & c\theta \end{bmatrix}, \boldsymbol{R}_{z,\psi} = \begin{bmatrix} c\psi & -s\psi & 0 \\ s\psi & c\psi & 0 \\ 0 & 0 & 1 \end{bmatrix} \quad (2.5)$$

$$R_b^n = R(\Theta_{nb}) = R_{z,\psi}R_{y,\theta}R_{x,\phi} = \begin{bmatrix} c\psi c\theta & -s\psi c\phi + c\psi s\theta s\phi & s\psi s\phi + c\psi c\phi s\theta \\ s\psi c\theta & c\psi c\phi + s\phi s\theta s\psi & -c\psi s\phi + s\theta s\psi s\phi \\ -s\theta & c\theta s\phi & c\theta c\phi \end{bmatrix} \quad (2.6)$$

where Θ_{nb} is the vector containing the Euler angles.

Similarly, transformations can be carried out for the angular velocity. Let $w_{nb}^b = [p, q, r]^T$ be the BODY fixed angular velocities, and $T(\Theta_{nb})$ be the transformation matrix that relates BODY fixed angular velocities and Euler rates. The Euler rate vector $\dot{\Theta}_{nb}$ can be obtained as shown in Equation 2.7:

$$\dot{\Theta}_{nb} = T(\Theta_{nb})w_{nb}^b \quad (2.7)$$

where,

$$T(\Theta_{nb}) = \begin{bmatrix} 1 & s\phi t\theta & c\phi t\theta \\ 0 & c\phi & -s\phi \\ 0 & \frac{s\phi}{c\theta} & \frac{c\phi}{c\theta} \end{bmatrix} \quad (2.8)$$

In case of $\theta = 90°$, the robot would face a singularity. So, we avoid getting the joint angles to be exactly 90°. Another possible solution to this problem is to use quaternions.

So, the 6-DOF kinematic equations becomes:

$$\dot{\eta} = J_\Theta(\eta)\nu \quad (2.9)$$

The Jacobian matrix that relates the linear and angular velocities in the NED frame and the BODY frame $J_\Theta(\eta)$ can be written as:

$$J_\Theta(\eta) = \begin{bmatrix} \dot{p}_{nb}^n \\ \dot{\Theta}_{nb} \end{bmatrix} = \begin{bmatrix} R(\Theta_{nb}) & 0_{3\times3} \\ 0_{3\times3} & T(\Theta_{nb}) \end{bmatrix} \begin{bmatrix} \nu_{nb}^n \\ w_{nb}^b \end{bmatrix} \quad (2.10)$$

where $\eta \in \mathbb{R}^6$ is the position and orientation in the NED frame, $J_\Theta(\eta) \in \mathbb{R}^{6\times6}$ is the Jacobian matrix that relates the linear and angular velocities in the NED frame and the BODY frame, and $\nu \in \mathbb{R}^6$ is the velocity in the BODY frame.

Skew-symmetric matrices and quaternions are other useful tools for describing the system's kinematics. Skew-symmetric matrices provides a way for calculating the cross-product of two vectors without using the cross-product-operator. Let $\lambda = [\lambda_1, \lambda_2, \lambda_3]^T$, the the skew-symmetric matrix $\mathbf{S}$ is defined as:

$$S(\lambda) = -S^T(\lambda) = \begin{bmatrix} - & -\lambda_3 & \lambda_2 \\ \lambda_3 & 0 & -\lambda_1 \\ -\lambda_2 & \lambda_1 & 0 \end{bmatrix} \tag{2.11}$$

So, the cross product for two vectors can be calculated as:

$$\lambda \times a = S(\lambda)a \tag{2.12}$$

where a is a vector having the same dimensions of λ, i.e $a = [a1, a2, a3]^T$.

Quaternions allow the kinematic equations to be represented without using Euler angles. The drawback of using quaternions is that the transformation matrix T is not defined when the pitch angle $\theta = \pm 90°$. So, quaternions are introduced to improve the robustness. A quaternion **q** is a complex number that consists of one real part η, and three imaginary parts $\varepsilon = [\varepsilon_1, \varepsilon_2, \varepsilon_3]^T$. A set of a unit quaternions Q can be defined as:

$$Q := \left\{ \boldsymbol{q} \mid \boldsymbol{q}^T \boldsymbol{q} = 1, \ \boldsymbol{q} = [\eta, \varepsilon^T]^T, \eta \in \mathbb{R}, \varepsilon \in \mathbb{R}^3 \right\} \tag{2.13}$$

For our application case, an underwater snake robot consisting of multiple articulated rigid bodies with separate coordinate frames attached to each body, there is a high probability of having a shape configuration with at least one of the coordinate frames oriented with a 90° pitch angle. So, using quaternions representation for each body can limit the cases where transformations are not defined. Euler angles, on the other hand are easier for a person to understand when defining orientation. So, being able to represent the relation between Euler angles and unit quaternions is useful. Equation 2.14 shows how to transform from quaternions to Euler angles:

$$\Theta_{nb} = \begin{bmatrix} atan2(2(\varepsilon_2\varepsilon_3 + \varepsilon_1\eta), \ 1 - 2(\varepsilon_1^2 + \varepsilon_2^2)) \\ -asin(2(\varepsilon_1\varepsilon_3 - \varepsilon_2\eta)) \\ atan2(2(\varepsilon_1\varepsilon_2 + \varepsilon_3\eta), \ 1 - 2(\varepsilon_2^2 + \varepsilon_3^2)) \end{bmatrix} \tag{2.14}$$

In the same way, Equation 2.15 shows how to transform from Euler angles to quaternions:

$$\boldsymbol{q} = \begin{bmatrix} c\left(\frac{1}{2}\psi\right) c\left(\frac{1}{2}\theta\right) c\left(\frac{1}{2}\phi\right) + s\left(\frac{1}{2}\psi\right) s\left(\frac{1}{2}\theta\right) s\left(\frac{1}{2}\phi\right) \\ c\left(\frac{1}{2}\psi\right) c\left(\frac{1}{2}\theta\right) s\left(\frac{1}{2}\phi\right) - s\left(\frac{1}{2}\psi\right) s\left(\frac{1}{2}\theta\right) c\left(\frac{1}{2}\phi\right) \\ s\left(\frac{1}{2}\psi\right) c\left(\frac{1}{2}\theta\right) s\left(\frac{1}{2}\phi\right) + c\left(\frac{1}{2}\psi\right) s\left(\frac{1}{2}\theta\right) c\left(\frac{1}{2}\phi\right) \\ s\left(\frac{1}{2}\psi\right) c\left(\frac{1}{2}\theta\right) c\left(\frac{1}{2}\phi\right) - c\left(\frac{1}{2}\psi\right) s\left(\frac{1}{2}\theta\right) s\left(\frac{1}{2}\phi\right) \end{bmatrix} \tag{2.15}$$

On using quaternions, the rotation matrix **R**, and the transformation matrix **T** can be expressed as:

$$R(q_b^n) = I_3 + 2\eta S(\varepsilon) + 2S^2(\varepsilon) \tag{2.16}$$

$$T(q_b^n) = \frac{1}{2} \begin{bmatrix} -\varepsilon^T \\ \eta I_3 + S(\varepsilon) \end{bmatrix} \tag{2.17}$$

where $S(\varepsilon)$ is skew-symmetric matrix presented in Equation 2.11, and I_3 is the identity matrix.

So, the 6-DOF kinematic equations in terms of quaternions becomes:

$$\dot{\eta} = J_q(\eta)\nu \tag{2.18}$$

The Jacobian matrix that relates the linear and angular velocities in the NED frame and the BODY frame $J_\Theta(\eta)$ can be written as:

$$J_q(\eta) = \begin{bmatrix} \dot{p}^n_{nb} \\ \dot{q}_{nb} \end{bmatrix} = \begin{bmatrix} R(q^n_b) & 0_{3\times3} \\ 0_{4\times3} & T(q^b_n) \end{bmatrix} \begin{bmatrix} \nu^n_{nb} \\ w^b_{nb} \end{bmatrix} \tag{2.19}$$

where $\eta \in \mathbb{R}^7$ is the position and orientation in the NED frame, $J_q(\eta) \in \mathbb{R}^{7\times6}$ is the Jacobian matrix that relates the linear and angular velocities in the NED frame and the BODY frame, and $\nu \in \mathbb{R}^6$ is the velocity in the BODY frame.

2.2 Hydrodynamics of Eely

Hydrodynamic model of Eely combines linear and non-linear drag forces, added mass effect, fluid moments and current effect. The hydrodynamic model in Equation 2.20 is in closed-form to avoid numerical evaluations with drag forces [9] [10].

$$f = \begin{bmatrix} f_x \\ f_y \end{bmatrix} = \begin{bmatrix} f_{A_x} \\ f_{A_y} \end{bmatrix} + \begin{bmatrix} f^I_{D_x} \\ f^I_{D_y} \end{bmatrix} + \begin{bmatrix} f^{II}_{D_y} \\ f^{II}_{D_y} \end{bmatrix} \tag{2.20}$$

where f_{A_x} and f_{A_y} are the effects due to the added mass forces and are expressed as:

$$\begin{bmatrix} f_{A_x} \\ f_{A_y} \end{bmatrix} = -\begin{bmatrix} \mu\left(\boldsymbol{S_\theta}\right)^2 & -\mu\boldsymbol{S_\theta C_\theta} \\ -\mu\boldsymbol{S_\theta C_\theta} & \mu\left(\boldsymbol{C_\theta}\right)^2 \end{bmatrix} \begin{bmatrix} \ddot{\boldsymbol{X}} \\ \ddot{\boldsymbol{Y}} \end{bmatrix} - \begin{bmatrix} -\mu\boldsymbol{S_\theta C_\theta} & -\mu\left(\boldsymbol{S_\theta}\right)^2 \\ \mu\left(\boldsymbol{C_\theta}\right)^2 & \mu\boldsymbol{S_\theta C_\theta} \end{bmatrix} \begin{bmatrix} \boldsymbol{V}^a_x \\ \boldsymbol{V}^a_y \end{bmatrix} \dot{\boldsymbol{\theta}} \tag{2.21}$$

where $\mu = \text{diag}(\mu_1, \ldots, \mu_n) \in \mathbb{R}^{n\times n}$, $V^a_x = \text{diag}(V_{x,1}, \ldots, V_{x,n}) \in \mathbb{R}^{n\times n}$, $V^a_y = \text{diag}(V_{y,1}, \ldots, V_{y,n}) \in \mathbb{R}^{n\times n}$ and $[V_{x,i}, V_{y,i}]^T$ are the ocean current velocity expressed in the inertial frame, $S_\theta = \text{diag}(\sin\theta)^T \in \mathbb{R}^{n\times n}$ and $C_\theta = \text{diag}(\cos\theta)^T \in \mathbb{R}^{n\times n}$.

$f^I_{D_x}$ and $f^I_{D_y}$ are the linear drag effects, while $f^{II}_{D_x}$ and $f^{II}_{D_y}$ are the non-linear drag effects expressed in Equations 2.22 and 2.23:

$$\begin{bmatrix} f^I_{D_x} \\ f^I_{D_y} \end{bmatrix} = -\begin{bmatrix} c_t C_\theta & -c_n S_\theta \\ c_t S_\theta & c_n C_\theta \end{bmatrix} \begin{bmatrix} V^{link}_{r_k} \\ V^{lin}_{r_y k} \end{bmatrix} \tag{2.22}$$

$$\begin{bmatrix} f^{II}_{D_I} \\ f^{II}_{D_y} \end{bmatrix} = -\begin{bmatrix} c_t C_\theta & -c_n S_\theta \\ c_t S_\theta & c_n C_\theta \end{bmatrix} \text{sgn}\left(\begin{bmatrix} V^{link}_{r_x} \\ V^{link}_{r_y} \end{bmatrix}\right) \begin{bmatrix} \left(V^{link}_{r_x}\right)^2 \\ \left(V^{link}_{r_y}\right)^2 \end{bmatrix} \tag{2.23}$$

11

where $c_t = diag(c_{t,1}, ..., c_{t,n})$, $c_n = diag(c_{n,1}, ..., c_{n,n})$, while $V_{r_x}^{link}$ and $V_{r_y}^{link}$ are expressed as:

$$\begin{bmatrix} V_{r_x}^{\text{link}} \\ V_{r_y}^{\text{link}} \end{bmatrix} = \begin{bmatrix} C_\theta & S_\theta \\ -S_\theta & C_\theta \end{bmatrix} \begin{bmatrix} \dot{X} - V_x \\ \dot{Y} - V_y \end{bmatrix} \tag{2.24}$$

where $V_x = \text{diag}(V_{x,1}, \dots, V_{x,n}) \in \mathbb{R}^{n \times n}$ and $V_y = \text{diag}(V_{y,1}, \dots, V_{y,n}) \in \mathbb{R}^{n \times n}$ are the current velocities.

2.3 Dynamics of Eely

An efficient algorithm for the forward dynamics of Eely was proposed in [11]. The equation of motion for Eely after eliminating the constraint forces is expressed as:

$$H(\vartheta)\dot{\zeta} + C(\vartheta, \zeta)\zeta + F(\vartheta, \zeta)\zeta + g(\vartheta) = \eta \tag{2.25}$$

where $H(\vartheta)$ is the system inertia matrix, $C(\vartheta, \zeta)$ the hydrodynamical drag matrix, $g(\vartheta)$ contains forces due to weight and buoyancy, and $\eta = [\eta_1^T \dots \eta_n^T] \in \mathbb{R}^a$ is a vector of external forces with $\eta_i \in \mathbb{R}^{a_i}$.

The forward dynamics algorithm for the hydrodynamically decoupled form of Equation 2.25 including the effect of steady and uniform ocean current and motor and thruster forces, is presented in Algorithm 1

This algorithm is based on the composite rigid body algorithm presented in [12]. Note that the terms $H_{i,j} \in \mathbb{R}^{a_i \times a_j}$ are sub-matrices of the system inertia matrix $H(\vartheta)$ which give the inertial coupling between joint i and joint j.

Algorithm 1 Forward Dynamics

$\acute{\xi}^0_{0,0'} \leftarrow 0$
for $i \leftarrow 1$ to n **do**
    $A_i^{\lambda(i)} \leftarrow \Lambda_i\left(\vartheta_i\right)$
    $\xi^i_{i,\lambda(i)} \leftarrow \Phi_i\left(\vartheta_i\right)\zeta_i$
    $\acute{\xi}^i_{i,\lambda(i)} \leftarrow \Theta_i\left(\vartheta_i, \zeta_i\right)\zeta_i$
    $\xi^i_{i,0'} \leftarrow A^i_{\lambda(i)}\xi^{\lambda(i)}_{\lambda(i),0'} + \xi^i_{i,\lambda(i)}$
    $\acute{\xi}^i_{i,0'} \leftarrow A^i_{\lambda(i)}\acute{\xi}^{\lambda(i)}_{\lambda(i),0'} + \acute{\xi}^i_{i,\lambda(i)} + \left[\xi^i_{i,0'}\right]_\wedge \xi^i_{i,\lambda(i)}$
    $\gamma^i \leftarrow R^i_{\lambda(i)}\gamma^{\lambda(i)}$
    $\acute{\tau}_i \leftarrow -M_i\acute{\xi}^i_{i,0'} - \Omega_i\left(\xi^i_{i,0'}\right)\xi^i_{i,0'} - D_i\left(\xi^i_{i,0'}\right)\xi^i_{i,0'} - G_i\gamma^i$
end for
for $i \leftarrow 1$ to $n_\star$ **do**
    $\acute{\tau}_{\lambda(i\star)} \leftarrow \acute{\tau}_{\lambda(i\star)} + \psi_{i\star}\nu_{i\star}$
end for
for $i \leftarrow n$ to 1 **do**
    $\acute{\eta}_i \leftarrow \Phi_i^{\mathrm{T}}\acute{\tau}_i + \psi_{i\star}\nu_{i\star}$
    if $\lambda(i) \neq 0$ **then**
        $\acute{\tau}_{\lambda(i\star)} \leftarrow \acute{\tau}_{\lambda(i\star)} + A^{i\ \mathrm{T}}_{\lambda(i)}\acute{\tau}_i$
    end if
end for
$H \leftarrow O_a$
for $i \leftarrow n$ to 1 **do**
    $\acute{M}_i \leftarrow M_i$
end for
for $i \leftarrow n$ to 1 **do**
    if $\lambda(i) \neq 0$ **then**
        $\acute{M}_{\lambda(i)} \leftarrow \acute{M}_{\lambda(i)} + A^{i\ \mathrm{T}}_{\lambda(i)}\acute{M}_i A^i_{\lambda(i)}$
    end if
    $X \leftarrow \acute{M}_i\Phi_i$
    $H_{i,i} \leftarrow \Phi_i^{\mathrm{T}}X$
    $j \leftarrow i$
    while $\lambda(j) \neq 0$ **do**
        $X \leftarrow A^{j\ \mathrm{T}}_{\lambda(j)}X$
        $j \leftarrow \lambda(j)$
        $H_{i,j} \leftarrow X^{\mathrm{T}}\Phi_j$
        $H_{j,i} \leftarrow H_{i,j}^{\mathrm{T}}$
    end while
end for
$\dot{\vartheta} \leftarrow T(\vartheta)\zeta$
$\dot{\zeta} \leftarrow H^{-1}\acute{\eta}$

2.4 Sensors

Eely uses an advanced sensor suite to help navigate. Some of these sensors are described in the following subsections below. A full sensor suite can be seen in table 2.2.

Table 2.2: Full sensor suite for Eely

Device	Quantity
DVL	1
HD Camera	1
IMU	1
Leakeage sensor	3
Multibeam echosounder	1
Ping Sonar Altimeter and Echosounder	1
Pressure sensor	1
UHI	1

2.4.1 DVL

The Doppler Velocity Log (DVL) is an acoustic sensor device utilized for measuring velocities based on the Doppler shift in frequency. When an object is moving towards or away from the DVL, the sensor measures the change in frequency of the acoustic signal reflected from the object. This allows the DVL to accurately determine velocities and estimate the distance traveled.

Typically, a DVL consists of four transducer heads, each emitting a beam of sonic pulses. By analyzing the echoes received from these pulses, the DVL can calculate the velocity vector of the vehicle relative to either the seafloor or the water column. The output of the DVL includes three-dimensional velocity measurements: u, v, and w components. The coverage of each beam is determined by the angle at which each transducer head is positioned [13].

2.4.2 UHI

In recent years, the demand for hyperspectral imaging for environmental mapping and monitoring has steadily increased. This includes sensor deployment on aerial, satellites, and most recently, underwater platforms [14]. The underwater hyperspectral imager (UHI) in Figure 2.2 combines a push-broom hyperspectral imager with an external light source [15]. For the external light source, Halogen and LED lights are usually used. Halogen lights are mostly used as they have close to a uni-formally distributed energy spectrum across the frequencies of visible light, while LED lights have the capability to boost the spectrum as required within the range of interest which is beneficial for applications where illumination is needed to make up for any deficiencies caused by a camera's response sensitivity or when matching a specific spectral profile is a requirement for the light source [16]. The imaging sensor is capable of measuring reflected light from

380 to 800 nm in contrary to normal RGB cameras which are only using 3 colour, and thus creating an energy spectrum of the environment. This in turn might be used to create an unique spectrum for specific OOIs [17].

Recently, Ecotone a Spin-off company from NTNU [18] has developed the first complete UHI system on the market. An illustration of their product mounted on Eely snakerobot is shown in Figure 2.2.
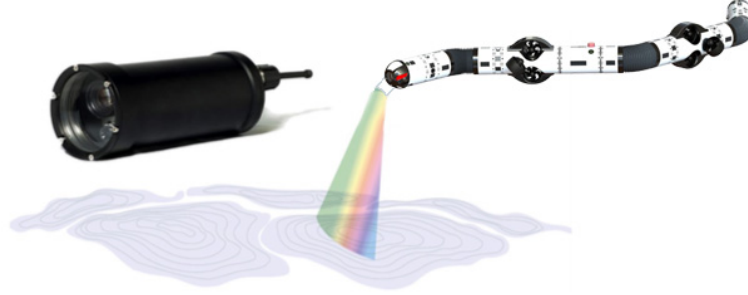
Figure 2.2: Underwater Hyperspectral Imager mounted on Eely

2.4.2.1 Hyperspectral Imaging Principles

A UHI sensor weighs about 5 kg and is able to dive to depths of up to 6000 meters, thanks to its titanium housing. It consists of both a regular RGB camera and a hyper-spectral imager. Many UHI sensors also have an altimeter to calculate the distance from the object being measured.

The hyperspectral imager measures light across a range of frequencies, including those outside the range of visible light to humans. The amount of light received by the UHI is measured in radiance, which is a unit of measurement for electromagnetic energy denoted $L\,[Wm^{-2}sr^{-1}nm^{-1}]$. Radiance is the most important parameter in evaluating the usefulness of the data, as it is affected by factors such as water visibility, the intensity of sunlight and other external light sources, and the distance and material of the object of interest (OOI).

Two principles affect the radiance when light is emitted from an external light source: attenuation and backscattering. Attenuation is the principle that the intensity of the light decreases as the distance from the light source increases. This relationship is exponential, and assuming only one external light source is present, it can be represented by the function:

$$L(z, \hat{\xi}) = L(0; \hat{\xi})e^{-c(\lambda)z} \tag{2.26}$$

where z and $\hat{\xi}$ represent the distance and direction from the light source, respectively, and $c(\lambda)$ is an attenuation coefficient that depends on the wavelength of the emitted signal.

Backscattering is an additive effect, meaning that it adds unwanted radiance as the emitted light reflects off particles in the water and surrounding environment. This effect causes the quality of measurements to decrease with distance and the presence of particles in the water [19]. Filtering this radiance out of the measured signal is not straightforward,

15

but in clear water and at moderate distances, high-quality results can still be obtained
despite the presence of backscattering.

The main principle behind the UHI sensor is that it sends out light in a push-broom, or
fan-like pattern, and measures the spectrum of light received from the environment. A
simplified model often assumes a flat surface, such as the sea bed or ice. This means that
the spatial range of the sensor is proportional to its altitude, allowing it to map a larger
area by increasing its altitude. However, this also reduces the usefulness of the data,
which can be assumed to be proportional to the radiance. A sketch of the simplified UHI
model is shown in Figure 2.3.
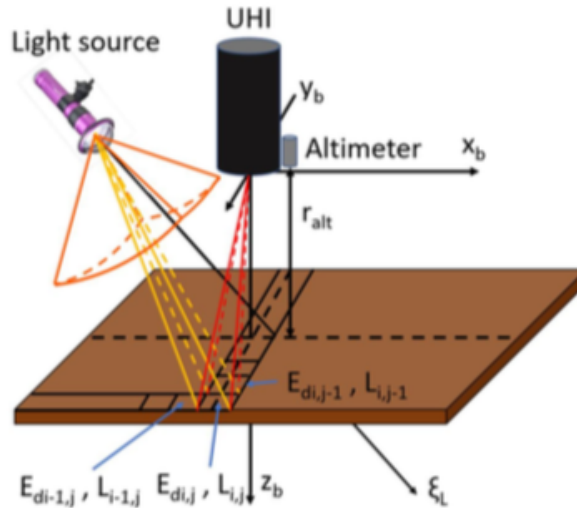
Figure 2.3: Simplified UHI model assuming a flat surface [20]

2.4.2.2 Applications in the Underwater Domain

The main challenge in seabed mapping and exploration is the complex and dynamic
behaviour of the seabed, as it is exhibiting large variation of biogeochemical composition
over time and space [17]. The traditional mapping methods often have spatial limitations
and are qualitative on a high level of human interpretation to obtain results. These
methods include in situ diver surveys, ship-based acoustics (echosounders), benthic box
core, epibenthic sledge and beam trawl samples, underwater photography, and video
towed from boat as some examples. Most of these methods depend on the luminosity
from sunlight and how far can it penetrate the water layers which does not help in seabed
mapping as the seafloor is usually optically deep and a very small portion of sunlight
reaches it depending on the OOI location as well [20].

The main strength point of UHI is the use of an external light source to provide the
required luminosity to rely on the spectral signature of the unique features of the benthos.
Thus, different OOIs absorb and reflect different intensities for different frequencies in the
visible spectrum giving them a unique optical fingerprint. So, mounting the UHI sensor
on a underwater platform like Eely will make use of these fingerprints to qualitatively
and quantitatively develop maps of minerals, benthic habitats, substrates, and organisms
living on the seabed [21].

The dominating factor limiting the use of UHI sensor is the water visibility, as it varies

a lot from a place to another and from a season to another especially in confined environments which are our regions of interest. Plankton drifting in the water can to a large extend limit the use if UHI sensor [22].

2.4.3 Setup of Sensors on Eely

Figure 2.4 shows the DVL and UHI sensors that were incorporated into the simulation model of Eely. The UHI sensor is positioned at the head of Eely, while the DVL sensor is situated in the middle of Eely's sensor module.
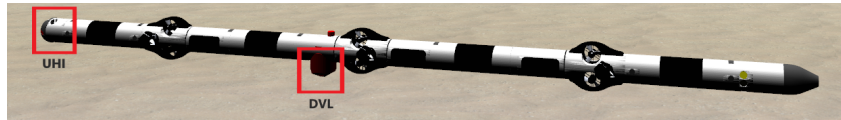
Figure 2.4: Sensor placements onboard Eely

Chapter 3

Risk Assessment

This chapter contains two parts. Firstly the most important terms that will reoccur throughout the chapter will be presented. In the second part, a Bayesian approach to asses the risks of losing Eely during two mission scenarios will be presented. The goal of this chapter is to improve Eely's performance and the likelihood of mission success. Sensitivity analysis results are presented in order to demonstrate the causes having the highest impact on losing Eely.

3.1 Definitions

3.1.1 Risk

Risk can be defined in various ways. According to ISO 31000 [23], risk refers to the potential impact of uncertainty on objectives, where the impact is a deviation from expected outcomes. Another definition, provided in NORSOK Z-013 [24], states that risk is a combination of the probability of occurrence of harm and the severity of that harm. However, for the purpose of this thesis, Rausand's [25] definition of risk is considered more appropriate and easier to understand. Rausand defines risk as the answer to three critical questions:

1. What can go wrong?

2. What is the likelihood of it happening?

3. What are the potential consequences?

The combination of these responses creates a comprehensive picture of the hazards, the associated consequences, and the likelihoods of their occurrence. These factors together make up the qualitative dimensions and components of risk.

The definition of risk related to a hazardous event e_i [26] can be represented by the following relation:

$$r = \{e_i, c_i, q\}|k \tag{3.1}$$

where c_i is the consequence of e_i, q is the measure of involved uncertainty, and k is the background knowledge for determining e_i, c_i and q. This is the most commonly used definition for Bayesian risk modeling. By accounting for previous knowledge about the operational conditions and mission scenarios, events with low background knowledge would not have a strong effect when making a decision in contrast to events with high background knowledge.

3.1.2 Hazard

A hazard according to NORSOK Z-013 [24] is defined as a potential source of harm that can result in loss of life, damage to health, environment, assets, or a combination of these. A hazardous event refers to the occurrence when a hazard is released.

3.1.3 Risk Management

Risk management is the process of designing and implementing a framework, procedures and processes to manage risk [23]. The risk management process according to ISO 31000 consists of five interrelated steps: establishing context, risk assessment, risk treatment, communication and consultation, and monitoring and review, thus ensuring continuous improvement of risk management. Figure 3.1 depicts the process outlined in ISO 31000. Communication and consultation play a critical role in identifying all risks and hazards by involving experts from different fields.
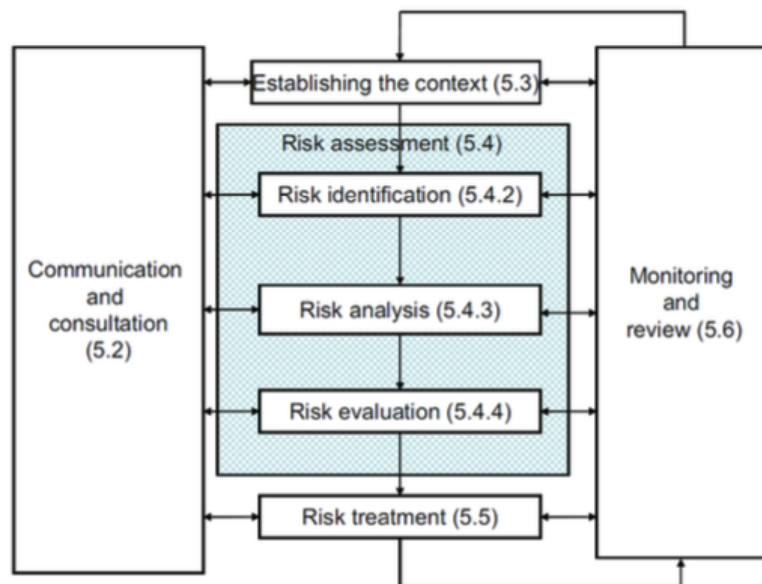
Figure 3.1: ISO 31000 Risk Management Process [23]

Establishing the context involves defining the scope, purpose, and goals of the risk management process. The risk assessment process includes three steps: risk identification, risk analysis, and risk evaluation. During risk identification, hazards are reviewed and the possible harm is identified. Risk analysis examines how the hazards might manifest

and assesses their relevance in the established context. Risk evaluation determines the level of risk and provides input for decision-making and risk treatment

Risk treatment involves identifying measures to reduce the risk induced by relevant risk contributors. The principle that risk should be reduced as long as the associated effort is not disproportional should always be applied [27]. The process of monitoring and review continually reduces the level of risk. Reassessing risk with the knowledge and experience gained during the process allows for the discovery of better and new ways of risk mitigation.

3.2 Risk Modeling using BNs

3.2.1 Bayesian Networks

A Bayesian network is a graphical model used to address problems involving uncertainty [28, 29]. It describes the dependencies between random variables in a directed acyclic graph, where nodes stand for random variables and directed arcs between nodes signify conditional dependencies between them. The Bayesian network, which is based on probability theory [30], allows for two-way reasoning by handling both causal reasoning, which derives posterior probabilities from prior probabilities, and diagnostic reasoning, which uses a formula to derive prior probabilities from posterior probabilities. The traditional static Bayesian network (SBN) has limitations when it comes to evaluating variables that change over time, but it is useful for analyzing and forecasting data at a specific time. The dynamic Bayesian network was created to overcome this drawback. The dynamic Bayesian network (DBN) incorporates methods that take into account the relationship between moments in time, known as the state transition probability, in contrast to SBN [31]. By considering this relationship, the network can learn to effectively use changes in values over time, producing better results.

DBNs rely on the Bayesian formula and the independence hypothesis as the foundation for their reasoning, which is based on probabilistic calculations based on an existing model. The calculation uses the joint distribution of all nodes in the evaluation model, denoted as $P(X_1, X_2, ..., X_n)$, and the set of parent nodes for X_i denoted as $P_a(X_i)$, as follows:

$$P(x \mid y) = \frac{P(xy)}{P(y)} = \frac{P(xy)}{\sum_x P(xy)} \tag{3.2}$$

$$P(X_1, X_2, \ldots, X_n) = \prod_{i=1}^{n} P(X_i \mid P_a(X_i)) \tag{3.3}$$

Combining the formulas and presumptions mentioned above, the following inference mechanism can be derived for the SBN model, which typically has n hidden nodes and m observation nodes:

$$P\left(x_1, x_2, \ldots, x_n \mid y_1, y_2, \ldots, y_m\right)$$
$$= \frac{\prod_j P\left(y_j \mid P_a\left(y_j\right)\right) \prod_i P\left(x_i \mid P_a\left(x_i\right)\right)}{\sum_{x_1, x_2, \ldots, x_n} \prod_j P\left(y_j \mid P_a\left(y_j\right)\right) \prod_i P\left(x_i \mid P_a\left(x_i\right)\right)} \tag{3.4}$$

The value of i in the formula ranges from 1 to n, and the value of j from 1 to m. x_i denotes the value of the random variable X_i, y_j denotes the value of the observation variable Y_j. In particular, $P_a(x_i)$ and $P_a(y_j)$ represent the set of parent nodes for x_i and y_j, respectively. The reasoning process for the DBN can be derived from Equation 3.4 by extending it along the timeline to create a dynamic network with T time points. In Equation 3.5, where i ranges from 1 to T, j ranges from 1 to m, and k ranges from 1 to n, the distribution of hidden variables can be described when the observation values are in a single composite state. In this equation, the hidden node X_{ij} value state is denoted by x_{ij}, where i and j are the hidden node current time point and the hidden node within this time point, respectively. The observation variable Y_{ij} value is denoted by y_{ij}, and the set of parent nodes for y_{ij} are denoted by $P_a(y_{ij})$.

$$P\left(x_{1n}, \ldots, x_{Tn} \mid y_{1n}, \ldots, y_{Tn}\right) = \frac{\prod_{ij} P\left(y_{ij} \mid P_a\left(y_{ij}\right)\right) \prod_{ik} P\left(x_{ik} \mid P_a\left(x_{ik}\right)\right)}{\sum_{x_{1n}, \ldots, x_{Tn}} \prod_{ij} P\left(y_{ij} \mid P_a\left(y_{ij}\right)\right) \prod_{ik} P\left(x_{ik} \mid P_a\left(x_{ik}\right)\right)} \tag{3.5}$$

Equation 3.6 can be applied if the observation variable has multiple states. y_{ijs} denotes the state of the j observation node x_{ij}, during the i time slice. The likelihood that y_{ij} is present in the appropriate state is $P(y_{ij} = y_{ijs})$. With this, the inference process for the DBN is completely described.

$$P\left(x_{1n}, \ldots, x_{Tn} \mid y_{1ns}, \ldots, y_{Tns}\right) = \sum_{y_{1n}, \ldots, y_{Tn}} \times \frac{\prod_{ij} P\left(y_{ij} = y_{ijs} \mid P_a\left(y_{ij}\right)\right) \prod_{ik} P\left(x_{ik} \mid P_a\left(x_{ik}\right)\right)}{\sum_{x_{1n}, \ldots, x_{Tn}} \left[\prod_{ij} P\left(y_{ij} \mid P_a\left(y_{ij}\right)\right) \prod_{ik} P\left(x_{ik} \mid P_a\left(x_{ik}\right)\right)\right]}$$
$$\times \prod_{ij} P\left(y_{ij} = y_{ijs}\right) \tag{3.6}$$

3.2.2 Risk Assessment

Risk in the context of operating Eely is associated with several potential hazards. These hazards encompass risks to the operators' life and health, as well as the potential loss or damage to Eely and other AUVs when deployed as part of an underwater monitoring fleet. Additionally, an important consideration is the potential environmental damage that may occur due to contact between Eely and subsea infrastructure or the seabed. To focus the assessment, specific areas of risk will be considered, namely the loss of the vehicle, and damage to the vehicle. In terms of environmental impact, the risk arising from the loss of the vehicle is considered to be negligible, given the vehicle's low environmental impact. Additionally, it should be noted that Eely will not be operated in close proximity to offshore or subsea facilities, reducing the risk of incidents in those areas.

Although the risk of loss of life and health related issues is assumed to be under control,

it is important to acknowledge that these aspects should be evaluated in a separate risk assessment to ensure that comprehensive safety measures are in place.

The analysis is limited to a functional assessment of the major components. Figure 3.2 provides a summary of the subsystems of interest and the considered influences. Furthermore, it is assumed that personnel are well trained on the operation of Eely and follow the procedures outlined in the Eely user manual. However, it is important to account for the possibility of errors or incidents during operation, as no system is entirely exempted from them.
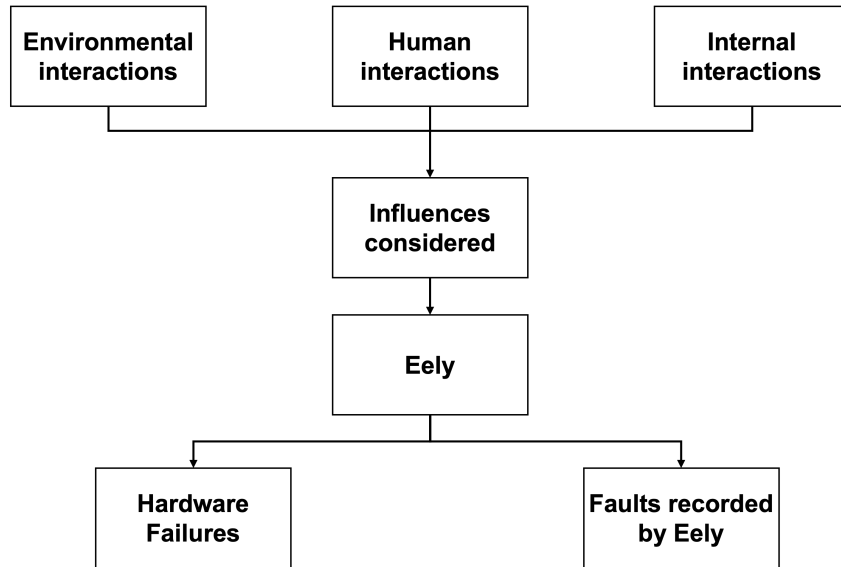
Figure 3.2: Subsystems and interactions taken into account for the risk assessment. Adopted from [27]

Another important point to note is that, up until now, Eely has not been lost, and no critical incidents have occurred at NTNU. Therefore, it is crucial to have a balance and avoid too conservative estimations that may hinder progress or efficiency for developing Eely.

3.2.3   HAZID

In context of risk assessment, Definition 3.1 may imply a Bayesian approach to probabilities, and hence the use of BN is a suitable approach to estimate the probability of losing Eely during different operational scenarios. HAZID was performed for the two case scenarios: i. Seabed mapping and ii. Confined environments operations in the form of a preliminary hazard analysis (PHA) prior to the development of the Bayesian risk model. Using the five-step method described in [32], the Bayesian risk model is developed.

HAZID aims to identify the hazards related to the operation of Eely for the two proposed case scenarios. Detectability is defined as Eely's ability to detect and monitor a specific hazard during its operation, where a high degree of detectability suggests a strong background knowledge, while a low degree of detectability suggests a weak background knowledge. The collection of hazards was mainly based on [33] as it offered a comprehensive compilation of potential risks and served as the foundation for the identification

procedure, along with our own judgment and similar systems [32]. In addition to, previous field trials with Eely in Trondheim Fjord [34] and previous experiments in karstic exploration [6, 35, 36] were also taken into account.

Table 3.1, adopted from [32] which was used for hazards in the context of AUV operation under ice, the same criteria was selected and modified based on hazards related to Eely's operation. Then, these hazards were assigned possible consequences depending on each case scenario, and the most noticeable hazards were identified. The risk priority number (rpn) for each hazard is obtained from the categories shown in Table 3.1. The rpn is the product of the frequency rating, the consequence rating, and the detectability rating. To assess the risk, the worst-case scenario is assumed which is losing Eely. Note that this loss may be temporary, as in the case of seabed mapping and deploying a vessel may recover Eely [37], or it can be a permanent loss as in the case of underwater caves. Tables VII-VIII in the Appendix of Paper 1 lists the hazards identified for the two case scenarios presented in the study. The assessment sheets design in the tables is based on the PHA sheet from [38].

Table 3.1: Criteria used to rate Frequency, Consequences and Detectability of events

Rating	Score	Description
Frequency		
Low	1	The event may occur less than once per mission
Medium	2	The event will be encountered, on average, once per mission
High	3	The event will be encountered several times per mission
Consequences		
Low/None	1	The event will have no negligible influence on the mission with respect to damage to Eely or loss of mission data
Medium	2	The event may lead to damages or delays that will minorly reduce the time available for the mission or affect the data collection
High	3	The event may lead to loss of Eely, early abortion of the mission, or significant loss of scientific data
Detectability		
Low/None	3	Eely is not able to detect or assess the hazardous event during the operation
Medium	2	Eely may infer information about the hazardous event. However, the inference will be associated with high uncertainty
High	1	Eely may collect and infer information about the hazardous event with high certainty

3.2.4 Failure Probabilities

The failure probabilities per year are given in Table 3.2, which are used in the BN nodes. However, it should be noted that failure probabilities for some parts of the robot's sensors were taken as for the general parts and not for a product of a specific brand from a specific

company. For example, the failure probability for the Underwater hyperspectral imager (UHI) sensor was taken as the same value for the general camera as the UHI is simply a more advanced camera as it combines a push-broom hyperspectral imager with an external light source [39]. The obtained data which is available is used as an initial attempt for quantitative risk assessment, but more proper assumptions and precise data could be extracted in future trials and for system suppress analysing own design.

Table 3.2: Failure Probabilities

Sensor/Item	Failure Probability
Joint module actuators	0.125
Thruster module actuators	0.1
DVL sensor	0.1
IMU sensor	0.01
UHI sensor	0.01
Cameras	0.01
LED lights	0.02
Leakage sensor	0.05
Batteries	0.000001

3.2.5 Conditional Probability Tables

The conditional probability tables (CPT) 3.3-3.7 are quantified based on the PHA. Table 3.4 shows the CPT for the failure of the propulsion system node. This table shows how critical is it in case of the failure of thruster module actuators as shown in red in any case of failure of thruster module actuators the probability of losing Eely is true as in confined environments the robot can't use its neutral buoyancy to float back to the surface. This is further illustrated in the sensitivity analysis subsection. Moreover, thrusters were one of the most susceptible components to failure as Eely operators at the Applied Underwater Robotics Laboratory (AUR Lab) have communicated that they have lost on average one thruster per year.

Table 3.3: CPT for Environmental complexity

Ocean current	TRUE				FALSE			
Dusty sediments	TRUE		FALSE		TRUE		FALSE	
Absence of natural light	T	F	T	F	T	F	T	F
TRUE	0.95	0.9	0.6	0.4	0.7	0.6	0.15	0.01
FALSE	0.05	0.1	0.4	0.6	0.3	0.4	0.85	0.99

Table 3.4: CPT for Failure of propulsion system

Failure of thruster module actuators	TRUE				FALSE			
Failure of joint module actuators	TRUE		FALSE		TRUE		FALSE	
Environmental complexity	T	F	T	F	T	F	T	F
TRUE	1	1	1	1	0.3	0.1	0.35	0
FALSE	0	0	0	0	0.7	0.9	0.65	1

Table 3.5: CPT for Failure of remote control

Failure of communication system	TRUE				FALSE			
Failure of operator intervention	TRUE		FALSE		TRUE		FALSE	
Environmental complexity	T	F	T	F	T	F	T	F
TRUE	0.4	0.3	0.3	0.2	0.1	0.01	0.05	0.01
FALSE	0.6	0.7	0.7	0.8	0.9	0.99	0.95	0.99

Table 3.6: CPT for Failure of autonomous control

Failure of propulsion system	TRUE		FALSE	
Failure of altitude control	TRUE	FALSE	TRUE	FALSE
TRUE	1	1	0.6	0
FALSE	0	0	0.4	1

Table 3.7: CPT for Loss of Eely

Failure of autonomous control	TRUE		FALSE	
Failure of remote control	TRUE	FALSE	TRUE	FALSE
TRUE	1	0.75	0.1	0
FALSE	0	0.25	0.9	1

3.2.6   Launching the BN Model

After gathering the failure probabilities data, the BN model is constructed using the software GeNIe 4.0, which allows interactive model building and learning, developed by Bayes Fusion company [40]. Figures 3.3 and 3.4 show the developed BNs for the two case scenarios.
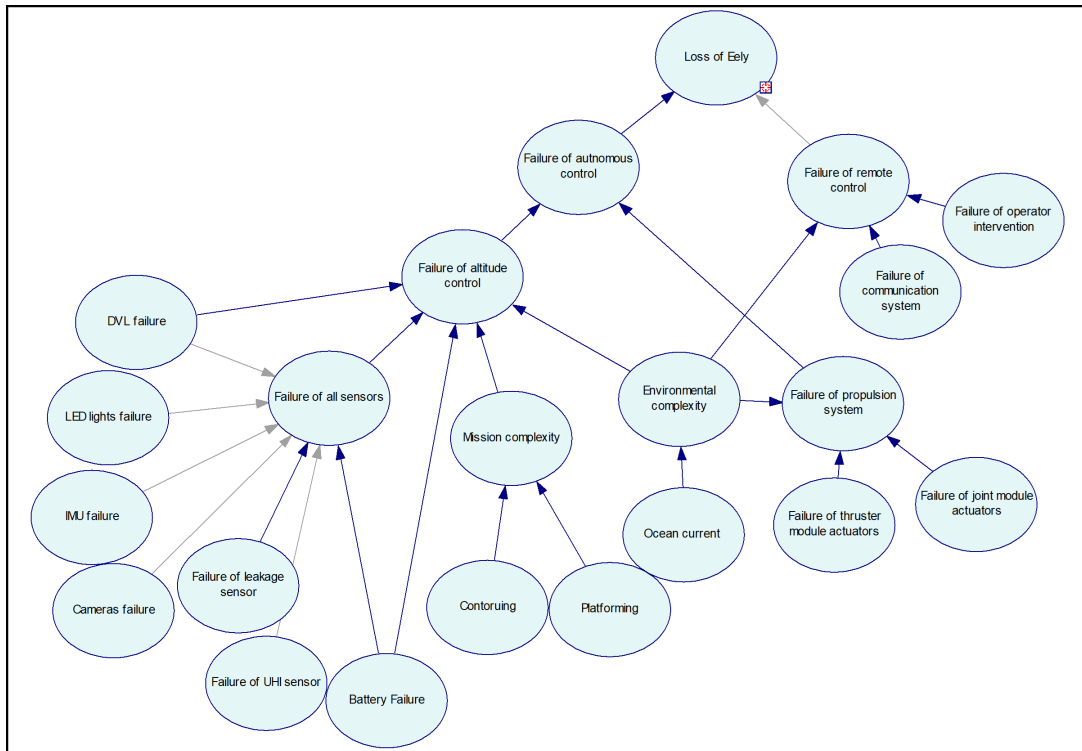
Figure 3.3: BN for Losing Eely during Seabed Mapping Operations
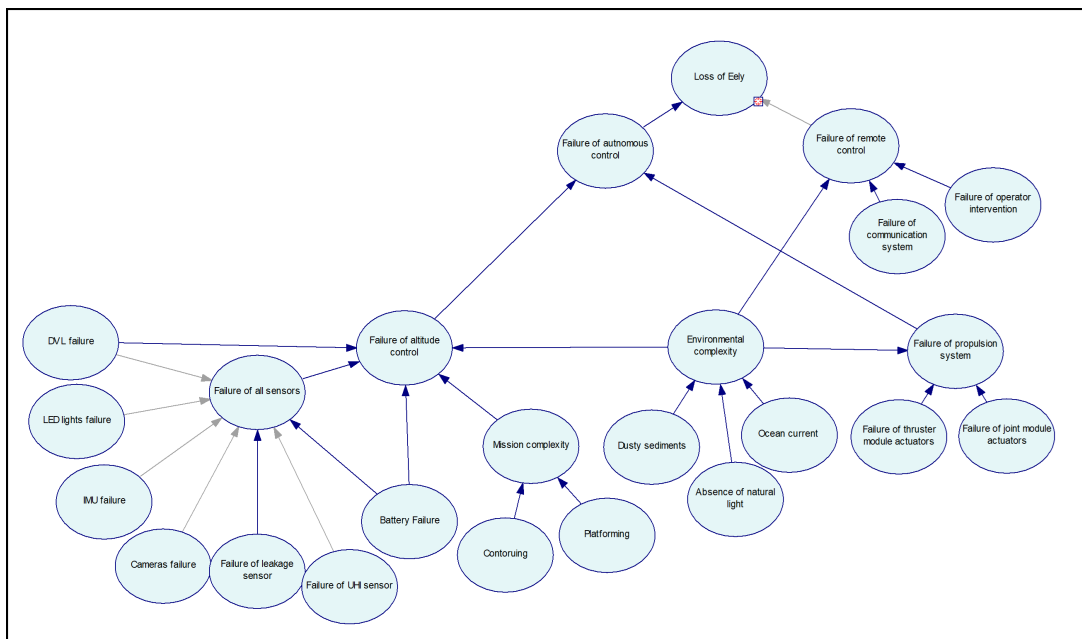
Figure 3.4: BN for Losing Eely during Confined Environments Operations

3.2.7   Dynamic Simulation

Figures 3.5 and 3.6 show the developed DBNs for the two case scenarios.

27
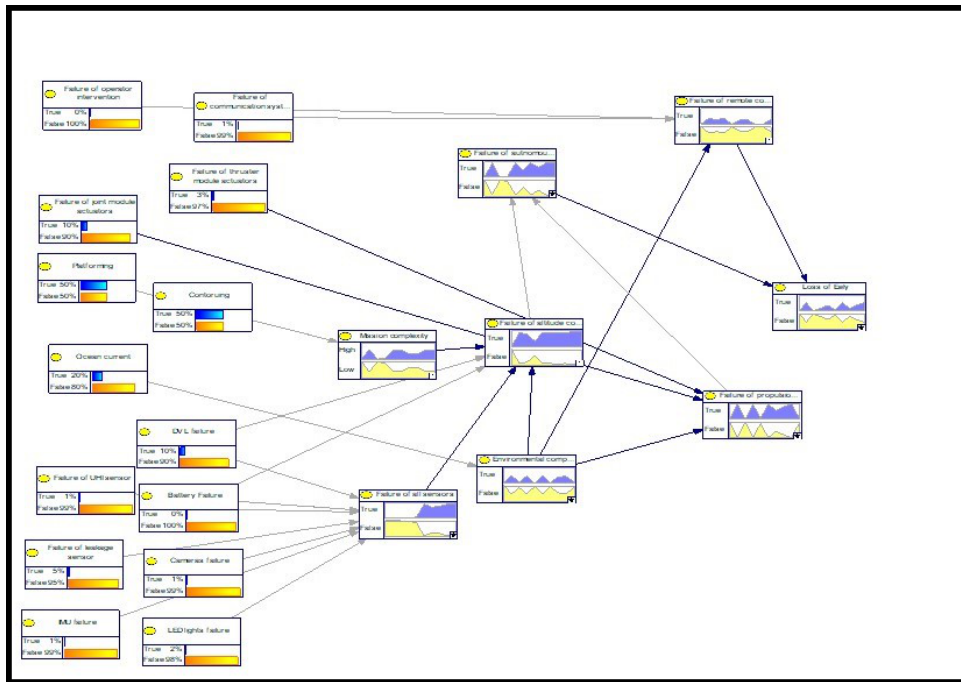
Figure 3.5: DBN for Losing Eely during Seabed Mapping Operations
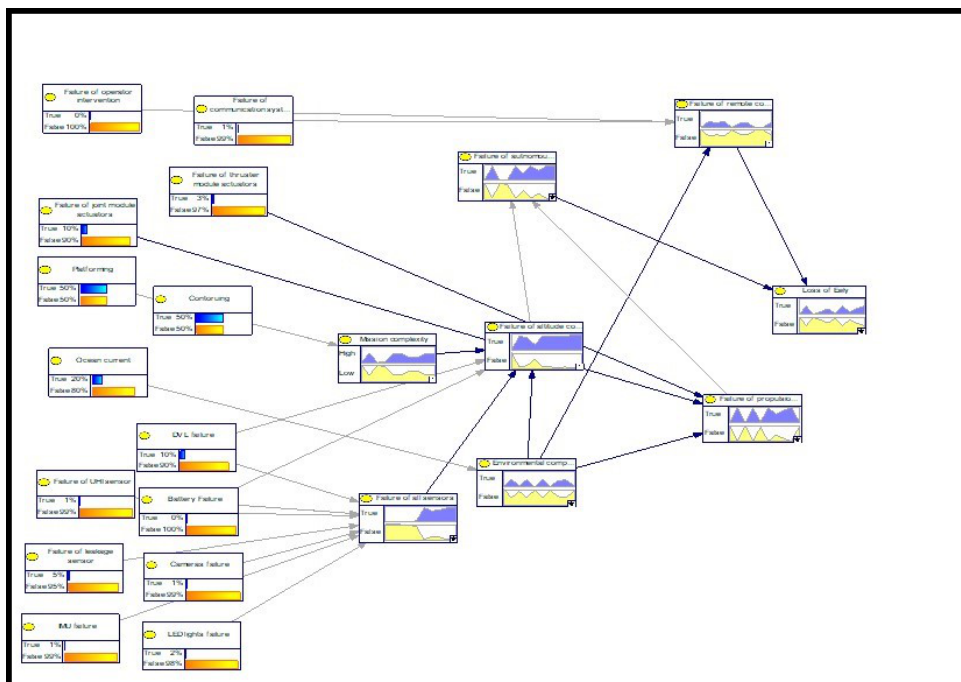
Figure 3.6: DBN for Losing Eely during Confined Environments Operations

The simulation results of the DBNs for the two case scenarios can be observed in Figures 3.7 - 3.8. The results indicate that the DBN can take into account changes over time and the likelihood of events occurring. In this regard, the probability of losing Eely in confined environments is higher than in seabed mapping due to various factors such as extreme pressures on the thrusters, poor communication with the vehicle, high mission complexity, and the complexity of the environment.

28

Time	0	1	2	3	4	5	6	7	8	9
True	0	0.5	0.082464657	0.49291932	0.0075615...	0.47928454	0.071891006	0.39130541	0.46153846	0.083333333
False	1	0.5	0.91753534	0.50708068	0.99243846	0.52071546	0.92810899	0.60869459	0.53846154	0.91666667

(a) Environmental Complexity

Time	0	1	2	3	4	5	6	7	8	9
High	0	0.6	0	0.09579219	0.6	0.56854628	0.32142857	0.38241285	0.6	0.6
Low	1	0.4	1	0.90420781	0.4	0.43145372	0.67857143	0.61758715	0.4	0.4

(b) Mission Complexity

Time	0	1	2	3	4	5	6	7	8	9
True	0	0.94	0	0.93929193	0.078761263	0.93792845	0.55377996	0.77379605	0.93615385	0
False	1	0.06	1	0.060708068	0.92123874	0.062071546	0.44622004	0.22620395	0.063846154	1

(c) Failure of Propulsion System

Time	0	1	2	3	4	5	6	7	8	9
True	0	0.35	0.28408146	0.34929193	0.0087064...	0.24829359	0.3071891	0.034823038	0	0.30833333
False	1	0.65	0.71591854	0.65070807	0.99129355	0.75170641	0.6928109	0.96517696	1	0.69166667

(d) Failure of Remote Control

Time	0	1	2	3	4	5	6	7	8	9
True	0	0	0	0.033586571	0.083333333	0.88528803	0.72887324	0.76869614	0.9	0.9
False	1	1	1	0.96641343	0.91666667	0.11471197	0.27112676	0.23130386	0.1	0.1

(e) Failure of All Sensors

Time	0	1	2	3	4	5	6	7	8	9
True	0	0.875	0.8	0.36631812	0.86805388	0.87581134	0.90477847	0.85623917	0.95429231	0.94635
False	1	0.125	0.2	0.63368188	0.13194612	0.12418866	0.09522153	0.14376083	0.045707692	0.05365

(f) Failure of Altitude Control

Time	0	1	2	3	4	5	6	7	8	9
True	0	0.9	0	0.083333333	0.9	0.45519087	0.9	0.65235527	0.9	0.9
False	1	0.1	1	0.91666667	0.1	0.54480913	0.1	0.34764473	0.1	0.1

(g) Failure of Autonomous Control

Time	0	1	2	3	4	5	6	7	8	9
True	0	0.531	0.0015181...	0.17157226	0.37400497	0.082124845	0.51130699	0.15426701	0.37	0.51183333
False	1	0.469	0.99848183	0.82842774	0.62599503	0.91787516	0.48869301	0.84573299	0.63	0.48816667

(h) Loss of Eely

Figure 3.7: Dynamic Simulation Results for Seabed Mapping Operations

Time	0	1	2	3	4	5	6	7	8	9
True	0	0.95	0.70553178	0.82608696	0	0.890625	0.95	0.93152293	1	0.95
False	1	0.05	0.29446822	0.17391304	1	0.109375	0.05	0.068477069	0	0.05

(a) Environmental Complexity

Time	0	1	2	3	4	5	6	7	8	9
High	0.083333333	0.40384615	0.9	0.64830508	0.70522388	0.79411765	0.83505155	0.86697248	0.92266187	0.9
Low	0.91666667	0.59615385	0.1	0.35169492	0.29477612	0.20588235	0.16494845	0.13302752	0.077338129	0.1

(b) Mission Complexity

Time	0	1	2	3	4	5	6	7	8	9
True	0.0011101...	0.985	0.78613998	0.9726087	0.89	0.9790625	0.985	0.96161196	0.99	0.985
False	0.9988898	0.015	0.21386002	0.027391304	0.11	0.0209375	0.015	0.038388043	0.01	0.015

(c) Failure of Propulsion System

Time	0	1	2	3	4	5	6	7	8	9
True	0	0.4	0.2656607	0.60793973	0.005690149	0.37313709	0.45368299	0.071938584	0	0.47910589
False	1	0.6	0.7343393	0.39206027	0.99430985	0.62696291	0.54631701	0.92806142	1	0.52089411

(d) Failure of Remote Control

Time	0	1	2	3	4	5	6	7	8	9
True	0.075559701	0.083333333	0.40384615	0.9	0.64830508	0.9	0.9	0.81593407	0.70522388	0.9
False	0.9244403	0.91666667	0.59615385	0.1	0.35169492	0.1	0.1	0.18406593	0.29477612	0.1

(e) Failure of All Sensors

Time	0	1	2	3	4	5	6	7	8	9
True	0	0.83898305	0.88167939	0.92444822	0.99	0.97058824	0.99	0.9867872	0.99	0.98959608
False	1	0.16101695	0.11832061	0.075551783	0.01	0.029411765	0.01	0.013212796	0.01	0.010403917

(f) Failure of Altitude Control

Time	0	1	2	3	4	5	6	7	8	9
True	0	0.9	0	0.14044238	0.86454104	0.67397463	0.9149248	0.83349585	0.90283958	0.9219928
False	1	0.1	1	0.85955762	0.13545896	0.32602537	0.085075202	0.16650415	0.097160424	0.078007198

(g) Failure of Autonomous Control

Time	0	1	2	3	4	5	6	7	8	9
True	0.01	0.593	0.019154136	0.56061045	0.13442855	0.45365809	0.6860779	0.39169736	0.37966184	0.73015723
False	0.99	0.407	0.98084586	0.43938955	0.86557145	0.54634191	0.3139221	0.60830264	0.62033816	0.26984277

(h) Loss of Eely

Figure 3.8: Dynamic Simulation Results for Confined Environments Operations

3.2.8   Sensitivity Analysis

The goal of sensitivity analysis is to identify the causes that have the most significant impact on the probability of losing Eely, and to limit these causes by introducing risk reduction measures. It also works as an indicator for adding more constraints and efforts for data collection. Decreasing the uncertainty of a cause that has little or no influence on the probability of losing Eely will result in a negligible change in the overall uncertainty value, making it of little importance. In our case, we aim to identify the top factors that influence the probability of losing Eely. Figures 3.9 - 3.10 show the sensitivity analysis results for losing Eely for the two case scenarios.

In the first case of seabed mapping operations shown in Figure 3.9, it can be seen that the probability of losing Eely is most sensitive to the failure of autonomous control. Other main factors are comprised of failure of thruster module, failure of altitude control, mission complexity, and DVL failure. The second case of sensitivity analysis is performed for confined environment operations and is shown in Figure 3.10. It can be seen that the failure of autonomous control is the most sensitive factor for losing Eely as well. Environmental complexity, failure of propulsion system, failure of altitude control, and mission complexity account for the remaining factors to which the loss of Eely is sensitive.
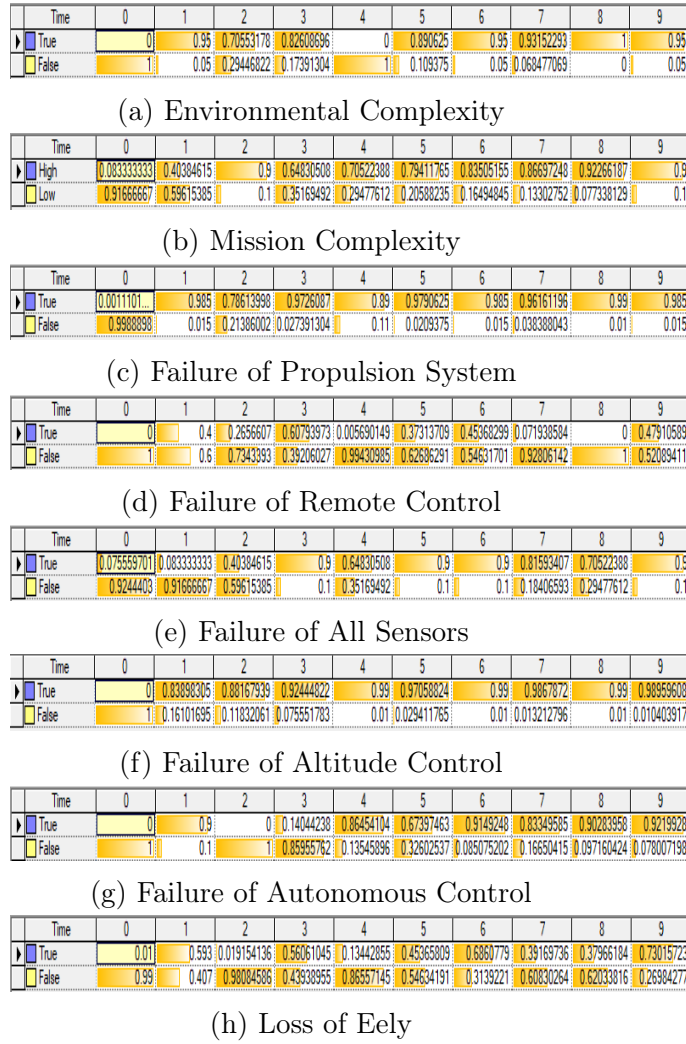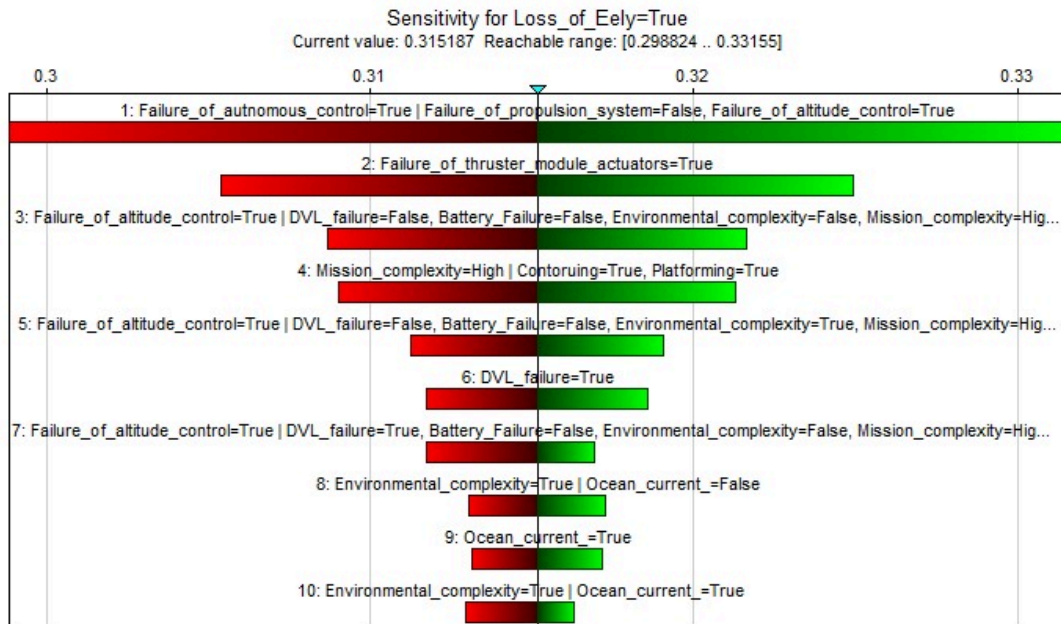
Figure 3.9: Sensitivity tornado diagram for losing Eely during Seabed Mapping Operations
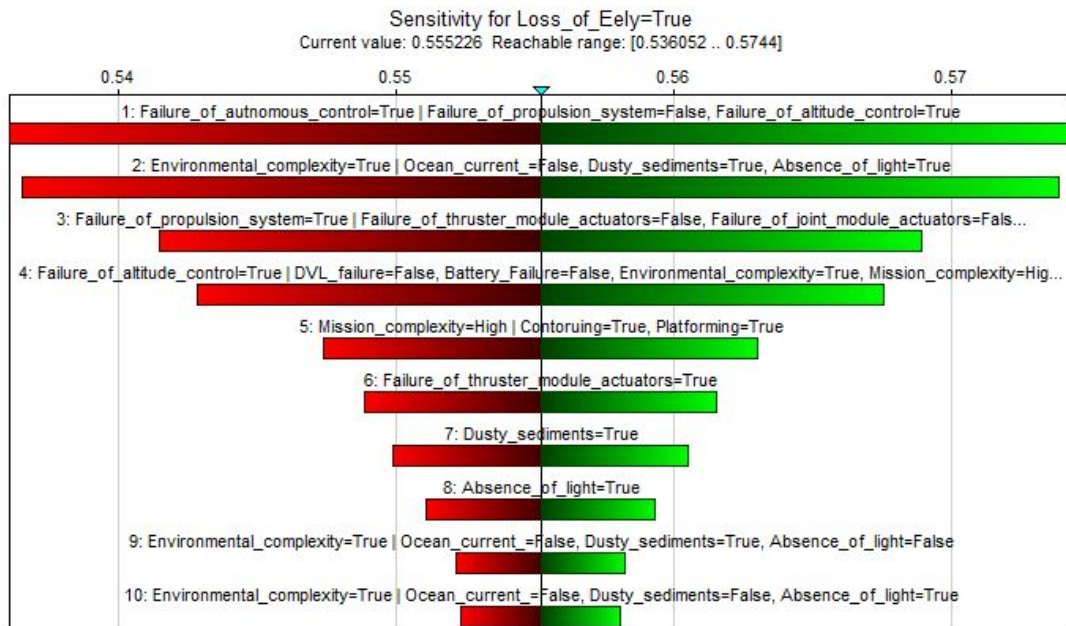

Figure 3.10: Sensitivity tornado diagram for losing Eely during Confined Environments Operations

3.2.9 Pros and Cons of the BN Model

The model looks upon almost Eely's entire system to avoid potential risks. Despite the fact that the model was built specifically for Eely, it can be transferred to the operations of other autonomous underwater vehicles. On the other hand, the model has some limitations, such as not including all of the possibilities with details which can cause the loss of Eely and not completely extending some nodes. For instance, nodes such as

31

failure of communication system and failure of operator intervention, the latter being a non-technical node, could be further developed, and other non-trivial factors could have been included in the model. For such expansion, it would require searching for more data including human and organizational factors and their influence on mission risk, which would take a significant amount of time and resources, having the current model seem to be adequate for the two investigated case scenarios. Moreover, DBN is time dependent where the state of a variable at one time depends on its previous states and the states of other variables and it can be computationally expensive to compute more time steps, and GeNIe is only limited to 1000 time step [40].

3.3 Discussion

From the results of the DBN and sensitivity analysis, improving the robustness of the autonomous control part would significantly decrease the risk of losing Eely robot during different operations. Regarding seabed mapping operations, from the sensitivity tornado graph in Figure 3.9 shows that improving the thruster module actuators and altitude control systems would also substantially reduce the risk of losing Eely.

As for confined environments operations, the sensitivity tornado graph in Figure 3.10 indicates that, except for environmental and mission complexity, improving the robustness of the thruster module actuators, propulsion system, and altitude control system would also significantly reduce the risk of losing Eely. The uncertainties associated with confined environments environmental complexity are reflected in the DBN in Figure 3.6 as they affect critical nodes, and in Tables VII-VIII in the Appendix of Paper 1 as they are the main reason for a high rpn, mainly for DVL failure and Controller failure.

Altitude Control of Underwater Snake Robot

This chapter will present and describe the altitude Control method based on for local sea floor geometry approximation from the DVL sensor measurements based on [41] and [42]. Two Control methods will be applied to Eely, the nonlinear PID and the nonlinear FOPID.

4.1   Altitude and Sea Floor Gradient

Figure 4.1 shows Eely fully submerged above the seabed. Eely position in the $\{n\}$ frame is $p = [x_p, y_p, z_p]^T$
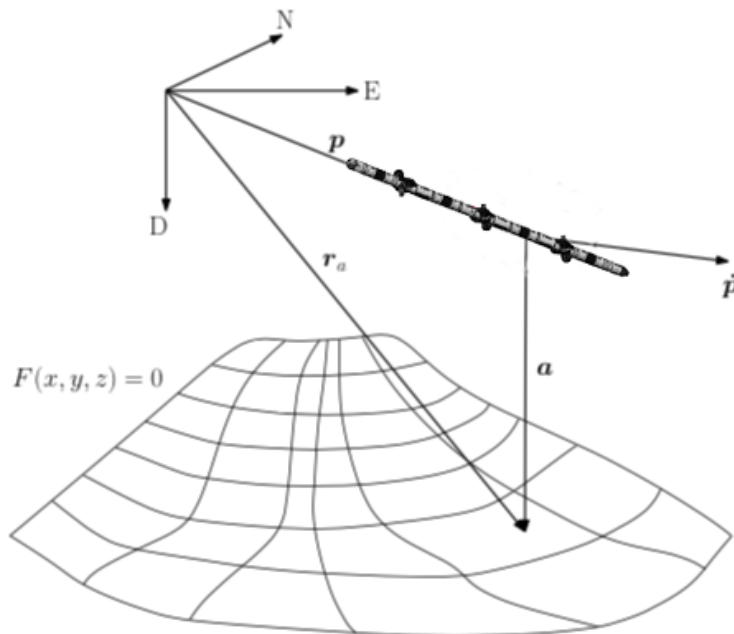

Figure 4.1: Eely above the Seabed in the NED-frame. Adopted from [13]

The NED-frame velocity vector $\dot{p}$ can be expressed as:

$$\dot{p} = R_b^n(\Theta_{nb})v \tag{4.1}$$

where $\Theta_{nb} = [\phi, \theta, \psi]^T$ is the altitude vector, $R_b^n(\Theta_{nb})$ is the rotation matrix from $\{b\}$ to $\{n\}$ frame, and $v = [u, v, w]^T$ is the velocity vector in $\{b\}$ frame.

Seabead is assumed to be a surface expressed by the following equation:

$$F(x, y, z) = f(x, y) - z = 0, \quad \frac{\partial F}{\partial t} = 0 \tag{4.2}$$

4.1.1 Altitude

The altitude is defined as the length of the vector from the center of origin (CO) of Eely to the point on the seabed with the same horizontal coordinates as the CO.

Eely's depth z_p is the vertical distance from the sea surface to the CO of Eely. This should not be confused with the water depth or altitude. The altitude vector is expressed as:

$$a = r_a - p = \begin{bmatrix} x_p \\ y_p \\ f(x_p, y_p) \end{bmatrix} - \begin{bmatrix} x_p \\ y_p \\ z_p \end{bmatrix} = \begin{bmatrix} 0 \\ 0 \\ f(x_p, y_p) - z_p \end{bmatrix} \tag{4.3}$$

where r_a is is the NED position of the point on the seabed below the CO of Eely, as shown in Figure 4.1. The altitude length can be written as:

$$a = f(x_p, y_p) - z_p = F(x_p, y_p, z_p) \tag{4.4}$$

From Equation 4.4, the altitude can be expressed by the same function F as the seabed, when F is evaluated at Eely's position.

4.1.2 Altitude Rate of Change

The altitude rate of change is given in Proposition 4.1.1, which is valid for 6 DOFs motion.

Proposition 4.1.1.

$$\dot{a} = \nabla F(p) \cdot \dot{p} \tag{4.5}$$

where $\nabla F(p) = \left[\frac{\partial f}{\partial x}\big|_{x_p, y_p}, \frac{\partial f}{\partial y}\big|_{x_p, y_p}, -1 \right]$ is the gradient vector of Equation 4.2 at the horizontal position (x_p, y_p) of Eely. The proof for Equation 4.5 is given as follows

Proof 4.1.1. The expression for the altitude rate of change is shown in Equation 4.6 using partial derivatives of a and chain rule.

$$\begin{aligned} \dot{a} = D_t a(\boldsymbol{p}(t)) &= D_t \left[a\left(x_p(t), y_p(t), z_p(t) \right) \right] \\ &= \frac{\partial a}{\partial x_p} \cdot \frac{dx_p}{dt} + \frac{\partial a}{\partial y_p} \cdot \frac{dy_p}{dt} + \frac{\partial a}{\partial z_p} \cdot \frac{dz_p}{dt} \end{aligned} \tag{4.6}$$

34

Substituting from Equation 4.4 in Equation 4.6, the altitude rate of change becomes:

$$\dot{a} = \frac{\partial f}{\partial x_p} \cdot \frac{dx_p}{dt} + \frac{\partial f}{\partial y_p} \cdot \frac{dy_p}{dt} - \frac{dz_p}{dt} \tag{4.7}$$

Since $x = x_p$ and $y = y_p$ in the function f presented in Equations 4.2 and 4.4. So, the partial derivatives $\frac{\partial f}{\partial x_p} = \frac{\partial f}{\partial x}\big|_{x_p, y_p}$ and $\frac{\partial f}{\partial y_p} = \frac{\partial f}{\partial y}\big|_{x_p, y_p}$. The altitude rate of change becomes:

$$\dot{a} = \left[\frac{\partial f}{\partial x}\bigg|_{x_p, y_p}, \frac{\partial f}{\partial y}\bigg|_{x_p, y_p}, -1 \right] \cdot \begin{bmatrix} \dot{x}_p \\ \dot{y}_p \\ \dot{z}_p \end{bmatrix} = \nabla F(p) \cdot \dot{p} \tag{4.8}$$

where $\nabla F = \left[\frac{\partial f}{\partial x}, \frac{\partial f}{\partial y}, -1 \right]$ if $F = F(x, y, z) = f(x, y) - z = 0$.

Equation 4.5 can be written as Equation 4.9 which shows how the altitude rate of change is related to the seabed from the gradient vector, and to Eely attitude and velocity vector.

$$\dot{a} = \left[\frac{\partial f}{\partial x}\bigg|_{x_p, y_p}, \frac{\partial f}{\partial y}\bigg|_{x_p, y_p}, -1 \right] \boldsymbol{R}_b^n \left(\boldsymbol{\Theta}_{nb} \right) \begin{bmatrix} u \\ v \\ w \end{bmatrix} \tag{4.9}$$

4.2 DVL Measurements

The DVL sensor is used to measure Eely's velocity over the seabed and to measure the altitude. DVL uses accoustic beams in a Janus configuration, these beams are transformed the DVL fixed frame $\{d\}$ to $\{b\}$ and finally to $\{n\}$.

4.2.1 DVL Beams and Kinematics

The used DVL has 4 acoustic beams in a Janus configuration is proposed in order to decrease the influence of the vehicle inclination [43]. The DVL j^{th} beam with its paramters is shown in Figure 4.2a. The jth is represented by vector r_j^d expressed in Equation 4.10 and it goes from the DVL to the seabed.
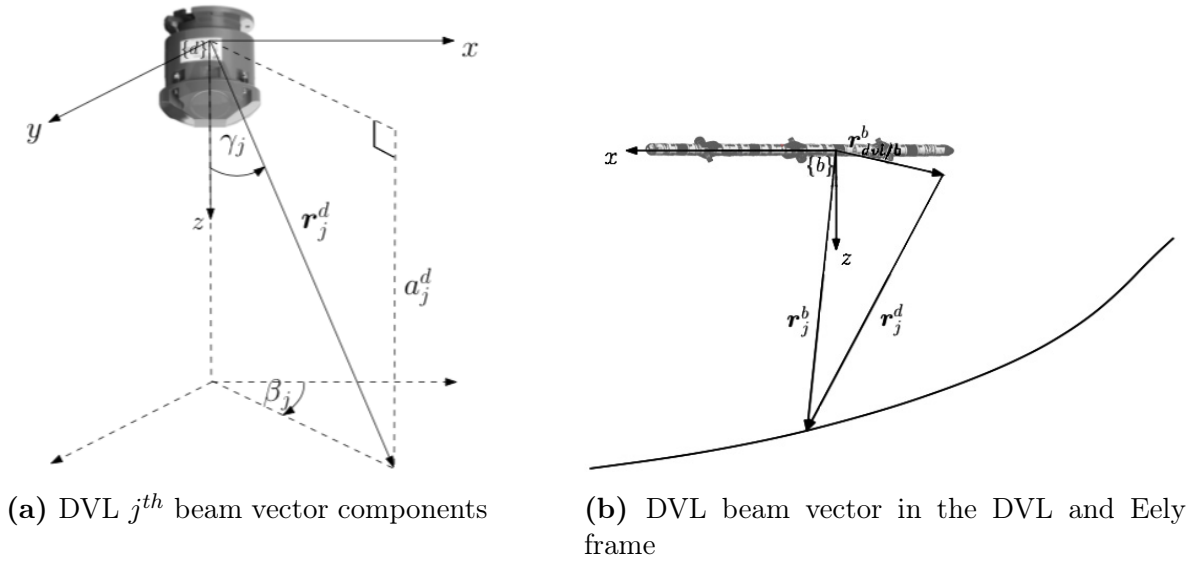
(a) DVL j^{th} beam vector components

(b) DVL beam vector in the DVL and Eely frame

Figure 4.2: The DVL beam components and beam vectors in the DVL and Vehicle frame. Adopted from [13]

$$\boldsymbol{r}_j^d = \begin{bmatrix} x_j^d \\ y_j^d \\ a_j^d \end{bmatrix} = a_j^d \begin{bmatrix} \tan\left(\gamma_j\right)\cos\left(\beta_j\right) \\ \tan\left(\gamma_j\right)\sin\left(\beta_j\right) \\ 1 \end{bmatrix} \tag{4.10}$$

where γ_j is the angle of the jth beam from the DVL z-axis, and β_j is the angle from the DVL x-axis. a_d^j is the vertical component of r_d^j, and r_d^j is expressed in terms of a_d^j and the constant angles γ_j and β_j. a_d^j is the measurement output from the DVL, and the vector with all 4 altitude measurements is noted as a^d.

4.2.2 Transformation of Beams

The vector r_d^j is transformed and shifted to $\{b\}$ frame in Equation 4.11, then transformed to $\{n\}$ frame in Equation 4.12. The first transformation and shift are illustrated in Figure 4.2b.

$$r_j^b = R_d^b(\Theta_{bd})r_j^d + r_{dvl/b}^b \tag{4.11}$$

$$r_j^n = R_b^n(\Theta_{nb})r_j^b \tag{4.12}$$

where Θ_{bd} is the orientation of $\{d\}$ relative to $\{b\}$. $r_{dvl/b}^b$ is the vector from CO of Eely to the DVL center in $\{b\}$ frame.

Finally, the 4 vectors from Eely CO to the seabed are given in $\{n\}$ as:

$$\boldsymbol{r}_j^n = \begin{bmatrix} x_j^n \\ y_j^n \\ a_j^n \end{bmatrix}, \quad j = 1, 2, 3, 4 \tag{4.13}$$

Equation 4.13 will be used to approximate the seabed geometry locally under Eely given that at least 3 DVL beams measurements are available.

4.2.3 Linear Approximation

A linear approximation function of the seabed requires at least 3 points. The linear seabed function is $f(x, y) = a + bx + cy$. In case all of the 4 DVL beams measurements are available, 4 different approximations can be calculated by different combinations of 3 of 4 beams. But, only one of the approximations must be chosen. It is advised to use the combination which gives the most preview while going forward as the forward looking beam will give some collision avoidance feature [13]. The seabed approximation using 3 DVL beams is obtained by solving Equation 4.14 to compute a_j, b_j, c_j.

$$
\begin{bmatrix} 1 & x_j^n & y_j^n \\ 1 & x_{j+1}^n & y_{j+1}^n \\ 1 & x_{j+2}^n & y_{j+2}^n \end{bmatrix} \begin{bmatrix} a_j \\ b_j \\ c_j \end{bmatrix} = \begin{bmatrix} a_j^n \\ a_{j+1}^n \\ a_{j+2}^n \end{bmatrix} \tag{4.14}
$$

4.3 Controllers

4.3.1 Speed Control

The surge, sway, heave, and yaw velocities of Eely are to be controlled using inputs from a joystick. The 4-DOF position and velocity vectors are given in Equations 4.15 and 4.16, respectively:

$$
\eta = \begin{bmatrix} u & v & w & r \end{bmatrix}^T \tag{4.15}
$$

$$
\nu = \begin{bmatrix} u & v & w & r \end{bmatrix}^T \tag{4.16}
$$

In this case, the control objective is to guide Eely by minimizing the error between the desired velocities provided by the joystick ν_{cmd} and the actual velocities of the vehicle ν. The actuator forces that are used to control the Eely's motion are given by:

$$
\tau = \begin{bmatrix} X & Y & Z & N \end{bmatrix}^T \tag{4.17}
$$

Joystick commands can be represented as a vector $\Theta^{js} = \begin{bmatrix} u^{js} & v^{js} & w^{js} & r^{js} \end{bmatrix}^T$, where each component of this vector corresponds to a different command, where u^{js} represent the surge command, v^{js} represent the sway command, w^{js} represent the heave command, and r^{js} represent the yaw command. The buttons corresponding to these commands are illustrated in Figure 4.3, and each command can take on values in the range [-1, 1], where a value of -1 represents the maximum negative command (for example, full reverse for the surge command), a value of 0 represents no command, and a value of 1 represents the maximum positive command (for example, full forward for the surge command).
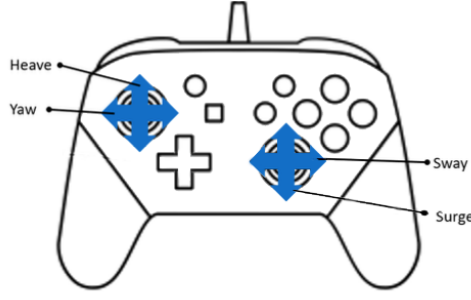
Figure 4.3: Commands given by the Controller

The commanded speed of Eely will be proportional to the joystick commands, and can be expressed as:

$$\nu_{cmd} = K_{js}^{\nu} T_{js}^{b} \Theta^{js} \tag{4.18}$$

where $K_{js}^{\nu} \in \mathbb{R}^{4 \times 4}$ is a diagonal scaling matrix that determines the maximum command velocity in each direction, and $T_{js}^{b} \in \mathbb{R}^{4 \times 4}$ is a transformation matrix that maps the joystick reference to the BODY frame of Eely. In order to counteract potential roll and pitch moments that arise from these inputs, ν_{cmd} is expanded such that:

$$\nu_{cmd} = \begin{bmatrix} u_{cmd} & v_{cmd} & u_{cmd} & 0 & 0 & r_{cmd} \end{bmatrix}^{T} \tag{4.19}$$

This expanded form of ν_{cmd} allows the speed of Eely to be controlled using a Proportional Integral Derivative (PID) control law of the form:

$$\tau_c = -K_p \left(\nu_{cmd} - \nu \right) - K_i \int_0^{t'} \left(\nu_{cmd} \left(t' \right) - \nu \left(t' \right) dt' \right) - K_d \left(\dot{\nu}_{cmd} - \dot{\nu} \right) \tag{4.20}$$

where $K_P, K_I, K_d \in \mathbb{R}^{6 \times 6}$ are the proportional, integral, and derivative gains, respectively. In order to produce stable and realistic results, the controller must be carefully tuned by choosing appropriate values for the gains. The commanded speed is also saturated according to Equation 4.21. In this case, the proportional, integral, and derivative gains are chosen to be equal for translation in all directions and rotation in all directions, as shown in Equation 4.22. This simplifies the tuning process by reducing the number of gains that must be chosen, but may decrease the quality of the controller as the behavior of the system is likely different in different directions due to the different dimensions of the vehicle.

$$K_{js}^{\nu} = K_{js} I_4 \tag{4.21}$$

$$K_p = \begin{bmatrix} K_{p,\text{linear}} I_3 & \mathbf{0}_{3 \times 3} \\ \mathbf{0}_{3 \times 3} & K_{p,\text{angular}} I_3 \end{bmatrix} \tag{4.22}$$

4.3.2 Joint Torque Control

Joint torque control is used to control the body configuration of Eely. The desired joint angles are represented by $q_d = [\theta_{1_d}, ..., \theta_{(N-1)_d}]^T$, and the actual joint angles are represented by $q = [\theta_1, ..., \theta_{N-1}]^T$. The difference between the actual and desired joint angles is $\tilde{q} = q - q_d$. The joint angles can be controlled with the following PD control law [44]:

$$\tau_\theta = -K_{p,\theta}\tilde{q} - K_{d,\theta}\dot{\tilde{q}} \tag{4.23}$$

The commanded joint torques are represented by $\tau_\theta \in \mathbb{R}^{N-1}$, and the proportional and derivative gains are represented by $K_{p,\theta}$ and $K_{d,\theta} \in \mathbb{R}^{N-1 \times N-1}$. These are positive definite diagonal matrices. To control the joints, it is necessary to measure the joint angles. Rotary encoders can be used for this purpose. These encoders can be installed on each joint motor to measure the relative rotation angle of each joint.

4.3.3 Thrust Allocation

Thrust allocation involves distributing the control signal from a controller to the thrusters on a vehicle. The generalized 6 DOF control forces and moments τ can be distributed to the thrusters using Equation 4.24, where B is the input matrix, n is the number of inputs, and $r_{bpi}^b = [l_{xi}, l_{yi}, l_{zi}]^T$ are the lever arms. Lever arms refer to the distance from the CO of the body of Eely to the line of action of the force at each thruster.

$$\tau = \sum_{i=1}^{n} \begin{bmatrix} f_i^b \\ r_{bpi}^b \times f_i^b \end{bmatrix} = \sum_{i=1}^{n} \begin{bmatrix} F_{x_i} \\ F_{y_i} \\ F_{z_i} \\ l_{y_i}F_{z_i} - l_{z_i}F_{y_i} \\ l_{z_i}F_{x_i} - l_{x_i}F_{z_i} \\ l_{x_i}F_{y_i} - l_{y_i}F_{x_i} \end{bmatrix} = Bu \tag{4.24}$$

To control an Eely robot, we use r thrusters and $N - 1$ joints, giving us a total of $n = r + N - 1$ inputs. The commanded forces and moments, represented by τ_c are 6 DOF, while the commanded joint torques are represented by τ_θ. The forces and moments applied to the robot from the joint motors and thrusters can be described as follows:

$$\begin{bmatrix} \tau_\theta \\ \tau_c \end{bmatrix} = B_{tot}u_{tot} = \begin{bmatrix} B & B_*(q) \end{bmatrix} \begin{bmatrix} u \\ u_* \end{bmatrix} \tag{4.25}$$

The vectors $u \in \mathbb{R}^{N-1}$ and $u* \in \mathbb{R}^r$ contain the joint motor forces and thrust forces, respectively. These vectors represent the inputs to the system. The matrix $B \in \mathbb{R}^{6 \times N-1}$ represents the input map for the joint motor forces, while $B_*(q) \in \mathbb{R}^{6 \times r}$ represents the thruster configuration matrix that maps the desired control forces and moments to the thrusters. Note that the position and orientation of the thrusters relative to the base of Eely can change as the joints rotate, so $B_*(q)$ must be recomputed when Eely's shape changes, while B remains constant [45]. It is possible to find geometric Jacobians that map the forces and moments τ_{t_j} from the thruster frames $\{t_j\}$ to the BODY frame $\{b\}$ of Eely, as shown in Equations 4.26 and 4.27:

$$\tau(q) = \sum_{j=1}^{r} J_{t_j}^{T}(q)\tau_{t_j} \tag{4.26}$$

$$\tau_{t_j} = \begin{bmatrix} 1 \\ \mathbf{0}_{5\times1} \end{bmatrix} u_{thr_j} \tag{4.27}$$

The scalar force applied by each thruster u_{thr_j} can be used to find the forces $\tau_b(q)$ acting on the BODY frame placed at the head link. The selection matrix $H = [I_{6\times6} \quad 0_{6\times N}]$ can be used to express $\tau_b(q)$ as:

$$\tau_b(q) = H\tau(q) = \sum_{j=1}^{r} H J_{t_j}^{\top}(q)\tau_{t_j} = \sum_{j=1}^{r} \left(Ad_{bt_j}^{-1}\right)^{T} \tau_{t_j} \tag{4.28}$$

where $Ad_{bt_j}^{-1}$ is the inverse map between the BODY frame and the thruster frame. Equation 4.28 can be re-written as:

$$\tau_b(q) = \sum_{j=1}^{r} B_j(q)u_{thr,j} \tag{4.29}$$

where,

$$B_j(q) = \left(Ad_{bt_j}^{-1}\right)^{\top} \begin{bmatrix} 1 \\ \mathbf{0}_{5\times1} \end{bmatrix} = \begin{bmatrix} R_{bt_j} & \mathbf{0}_{3\times3} \\ \hat{p}_{bt_j}\mathbf{R}_{bt_j} & R_{bt_j} \end{bmatrix} \begin{bmatrix} 1 \\ \mathbf{0}_{5\times1} \end{bmatrix} \tag{4.30}$$

The complete thruster configuration matrix can be expressed as:

$$\begin{bmatrix} B & B_*(q) \end{bmatrix} = \begin{bmatrix} B & B_1(q) & B_2(q) & \dots & B_r(q) \end{bmatrix} \tag{4.31}$$

This matrix is used to control the forces and moments applied by the thrusters, which in turn allows Eely to move and maneuver as desired.

4.4 Nonlinear PID Control

Let η_d denote the desired pose of the vehicle in the NED frame, which can be provided by a guidance law. The difference between the actual pose and the desired pose is represented by $e = \eta - \eta_d$. The control objective is to minimize e with a feedback loop that reaches the desired states. This can be accomplished with the following nonlinear Multiple Input Multiple Output (MIMO) PID control law:

$$\tau_c = -K_p J_{\Theta}^{-1} e - K_d J_{\Theta}^{-1} \dot{e} - K_i J_{\Theta}^{-1} \int_{0}^{t} e\left(t'\right) dt' \tag{4.32}$$

where τ_c represents the control torque, J_{Θ} is the Jacobian matrix, K_p, K_d, and K_i are the proportional, derivative, and integral gain constants, respectively, e is the error between

the reference signal and the system output, and $\dot{e}$ and $\int_0^t e(t')\,dt'$ represent the time derivative and the time integral of the error, respectively.

To achieve a more satisfactory response, a nonlinear PID controller has been developed. This controller replaces each term of the conventional PID controller with a nonlinear function $f(e)$, which is a combination of sign and exponential functions of the error signal [46]. The controller's derivative and integral are also modified using similar nonlinear functions and can be given as:

$$\begin{cases} U_{\text{NLPID}} = f_1(e) + f_2(e) + f_3\left(\int e\,dt\right) \\ f_i(\beta) = k_i(\beta)|\beta|^{\alpha_i}\,\text{sign}(\beta) \\ k_i(\beta) = k_{i1} + \frac{k_2}{1+\exp(\mu_i\beta^2)}, i = 1, 2, 3 \end{cases} \tag{4.33}$$

where β could be e, $\dot{e}$, or $\int e\,dt$, $\alpha_i \in \mathbb{R}^+$, the function $K_i(\beta)$ is a positive function with coefficients $K_{i1}, K_{i2}, \mu_i \in \mathbb{R}^+$.

4.5 Fractional Order Calculus and Control

4.5.1 Introduction

Podlubny [47, 48, 49] introduced fractional PID controller with integrator order λ and differentiator order μ which showed that the performance of Fractional dynamics performance becomes better with FOPID. In 2010, an interesting perspective to the subject, unifying all mentioned notions of fractional derivatives and integrals, was introduced and studied in [50, 51, 52]. After this work, different researchers composed FOPID controllers utilizing diverse outlines and tuning techniques. In [53] motion control of dynamical rigid body using FOPID showed the effect of fractional order controller on the dynamical response of the rigid body. The application fields of fractional calculus are increasingly widening, including areas such as electrical engineering, automation and control engineering, robotics [54], bio-medical engineering and recently the renewable energy domain introduced in [55].

The main motivation in fractional order operators and systems are their good performances, hereditary properties [56], and the recent advances in computer science and numerical tools allowed for FOPID to be implemented. The existing problems in altitude and motion control of underwater vehicles have prompted research into more effective control methods; therefore, different altitude tracking control approaches for UUVs have been proposed to achieve the best performance including high operational speed, high tracking accuracy (minimized tracking error), low energy consumption and smoothness of velocity control signal obtained. This section introduce the FOPID applied to the altitude controller to follow a specified sea mount and maintain a safe distance from the sea bed [57].

4.5.2 Fractional Order PID Controller $PI^\lambda D^\mu$

The FOPID controller was presented for the first time by Podlubny in 1999 [58]. The FOPID controller is a natural extension of the classical PID controller with an arbi-

trary order of its integration and differentiation actions [59]. With a more sophisticated controller, new design strategies are possible with the most flexible controller for plant with performance limitations. The differential equation of the $PI^\lambda D^\mu$ controller in time domain is described by:

$$U(t) = K_p e(t) + K_i D^{-\lambda} e(t) + K_d D^\mu e(t) \qquad (4.34)$$

Figure 4.4 shows that by selecting $\lambda = 1$ and $\mu = 1$, the nonlinear PID controller can be used. Selecting $\lambda = 1$ and $\mu = 0$ is equivalent to a PI controller, while selecting $\lambda = 0$ and $\mu = 1$ is equivalent to a PD controller. These are all special cases of the FOPID controller.
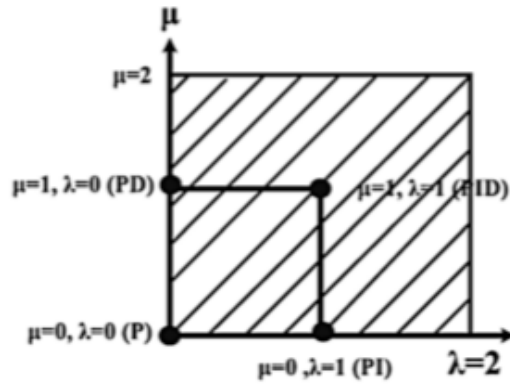

Figure 4.4: FOPID convergence graph

Figure 4.5 illustrates the plane of the integral and derivative actions of the PID controller. Obviously, the classical PID controller can be only represented by four points in the plane, while the FOPID controller is represented by the whole limited plane [60].
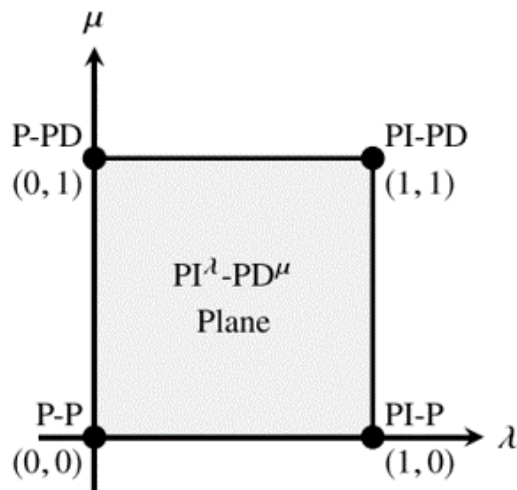

Figure 4.5: FOPID Plane

The transfer function of the fractional order PID controller ($PI^\lambda D^\mu$) is given by:

$$G_{FO-PID}(s) = K_p + \frac{K_i}{s^\lambda} + K_d s^\mu \tag{4.35}$$

where K_p, K_i, K_d are proportional, integral and derivative gains respectively. μ and λ are positive numbers that represent the order of differentiation and integration [56]. The control signal in the time domain representation given by:

$$u_{FO-PID}(k) = K_p e(k) + K_i D^{-\lambda} e(k) + K_d D^\mu e(k) \tag{4.36}$$

In order to find a series approximation for $s^{-\lambda}$ in terms of z^{-1} which has infinite direct current gain, first we write it as $s^{-\lambda} = (1/s) \times s^{1-\lambda}$ and then apply the Tustin method to it. Finally we get the following expression:

$$s^{-\lambda} = \left(\frac{2}{T}\right)^{-\lambda} \frac{1+z^{-1}}{1-z^{-1}} \sum_{n=0}^{N} f_n(1-\lambda)z^{-n} \tag{4.37}$$

where $f_n(1-\lambda)z^{-n}$ are again calculated as:

$$f_n(1-\lambda) = \frac{1}{n!} \times \frac{d^n}{dZ^{-1k}} \left(\frac{1-Z^{-1}}{1+Z^{-1}}\right)\bigg|_{Z^{-1}=0} \tag{4.38}$$

The following formulation for the discrete-time $\text{PI}^\lambda\text{D}^\mu$ controller:

$$G_c(z) = K_p + K_i \frac{1+z^{-1}}{1-z^{-1}} \sum_{n=0}^{N} f_n(1-\lambda)z^{-n} + K_d \sum_{n=0}^{N} f_n(\mu)z^{-n} \tag{4.39}$$

where

$$K_p = k_p, \, K_i = k_i \left(\frac{2}{T}\right)^{-\lambda}, \quad K_d = k_d \left(\frac{2}{T}\right)^\mu \tag{4.40}$$

By using the inverse z-transform, the difference equation relating $e(k)$ to $u(k)$ can be written as the following:

$$\begin{aligned}
u(k) =\ & u(k-1) + K_p[e(k) - e(k-1)] \\
& + K_i \sum_{n=0}^{N} f_n(1-\lambda)[e(k-n) + e(k-n-1)] \\
& + K_d \sum_{n=0}^{N} f_n(\mu)[e(k-n) - e(k-n-1)]
\end{aligned} \tag{4.41}$$

where N is number of Memory locations.

4.5.3 Nonlinear Fractional Order PID Controller (FOPID)

Figure 4.6 shows a block diagram which represent the FOPID control structure.
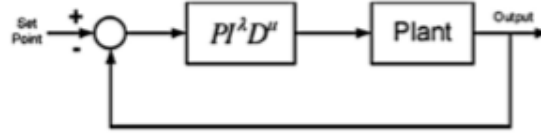

Figure 4.6: FOPID Controller block diagram

The nonlinear FOPID control law applied to Eely is expressed as:

$$\tau_c = -K_p J_\Theta^{-1} e - K_d J_\Theta^{-1} \dot{e}^\mu - K_i J_\Theta^{-1} \int_0^t \frac{e\left(t'\right) dt'}{\lambda} \tag{4.42}$$

The difference between PID and FOPID controllers is that, FOPID provides extra degree of freedom not only for the controller gains (K_p, K_i, K_d) but also for the orders of integral λ and derivative μ [56]. FOPID will increase the disturbance rejection of the system especially that Eely is operating at a turbulent flow environment (water).

Chapter 5

Simulator Implementation

This chapter presents the implementation and the simulations carried out during this work on Eely. The simulations were carried out using the Robotics Operating System (ROS) framework, Gazebo, and Plankton simulator.

5.1 ROS2

ROS2 was developed from scratch, and it is a complete new ROS with goals to make it more compatible with industrial applications compared to ROS1 which was dedicated to accelerating robotics research. ROS2 was built with the following design requirements [61] in order to make it ready for commercial use and adoption:

- Security — It needs to be safe with proper encryption where needed

- Embedded Systems — ROS2 needs to be able to run on embedded systems

- Diverse networks — Need to be able to run and communicate across vast networks since robots from LAN to multi-satellite hops to accommodate the variety of environments where robots could operate and need to communicate.

- Diverse networks — Need to be able to run and communicate across vast networks since robots from LAN to multi-satellite hops to accommodate the variety of environments where robots could operate and need to communicate.

- Real-time computing — Need to be able to perform computation in real time reliably since run time efficiency is crucial in robotics

- Product Readiness — Need to conform to relevant safety / industrial standards such that it ready for market

ROS2 is built as a decentralized framework compared to ROS1 which was centralized, meaning that there is a ROS Master node, which provides naming and registration services for other ROS nodes. In that way, ROS master node acts as the mediator for establishing connections between nodes, and if this connection dies, there is no way of communicating with other nodes. In ROS2, ROS master node was eliminated, because ROS2 uses DDS

which allowed for nodes to communicate with each other in a peer-to-peer fashion without the need for a mediator. Thus the system's fault tolerance increase as it don't have a single point of failure compared to ROS1 [62]. ROS2 infrastructure follows a publish-subscribe architecture, where nodes receive information by subscribing to a topic, and can send information by publishing messages to a topic. This structure allows the program to run multiple processes simultaneously, since none of the nodes need to know about the existence of other nodes [61].

5.2 Plankton Simulator

Simulations are carried out using Plankton open source simulator [63]. Plankton simulator is directed towards marine and maritime robotics researchers, aiming to simplify robotics research in these domains. The simulator runs using Gazebo and UUV Simulator [64] plugin in ROS2. Gazebo is an open source physics engine used to simulate robots and environments allowing the user to receive good visual information about how systems behave. It can also be used with several plugins, where the UUV Simulator is the most important one for this project. The UUV package have the required tools for simulating Unmanned Underwater Vehicles (UUVs), such as ROVs and AUVs. Also, the UUV Simulator has the ability to compute the thruster allocation matrix based on the placement of the thruster frames in relation to the base link.

5.3 Eely Platform in Simulation

The properties used for the Eely's model are from the Eely500 user manual. Parameters for the simulation model are given in Appendix Table A.1. Eely is simulated in its fully extended configuration having 5 links as shown in Figure 5.1.

Figure 5.1: Eely in torpedo shape with all modules

The topology of Eely can be represented by a connectivity graph [65]. For illustration, the connectivity graph of Eely is shown in Figure 5.2. Every node (vertex) in the connectivity

graph represents a reference frame with the same label, where frame {0} is the NED frame, and the superscript $*$ indicates the thruster frame. Physical parameters for Eely vehicle are shown in Table 5.1.

Table 5.1: Eely properties

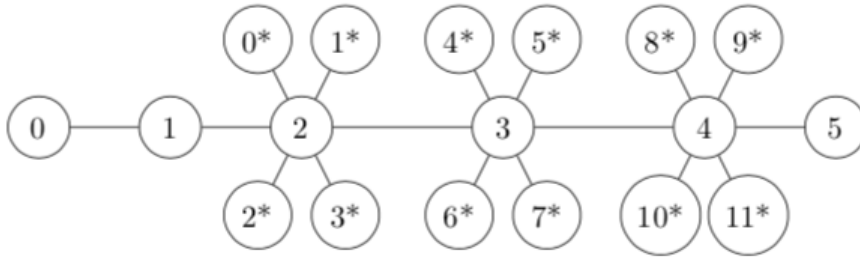| Parameter	Value	Unit
radius	100	mm
total length	6182	mm
total dry mass	199	kg
link 1 length	494	mm
link 2 length	1185	mm
link 3 length	1435	mm
link 4 length	1185	mm
link 5 length	740	mm
joint module	285	mm

Figure 5.2: Connectivity graph describing Eely. Adopted from [11]

The full simulation architecture is illustrated in Figure 5.3, which provides a simplified overview of the main topics and modules that the system relies upon. The basic components include signal processing, altitude controller, and thrust allocation. The YAML configuration file, shown on the right, offers an easy and human-readable approach to adjust and define various parameters without the need to modify the main code by the operator.
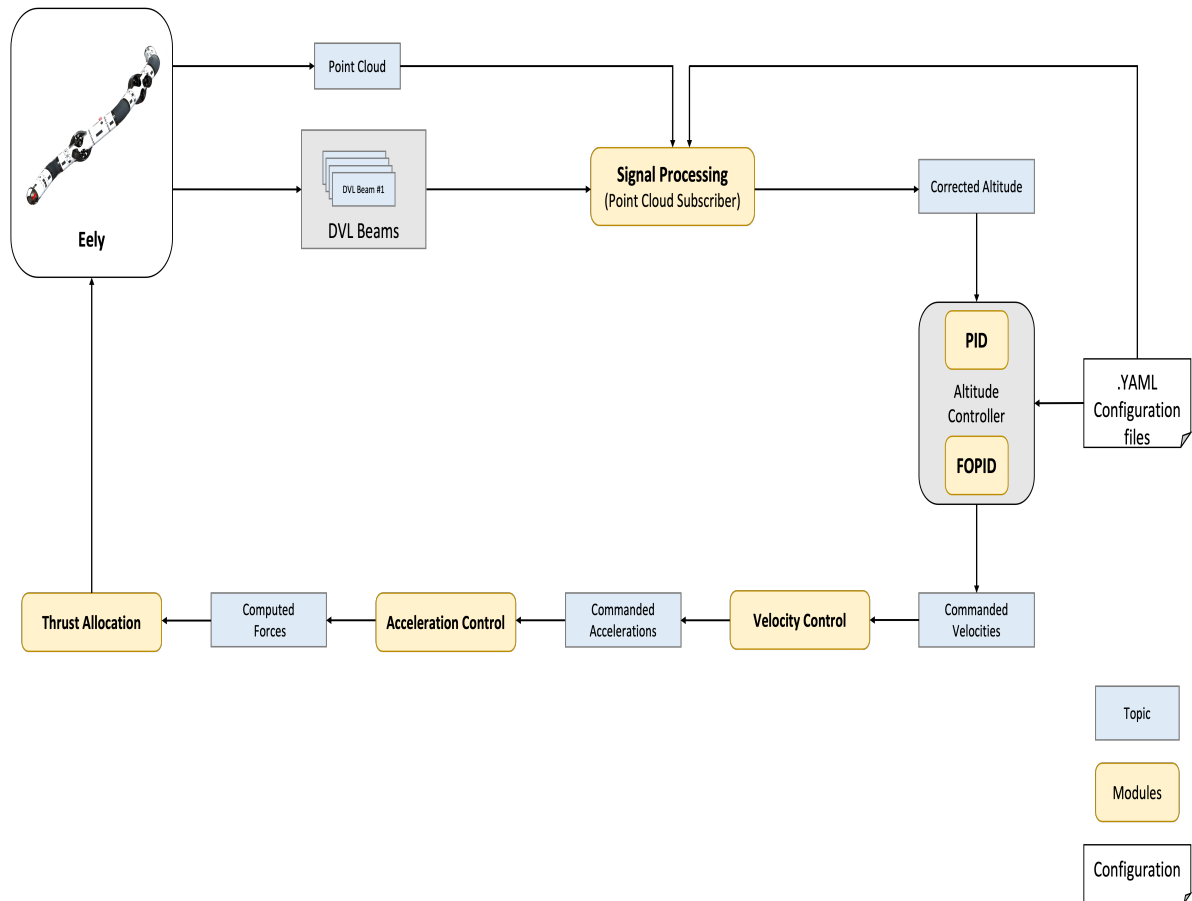
Figure 5.3: Simulation Architecture

5.4 Results

Figures 5.5 - 5.10 show the altitude control results for Eely using Proportional, PID, four
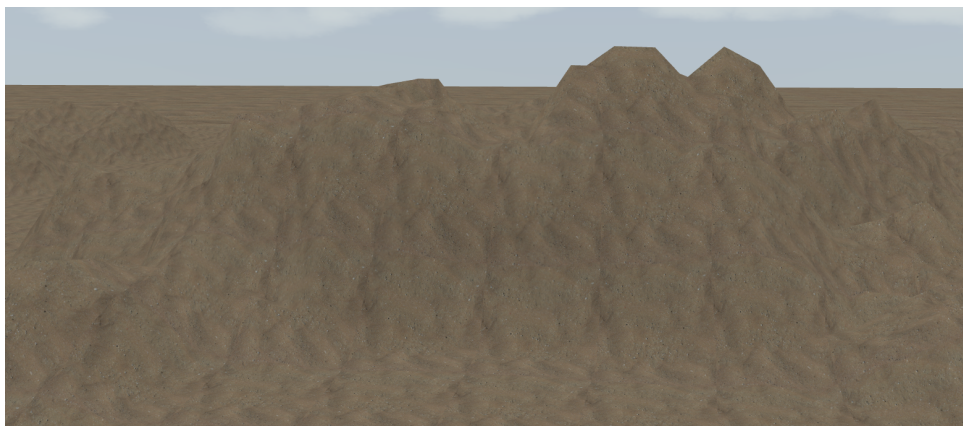FOPID controllers over a specified seamount shown in Figure 5.4.

Figure 5.4: Seamount to be mapped

5.4.1 Eely with Proportional Controller

(a) Thrusters output 0-3

(b) Thrusters output 4-7

(c) Thrusters output 8-11
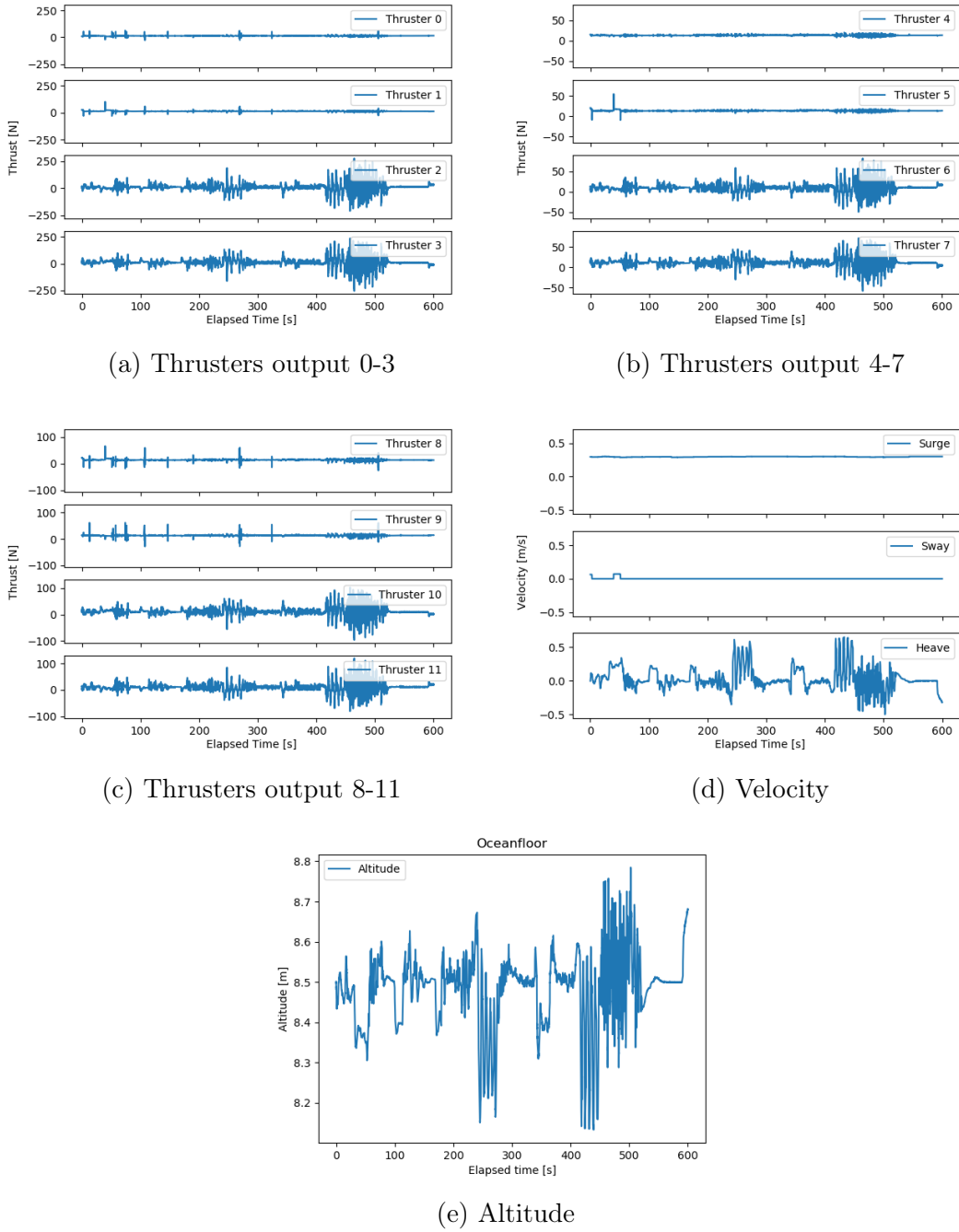
(d) Velocity

(e) Altitude

Figure 5.5: Altitude Control Simulation results of Eely with Proportional Controller

Figure 5.5 shows the results obtained from the Proportional controller. According to the results, Eely required more control forces to maintain its desired altitude, indicating that it may have had to use more energy to navigate through the seamount. It can be noticed that not all of the thrusters were utilized, which can contribute to the increased oscillations of Eely and the risk of losing thrusters.

5.4.2   Eely with PID Controller

(a) Thrusters output 0-3

(b) Thrusters output 4-7

(c) Thrusters output 8-11
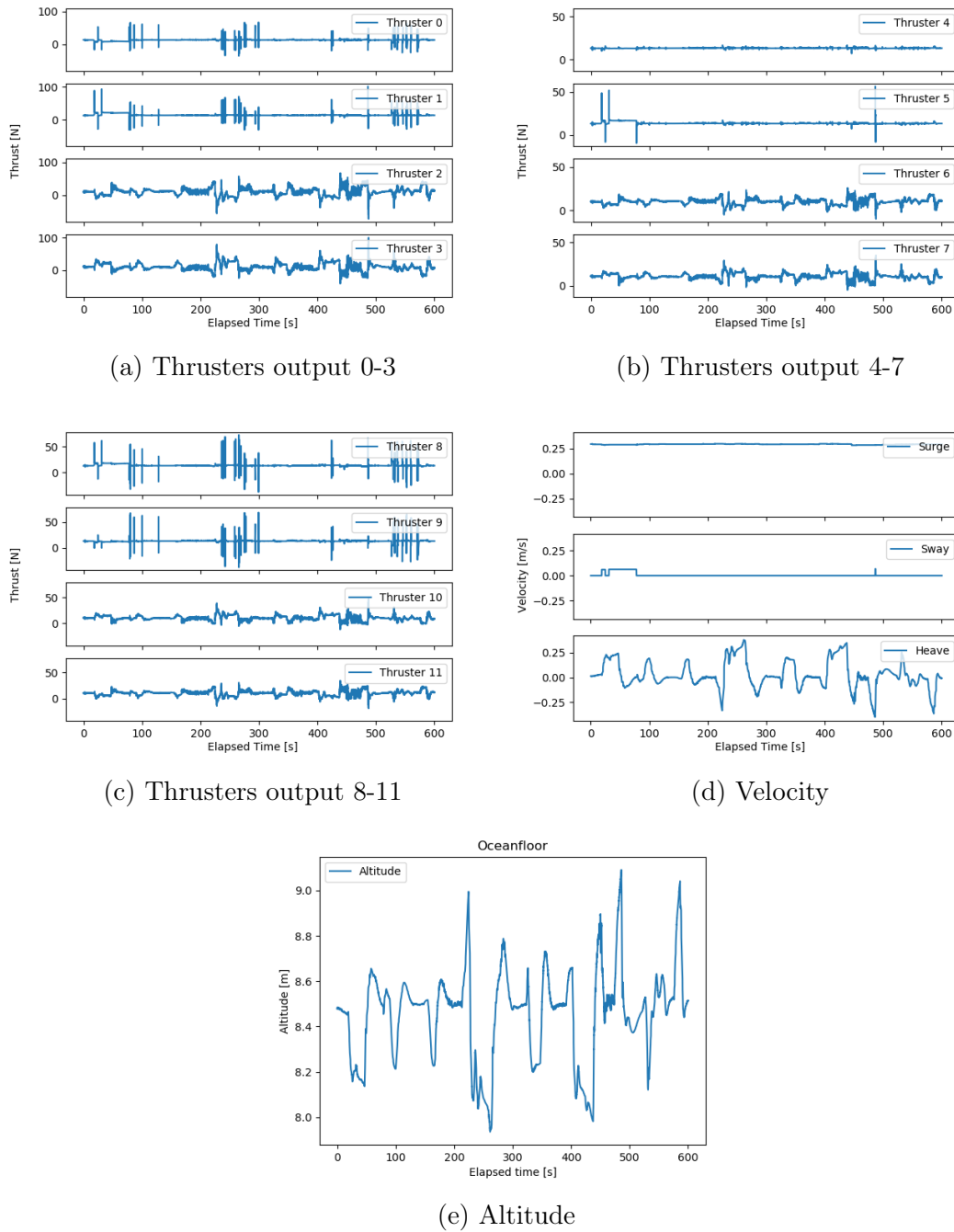
(d) Velocity

(e) Altitude

Figure 5.6: Altitude Control Simulation results of Eely with PID Controller

Figure 5.6 shows the results obtained from the PID controller. According to the results, Eely performed significantly better when using a PID controller. The settling time and oscillations were greatly improved compared to the previous simulation. Additionally, the thrusters were utilized more effectively, particularly in creating smoother thrust in the heave direction, compared to the previous simulation.
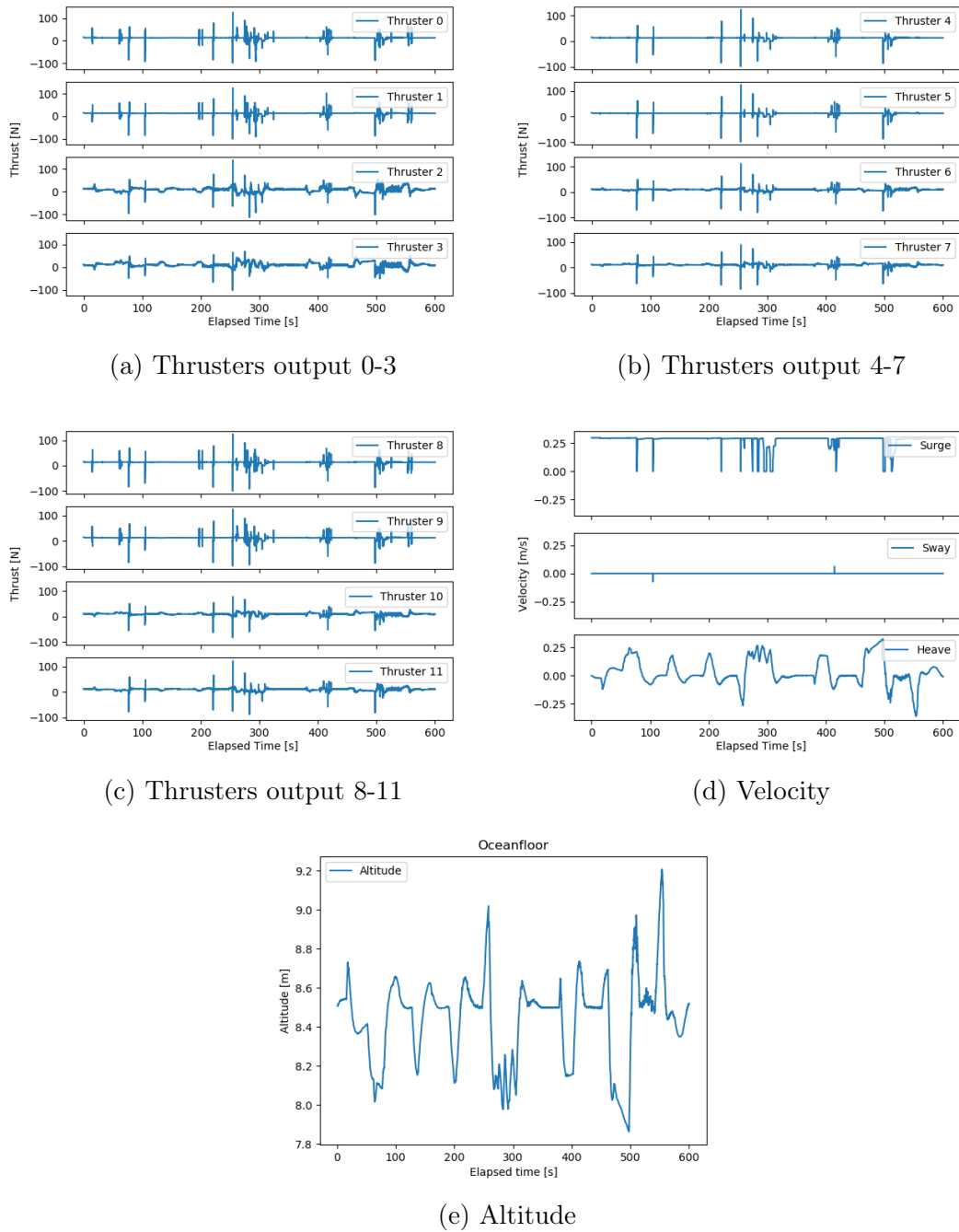
5.4.3 Eely with FOPID 1 Controller

(a) Thrusters output 0-3

(b) Thrusters output 4-7

(c) Thrusters output 8-11

(d) Velocity

(e) Altitude

Figure 5.7: Altitude Control Simulation results of Eely with FOPID 1 Controller

Figure 5.7 shows the results obtained from the FOPID 1 controller. According to the results, Eely performed slightly better than when using a PID controller in terms of adaptability to sudden changes caused by the unstructured variations in the seamount.

5.4.4   Eely with FOPID 2 Controller

(a) Thrusters output 0-3

(b) Thrusters output 4-7

(c) Thrusters output 8-11

(d) Velocity

(e) Altitude

Figure 5.8: Altitude Control Simulation results of Eely with FOPID 2 Controller

Figure 5.8 shows the results obtained from the FOPID 2 controller. According to the results, Eely performed slightly better than when using a PID controller in terms of adaptability to sudden changes caused by the unstructured variations in the seamount.

5.4.5 Eely with FOPID 3 Controller

(a) Thrusters output 0-3

(b) Thrusters output 4-7

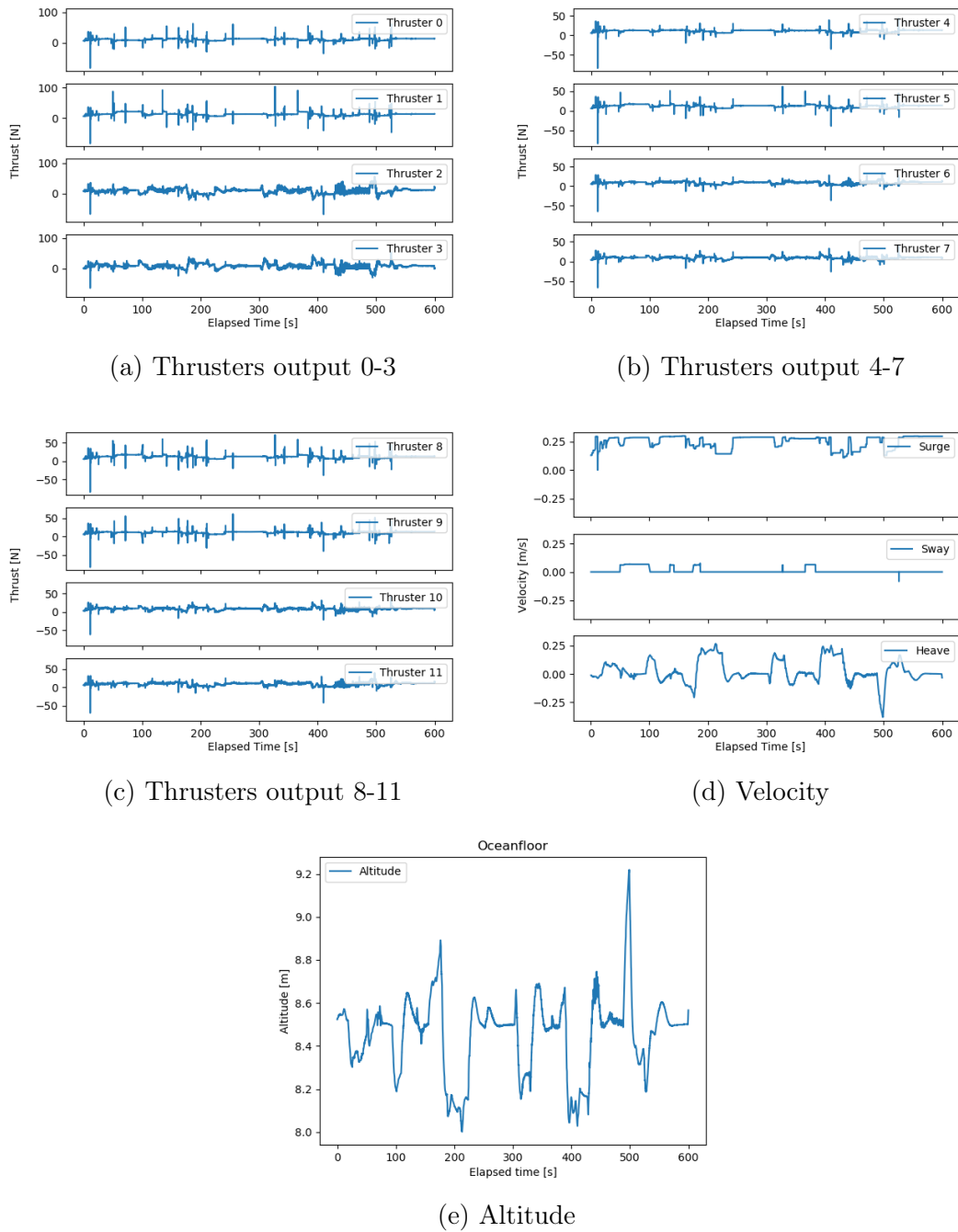(c) Thrusters output 8-11

(d) Velocity

(e) Altitude

Figure 5.9: Altitude Control Simulation results of Eely with FOPID 3 Controller

Figure 5.9 shows the results obtained from the FOPID 3 controller. According to the results, Eely performed slightly better than when using a PID controller in terms of adaptability to sudden changes caused by the unstructured variations in the seamount.
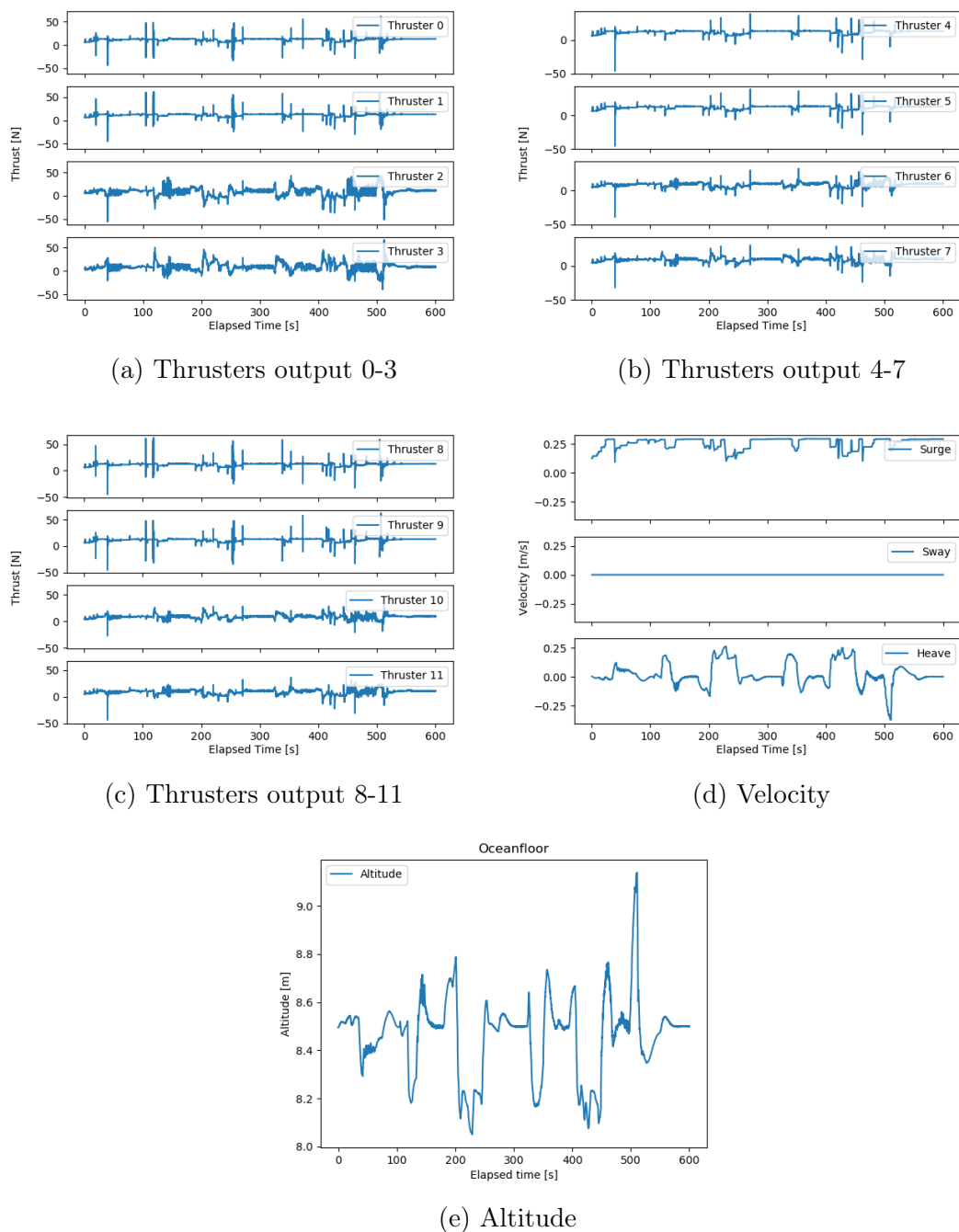
5.4.6 Eely with FOPID 4 Controller

(a) Thrusters output 0-3

(b) Thrusters output 4-7

(c) Thrusters output 8-11
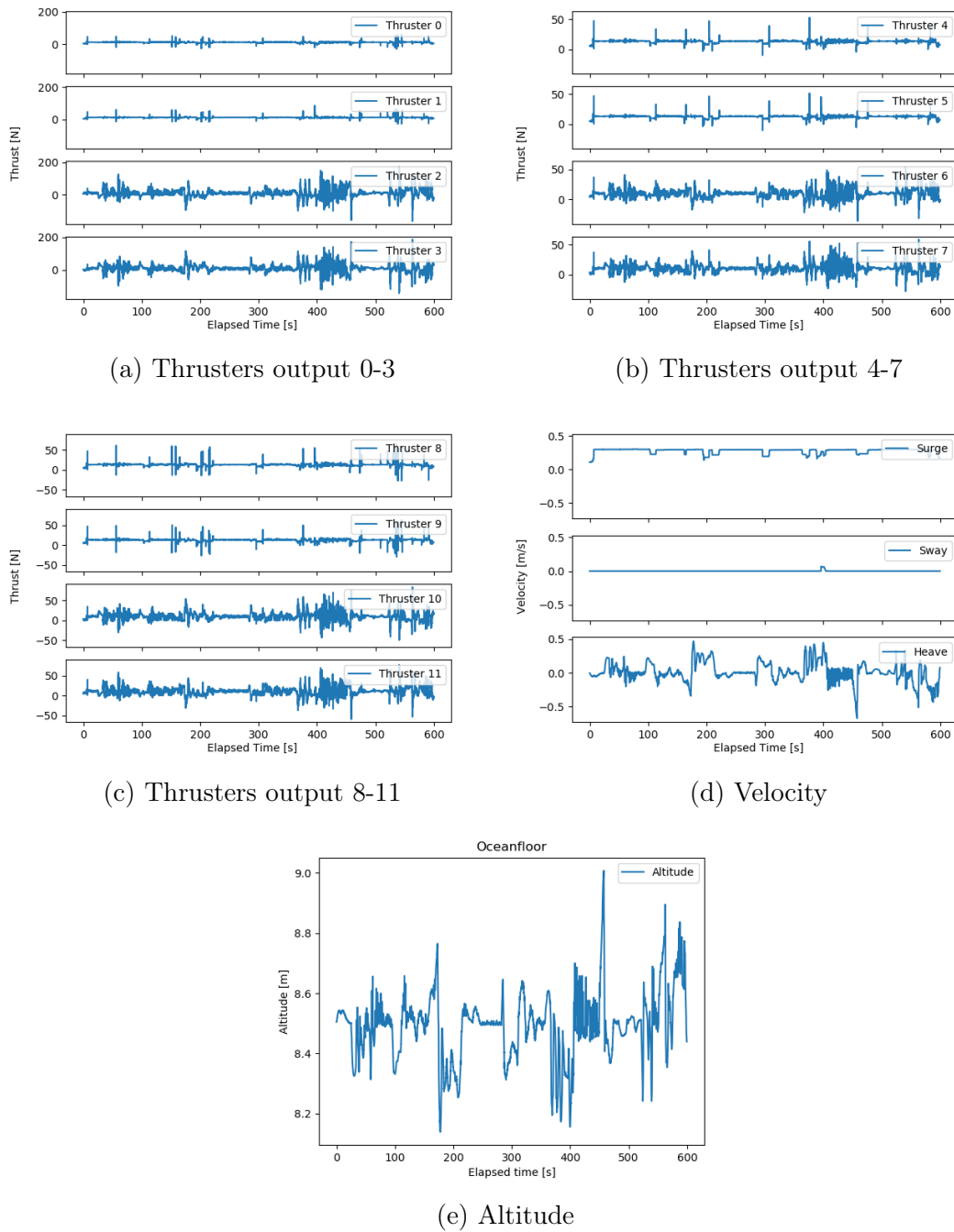
(d) Velocity

(e) Altitude

Figure 5.10: Altitude Control Simulation results of Eely with FOPID 4 Controller

Figure 5.10 shows the results obtained from the FOPID 4 controller. According to the results, Eely surpassed the PID controller and other FOPID controllers in terms of disturbance rejection and its ability to closely follow the intricate details of the unstructured seamount with minimal deviation from the desired setpoint of 8.5 m altitude, as demonstrated in Table 5.2.

5.5 Discussion

The simulation results presented in Figure 5.11 show the combined altitude outputs of Eely over a period of 10 minutes on the specified seamount using six different controllers, namely Proportional, PID, and four FOPID controllers.
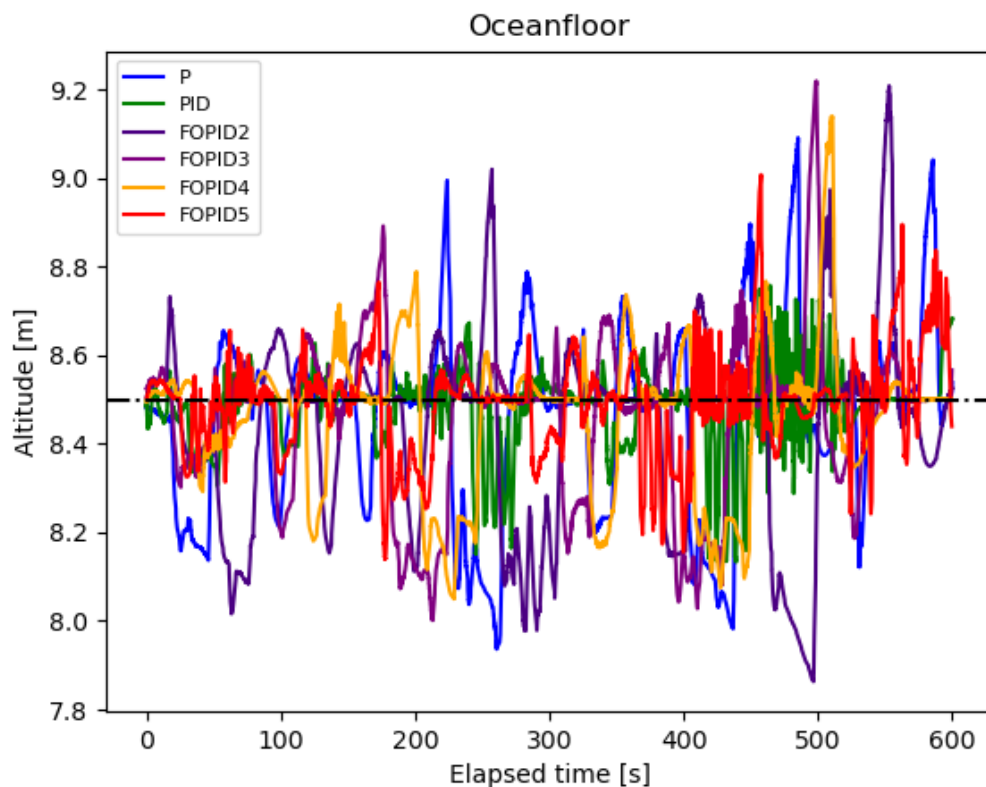

Figure 5.11: Combined Altitude results of different Controllers

The performance of different controllers combined with the altitude controller for Eely, the tracking error, and the power for each controller are shown in Table 5.2.

Table 5.2: Performance comparison of Controllers and Error

Controller	Controller Parameters					Error (%)	Power consumed (%)
	Kp	Ki	Kd	λ	μ		
Proportional	0.5	0	0	0	0	40	55
PID	0.5	0.2	0.05	1	1	20	12
FOPID 1	0.5	0.2	0.05	0.6	0.7	12	7.1
FOPID 2	0.5	0.2	0.05	0.4	0.7	5	5.2
FOPID 3	0.5	0.2	0.05	0.17	0.35	3	4.9
FOPID 4	0.5	0.2	0.05	0.2	0.6	1	60

The nonlinear PID gave satisfactory performance with 20% error from the specified altitude. It is clearly evident that nonlinear FOPID had superior altitude regulation performance in confined environments with 1% error from the specified altitude for FOPID 4 controller. This was demonstrated in the simulation results, which showed Eely's ability to map a steep part of a seamount with greater detail and precision as shown in Figure 5.12 which gives a close look on Eely while mapping a steep part of the seamount. The power comparison between each controller was computed based on [66]. A noticeable indication of power efficiency is that having very high tracking precision, but with high gain, is not necessarily good in terms of power efficiency. Precision may be sacrificed to reduce power consumption and increase operational time.

Figure 5.12: Eely mapping a Confined part of the Seamount with FOPID 4 Controller

The FOPID controller appears to be a promising option for controlling Eely Underwater Snake Robot, especially when over-shoot and settling time are important considerations, according to these results. FOPID was more resilient to disturbances and uncertainties, such as those brought on by outside environmental forces and measurement noise.

6

Chapter

Field Experiments

Field experiments with Eely were performed on April 26, 2023. The robot was launched from onboard RV Gunnerus in Trondheim Fjord, close to Trondheim Biological station. Figure 6.1 shows pictures of Eely taken during the field experiments.

Figure 6.1: Eely in Trondheim Fjord during the experiments

The position of the robot is measured with a HiPAP system installed on RV Gunners, which gives the acoustic position of Eely relative to RV Gunnerus. The global position is in turn measured with a GNSS system. This allows the north and east position of Eely to be given in Universal Transverse Mercator (UTM) coordinates [34]. This coordinate system divides the world into multiple zones that can be projected on a flat plane [67]. Each of these zones can be compared to a NED frame. Resulting north and east positions from the field experiments are given in this coordinate system, where the axes are scaled to make the results more readable.

The duration of the trials was approximately 50 minutes, and three successful recordings were captured. The recordings were taken in Coordinated Universal Time (UTC) because all GNSS satellites in a constellation carry atomic clocks that are synchronized to UTC by the network's ground stations [68].

The purpose of the field experiments was divided into two parts:

• For the control part of the thesis:

To test and record the log from Eely while doing altitude control with the same specified range from the seabed as the simulator, which is 8.5 meters. The objective area of interest was an unstructured surface similar to the one in the simulator to compare the behavior of Eely in the physical and simulated environment.

• For the risk part of the thesis:

To test the performance and capabilities of Eely for the proposed two case scenarios: seabed mapping and confined environments. For saftey issues, only the first case scenario for seabed mapping was considered. For the seabed mapping case: Eely was mapping the seabed in both contouring and platforming manner, monitor the performance of the thrusters as it was mentioned in the literature that usually there happens a thruster failure in one or more thrusters and from the field trials of Eely last year one of the thrusters also stopped working [34], to record the log from different sensors like the DVL-IMU-UHI-cameras to check their accuracy and the quality of the recorded data to be used to asses the failure probabilities of such sensors as there were not a clear failure probability for them in terms of being mounted on a vehicle like Eely.

6.1 Signal Processing

Signals produced by sensor measurements can vary in quality, and sometimes a measured signal may contain noise and errors. Controlling the signal quality is crucial to identify and remove errors in a system that relies on measured signals for direction and control. The observed signals from the field experiments contained a few errors. For example, Figure 6.7 shows a few sudden jumps or spikes in the measurements, which are known as wild points. A wild point is identified by determining whether a measurement significantly deviates from the prior measurements. As illustrated in Equation 6.1, a sampled value of a signal may be accepted if it is within a range around the calculated mean signal.

$$x[k] \in [\bar{x}_k - a\sigma, \bar{x}_k + a\sigma] \tag{6.1}$$

where $x[k]$ is a sample from a signal, $\bar{x}_k$ is the estimated mean signal, a is a scaling

factor, and σ is the standard deviation. If the sample $x[k]$ is rejected, it is replaced with an estimated mean value. The wild point check is illustrated in Figure 6.2.
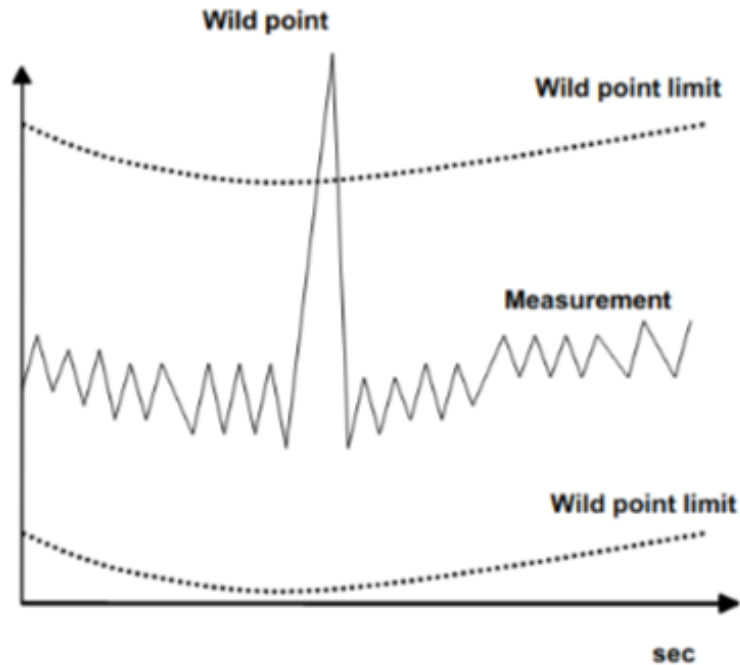

Figure 6.2: Wild point check [66]

6.2 Results

6.2.1 Altitude control

The results for measured altitude from the DVL of Eely are shown for a torpedo-shaped body configuration. The processed data is used to create altitude control plots similar to the ones obtained from the simulator for three trials, as shown in Figures 6.3, 6.5, and 6.7, respectively. Unfortunately, the data about velocities and thruster output were not available. Therefore, the analysis of the altitude tracking performance is based solely on the changes in position from the desired altitude set-point, which is 8.5 meters.

Figures 6.4, 6.6, and 6.8 shows the OOIs outputs of the seabed obtained from Eely during the three trials. These figures were obtained from the multibeam echosounder mounted on Eely and were processed using NaviScan Online and Helmsman softwares from EIVA [69].
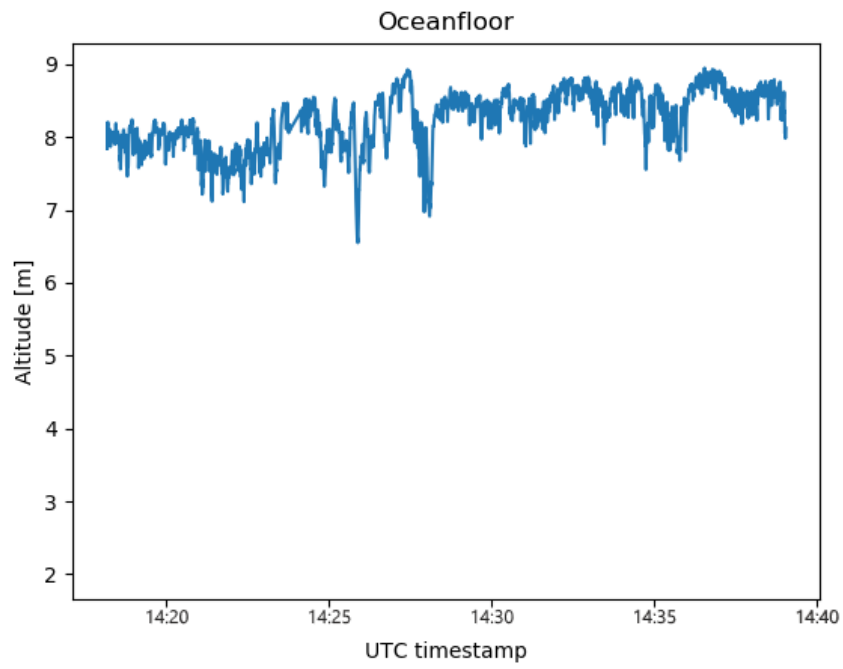
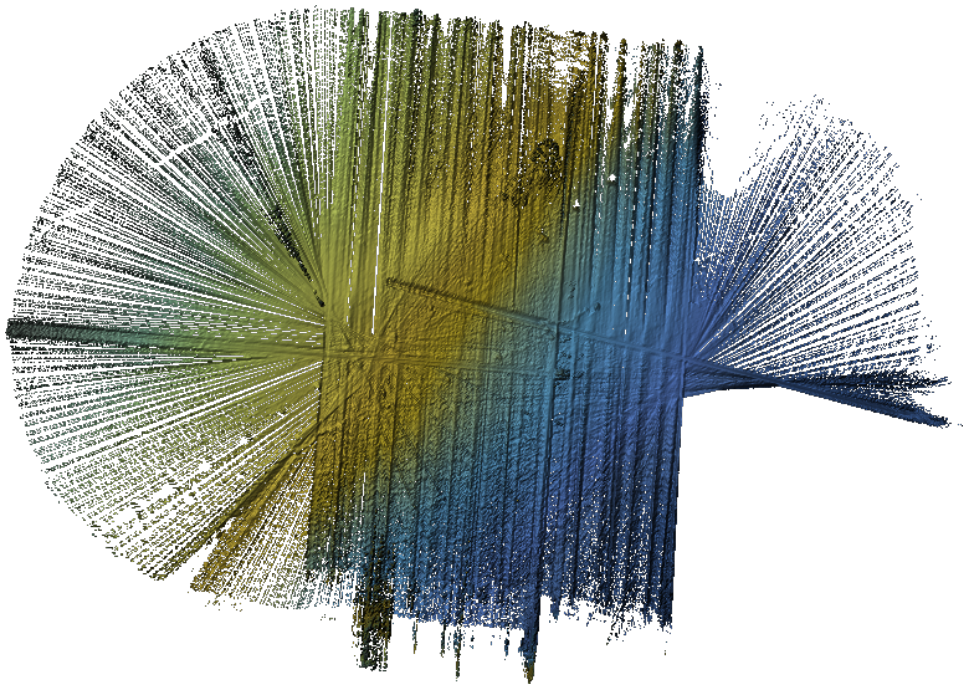**Figure 6.3:** Altitude Control of Eely Trial 1

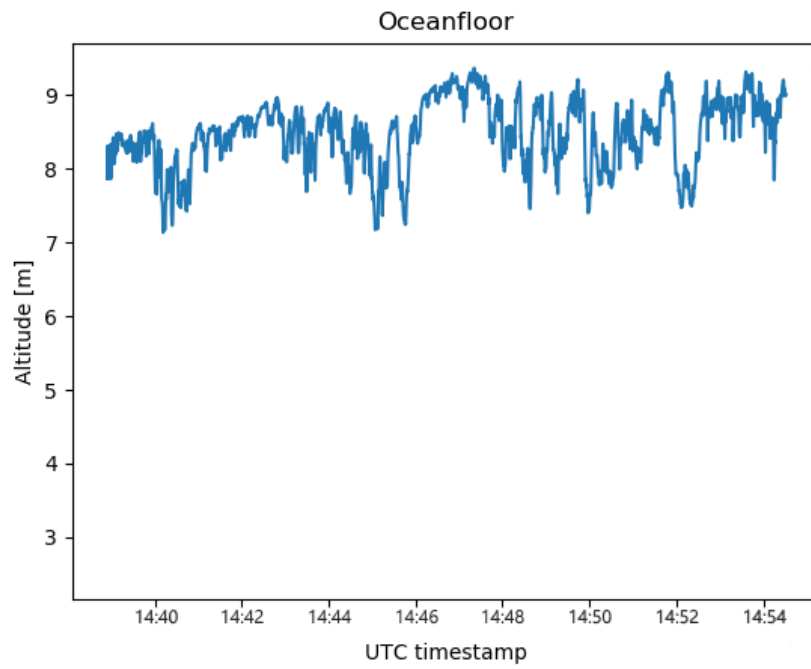**Figure 6.4:** Multibeam echosounder scan of Eely Trial 1
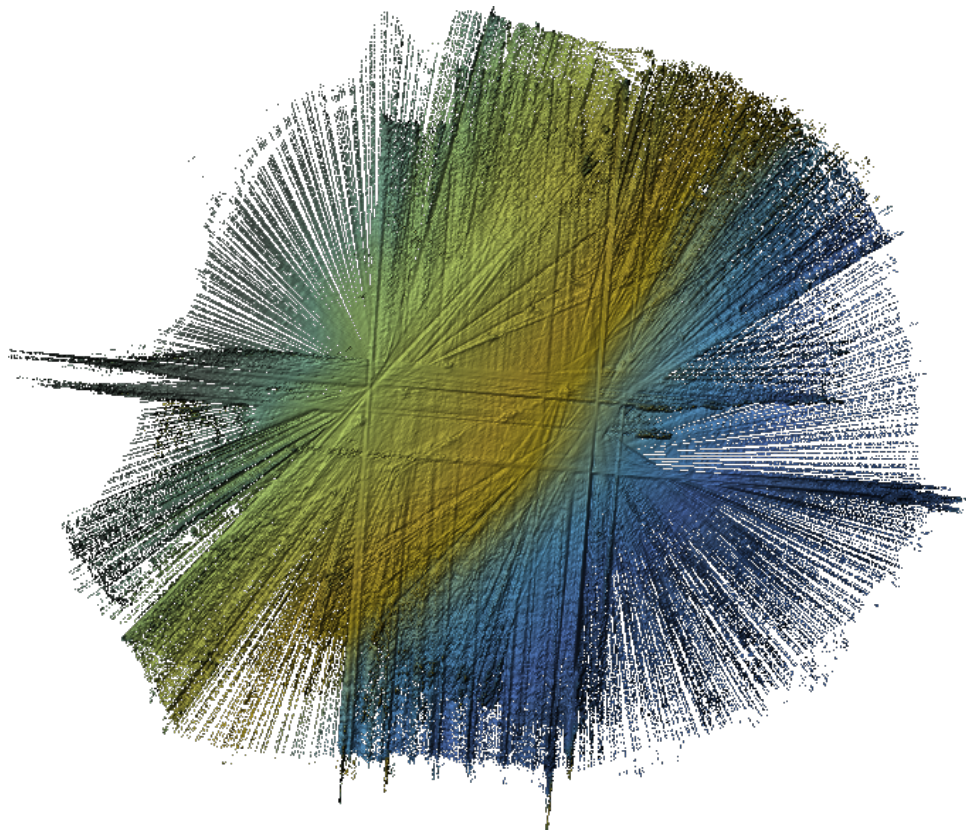
Figure 6.5: Altitude Control of Eely Trial 2

Figure 6.6: Multibeam echosounder scan of Eely Trial 2

61
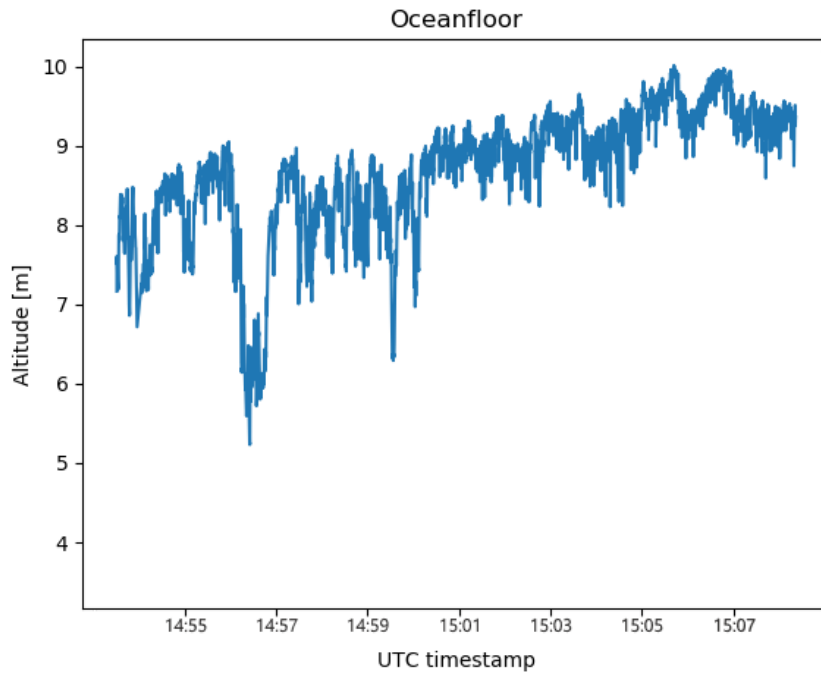
Figure 6.7: Altitude Control of Eely Trial 3
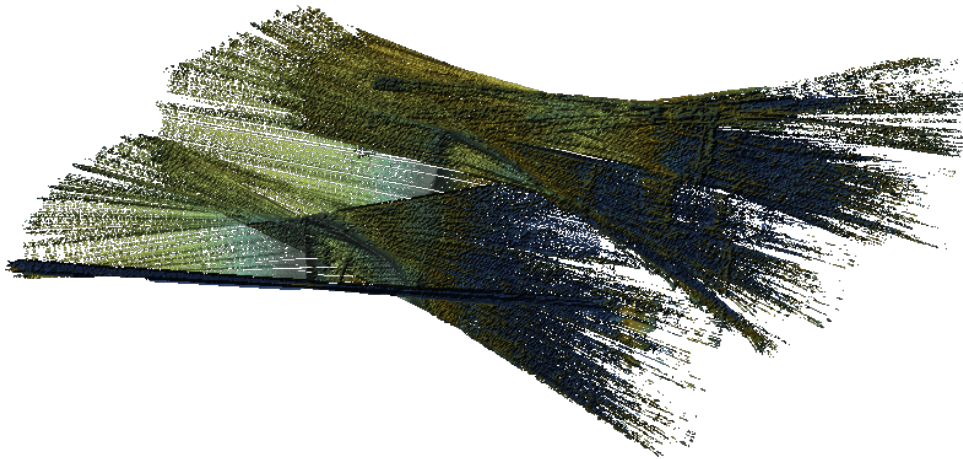
Figure 6.8: Multibeam echosounder scan of Eely Trial 3

6.2.2 Risk Assessment

The robot was controlled in a hybrid manner, utilizing a fiber optic cable connection as shown in Figure 6.9. This cable served the purpose of supplying power to the robot and transmitting a live feed from its cameras and sensors. The operator had the ability to intervene at any time and manually control the robot using a joystick.

However, after the first Altitude control trial, the robot experienced a sudden blackout, making communication and data reception from the robot and its sensors impossible. Our first suspicion regarding this blackout was related to a potential issue with the fiber cable itself. Given its high sensitivity, it could have become entangled or disconnected from the robot due to an excessive tension. To address the situation, we waited for the

robot to float back to the surface using its neutral buoyancy, and subsequently recovered it with the assistance of the lifting basket and the boat. We replaced the defected fiber cable with a new one and proceeded to deploy Eely back into the water, where it operated normally and successfully completed the remaining two trials. Apart from this particular incident, Eely encountered no problems with any of its thrusters or sensors throughout the experimental sessions.
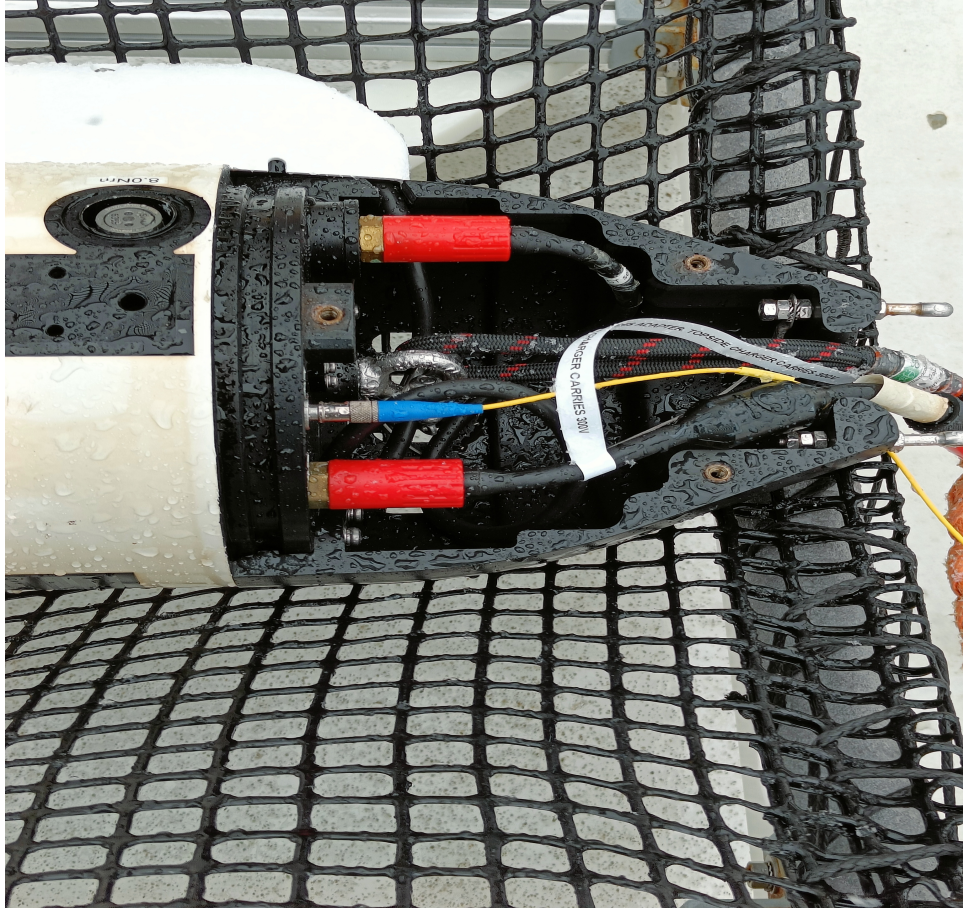
Figure 6.9: Fiber cable connected to Eely

6.3   Discussion

The goal of the field experiments was to validate the simulator and compare the simulated altitude capabilities of Eely with its real-world performance. However, it is evident that the simulations were conducted in an idealistic environment, free of significant sensor noise and harsh environmental conditions, unlike the challenging conditions encountered during the field experiments. Consequently, differences and challenges emerged in the field experiments that were not accounted for in the simulator.

Additionally, due to restrictions imposed by the manufacturing company, intervention in the low-level controller of the real robot was prohibited, which may explain the better altitude performance observed in the simulations.

Moreover, the current loads may be different compared to the simulator as there was no precise measurement of it, and the weather was changing during the field trial day.

Another noteworthy disparity between the simulations and the field experiments was the difference in their durations. While the simulations adhered to a fixed timing, the field experiments were subject to variable time frames dictated by practical constraints. This temporal inconsistency could have influenced the performance outcomes, particularly in dynamic and time-sensitive scenarios.

Tether management, a critical aspect for the real robot, was not taken into account in the simulator. Maneuvers may be required to avoid entanglement, a factor that was not considered in the simulated environment.

Chapter 7

Conclusions and Further Work

This chapter presents conclusions for the presented work, as well as recommendations for further work.

7.1 Conclusions

In this thesis, the challenges faced by Eely, an articulated underwater snake robot, operating in confined and demanding underwater environments was addressed. A Bayesian risk assessment approach was proposed to evaluate the risks associated with the loss of Eely during mission scenarios. Additionally, a nonlinear Fractional Order PID (FOPID) altitude controller was introduced to regulate and stabilize Eely's altitude underwater. Through comprehensive simulations, the effectiveness and robustness of the proposed controller in controlling Eely's altitude in diverse underwater conditions was demonstrated.

The results of the Bayesian risk assessment provided valuable insights into quantifying and mitigating the potential risks and uncertainties associated with Eely's missions. By identifying critical factors such as the robustness of the autonomous control, thruster module actuators, propulsion system, and altitude control system, the areas where improvements could significantly reduce the risk of losing Eely during different operations, including seabed mapping and confined space operations were highlighted.

Furthermore, the simulation results revealed that the FOPID altitude controller exhibited superior altitude regulation performance in confined environments, demonstrating Eely's ability to navigate challenging terrains with enhanced precision and stability. The FOPID controller proved to be resilient to disturbances and uncertainties, making it a promising option for controlling underwater snake robots when overshoot and settling time are crucial considerations.

However, it is important to note that field experiments presented some disparities compared to the simulated results. The real-world conditions introduced sensor noise, harsh environmental challenges, and restrictions on low-level controller intervention, which affected Eely's altitude performance. Additionally, factors such as the duration of field experiments, current loads, and tether management, which were not considered in the simulator, played significant roles in the robot's performance.

7.2 Further Work

The work developed in the thesis opens avenues for future research and development in the field of underwater snake robots operating in confined environments. Here are some potential areas for further investigation:

1. Enhanced Risk Assessment: Expand the Bayesian risk assessment methodology to encompass additional risk factors and uncertainties. Incorporate real-time sensor data and environmental feedback to continuously update risk models and adapt control strategies accordingly.

2. Adaptive Control Strategies: Investigate adaptive control algorithms that can dynamically adjust Eely's control parameters based on the changing environmental conditions and uncertainties encountered during missions. Develop intelligent control systems that can optimize performance and mitigate risks in real-time.

3. Hybrid Control Approaches: Explore the integration of machine learning techniques and traditional control methods to enhance the performance and adaptability of Eely in confined environments. Develop models that can learn from past mission experiences to make informed decisions and improve control strategies.

4. Experimental Validation: Conduct extensive field experiments to validate the simulator's accuracy and further compare the simulated altitude capabilities with Eely's real-world performance. Consider factors such as sensor noise, harsh environmental conditions, tether management, and intervention in the low-level controller to provide a more comprehensive evaluation.

5. Collaborative Robotic Systems: Investigate the potential for collaborative behavior among underwater snake robots and an unmanned surface vehicles to enhance exploration and intervention capabilities in confined environments. Explore coordination, communication, and task allocation strategies to enable efficient and safe operations in complex underwater landscapes.

6. Active Tether Self-management System: Integrating the fiber optic cable between Eely and an unmanned surface vehicles as an embedded winch system to assist in maintaining the cable in a semi-stretched configuration, thereby preventing entanglement with obstacles [70].

By addressing these research areas, we can further advance the field of underwater snake robots and contribute to their successful exploration and intervention in confined environments, ensuring safer and more reliable operations in challenging underwater landscapes.

References

[1] Junku Yuh. "Design and control of autonomous underwater robots: A survey". In: *Autonomous Robots* 8.1 (2000), pp. 7–24.

[2] Huu-Tho Dang. "Underwater robots for karst and marine exploration : A study of redundant AUVs". PhD dissertation. Université de Montpellier, 2021.

[3] WC Stone. "Design and deployment of a 3D autonomous subterranean submarine exploration vehicle". In: *Proceedings UUST07, Conference on Un-manned, Untethered Submersable Technology, Durham, NH*. 2007.

[4] Nathaniel Fairfield, George Kantor, and David Wettergreen. "Real-time SLAM with octree evidence grids for exploration in underwater tunnels". In: *Journal of Field Robotics* 24.1-2 (2007), pp. 03–21.

[5] Luis Lopes, Norbert Zajzon, Balázs Bodo, Stephen Henley, Gorazd Žibret, and Tatjana Dizdarevic. "UNEXMIN: Developing an autonomous underwater explorer for flooded mines". In: *Energy Procedia* 125 (2017), pp. 41–49.

[6] Adrien Lasbouygues, Silvain Louis, Benoıt Ropars, Luc Rossi, Herve Jourde, Hélène Délas, Pierre Balordi, Rémi Bouchard, Mehdi Dighouth, Marc Dugrenot, et al. "Robotic mapping of a karst aquifer". In: *IFAC: International Federation of Automatic Control*. 2017.

[7] Pål Liljebäck and Richard Mills. "Eelume: A flexible and subsea resident IMR vehicle". In: *Oceans 2017-Aberdeen*. IEEE. 2017, pp. 1–4.

[8] SNAME. "Nomenclature for Treating the Motion of a Submerged Body Through a Fluid". In: *Technical Research Bulletin No.* (1950), pp. 1–5.

[9] Eleni Kelasidi. "Modeling, Control and Energy Efficiency of Underwater Snake Robots". PhD dissertation. Norwegian University of Science and Technology, 2015.

[10] Eleni Kelasidi, K. Y. Pettersen, J. T. Gravdahl, and P. Liljebäck. "Modeling of underwater snake robots". In: *2014 IEEE International Conference on Robotics and Automation (ICRA)*. 2014, pp. 4540–4547. DOI: `10.1109/ICRA.2014.6907522`.

[11] Henrik M. Schmidt-Didlaukies, Asgeir J. Sørensen, and Kristin Y. Pettersen. "Modeling of Articulated Underwater Robots for Simulation and Control". In: *2018 IEEE/OES Autonomous Underwater Vehicle Workshop (AUV)*. 2018, pp. 1–7. DOI: `10.1109/AUV.2018.8729806`.

[12] Roy Featherstone. *Rigid Body Dynamics Algorithms*. Springer, 2014.

[13] Fredrik Dukan. "ROV Motion Control Systems". PhD dissertation. Norwegian University of Science and Technology, 2014.

[14] Aksel Alstad Mogstad. "Underwater Hyperspectral Imaging as a Tool for Benthic Habitat Mapping". PhD dissertation. Norwegian University of Science and Technology, 2021.

[15] Jørgen Tegdan, Stefan Ekehaug, Ingrid Myrnes Hansen, Lars Martin Sandvik Aas, Kay Johnny Steen, Ragnhild Pettersen, Frank Beuchel, and Lionel Camus. "Underwater hyperspectral imaging for environmental mapping and monitoring of seabed habitats". In: *OCEANS 2015 - Genova*. 2015, pp. 1–6. DOI: `10.1109/OCEANS-Genova.2015.7271703`.

[16] ProPhotonix. *LED vs Halogen Technology for Hyperspectral Imaging*. URL: `https://www.prophotonix.com/blog/led-vs-halogen-technology-for-hyperspectral-imaging/`.

[17] Geir Johnsen, Z. Volent, H. Dierssen, R. Pettersen, M.Van Ardelan, F. Søreide, P. Fearns, M. Ludvigsen, and M. Moline. "20 - Underwater hyperspectral imagery to create biogeochemical maps of seafloor properties". In: *Subsea Optics and Imaging*. Ed. by John Watson and Oliver Zielinski. Woodhead Publishing Series in Electronic and Optical Materials. Woodhead Publishing, 2013, 508–540e. ISBN: 978-0-85709-341-7. DOI: `https://doi.org/10.1533/9780857093523.3.508`. URL: `https://www.sciencedirect.com/science/article/pii/B9780857093417500200`.

[18] ecotone. *Software and hardware for Underwater Hyperspectral Imaging*. URL: `https://ecotone.com`.

[19] David.R. Lyzenga, Norman.P. Malinas, and Fred.J. Tanis. "Multispectral bathymetry using a simple physically based algorithm". In: *IEEE Transactions on Geoscience and Remote Sensing* 44.8 (2006), pp. 2251–2259. DOI: `10.1109/TGRS.2006.872909`.

[20] Thomas Erling Lone. "NAVIGATION TECHNIQUES FOR UNDERWATER VEHICLES IN POLAR REGIONS". MSc dissertation. Norwegian University of Science and Technology, 2020.

[21] Asgeir J. Sørensen, Martin Ludvigsen, Petter Norgren, Øyvind Ødegård, and Finlo Cottier. "Sensor-Carrying Platforms". In: *POLAR NIGHT Marine Ecology: Life and Light in the Dead of Night*. Ed. by Jørgen Berge, Geir Johnsen, and Jonathan H. Cohen. Cham: Springer International Publishing, 2020, pp. 241–275. ISBN: 978-3-030-33208-2. DOI: `10.1007/978-3-030-33208-2_9`. URL: `https://doi.org/10.1007/978-3-030-33208-2_9`.

[22] Emiliano Cimoli, Arko Lucieer, Klaus M. Meiners, Lars Chresten Lund-Hansen, Fraser Kennedy, Andrew Martin, Andrew McMinn, and Vanessa Lucieer. "Towards improved estimates of sea-ice algal biomass: experimental assessment of hyperspectral imaging cameras for under-ice studies". In: *Annals of Glaciology* 58.75pt1 (2017), pp. 68–77. DOI: `10.1017/aog.2017.6`.

[23] ISO. *ISO 31000: Risk Management: Principles and Guidelines*. 2009.

[24] NORSOK-Z-013. *Risk and emergency preparedness assessment*. 2010.

[25] Marvin Rausand. *Risk assessment: theory, methods, and applications*. Vol. 115. John Wiley & Sons, 2013.

[26] Terje Aven. "Practical implications of the new risk perspectives". In: *Reliability Engineering & System Safety* 115 (2013), pp. 136–145. ISSN: 0951-8320. DOI: `https://doi.org/10.1016/j.ress.2013.02.020`.

[27]   Christoph Thieme. "Development of a Risk Management Process for NTNU's RE-MUS 100 AUV". MSc dissertation. Norwegian University of Science and Technology, 2014.

[28]   Jeevith Hegde, Ingrid Bouwer Utne, Ingrid Schjølberg, and Brede Thorkildsen. "A Bayesian approach to risk modeling of autonomous subsea intervention operations". In: *Reliability Engineering & System Safety* 175 (2018), pp. 142–159. ISSN: 0951-8320. DOI: https://doi.org/10.1016/j.ress.2018.03.019.

[29]   Christoph Alexander Thieme and Ingrid Bouwer Utne. "A risk model for autonomous marine systems and operation focusing on human–autonomy collaboration". In: *Proceedings of the Institution of Mechanical Engineers, Part O: Journal of Risk and Reliability* 231 (2017), pp. 446–464. DOI: 10.1177/1748006X17709377.

[30]   Max Krüger, Jürgen Ziegler, and Kathrin Heller. "A generic Bayesian Network for identification and assessment of objects in maritime surveillance". In: *2012 15th International Conference on Information Fusion*. 2012, pp. 2309–2316.

[31]   Hongfei Yao, Hongjian Wang, Yiming Li, Ying Wang, and Chunsong Han. "Research on Unmanned Underwater Vehicle Threat Assessment". In: *IEEE Access* 7 (2019), pp. 11387–11396. DOI: 10.1109/ACCESS.2019.2891940.

[32]   Jens E Bremnes, Christoph A Thieme, Asgeir J Sørensen, Ingrid B Utne, and Petter Norgren. "A Bayesian Approach to Supervisory Risk Control of AUVs Applied to Under-Ice Operations". In: *Marine Technology Society Journal* 54.4 (2020), pp. 16–39.

[33]   Ingrid Bouwer Utne and Ingrid Schjølberg. "A Systematic Approach to Risk Assessment: Focusing on Autonomous Underwater Vehicles and Operations in Arctic Areas". In: vol. Volume 10: Polar and Arctic Science and Technology. International Conference on Offshore Mechanics and Arctic Engineering. 2014. DOI: 10.1115/OMAE2014-23776.

[34]   Bendik Alexander Urne Jørgensen. "Methods for Visual Inspection and Mapping of Subsea Structures and Rough and Steep Underwater Terrain Using Articulated Underwater Robots". MSc dissertation. Norwegian University of Science and Technology, 2022.

[35]   Benoit Ropars, Adrien Lasbouygues, Lionel Lapierre, and David Andreu. "Thruster's dead-zones compensation for the actuation system of an underwater vehicle". In: *2015 European Control Conference (ECC)*. IEEE. 2015, pp. 741–746.

[36]   Adrien Lasbouygues, Lionel Lapierre, David Andreu, Josue Lopez Hermoso, Hervé Jourde, and Benoit Ropars. "Stable and reactive centering in conduits for karstic exploration". In: *2014 European Control Conference (ECC)*. IEEE. 2014, pp. 2986–2991.

[37]   Gwyn Griffiths and Mario Brito. "Predicting risk in missions under sea ice with Autonomous Underwater Vehicles". In: *2008 IEEE/OES Autonomous Underwater Vehicles*. 2008, pp. 1–7. DOI: 10.1109/AUV.2008.5290536.

[38]   Marvin Rausand. *Risk assessment: theory, methods, and applications*. Vol. 115. John Wiley & Sons, 2013.

[39]   Jørgen Tegdan, Stefan Ekehaug, Ingrid Myrnes Hansen, Lars Martin Sandvik Aas, Kay Johnny Steen, Ragnhild Pettersen, Frank Beuchel, and Lionel Camus. "Underwater hyperspectral imaging for environmental mapping and monitoring of seabed habitats". In: *OCEANS 2015 - Genova*. 2015, pp. 1–6. DOI: `10.1109/OCEANS-Genova.2015.7271703`.

[40]   BayesFusion, LLC. *GeNIe: A Tool for Graphical Decision-Analytic Modeling*. `https://support.bayesfusion.com/docs`.

[41]   Fredrik Dukan and Asgeir J. Sørensen. "Altitude Estimation and Control of ROV by use of DVL". In: *IFAC Proceedings Volumes* 45.27 (2012). 9th IFAC Conference on Manoeuvring and Control of Marine Craft, pp. 79–84. ISSN: 1474-6670. DOI: `https://doi.org/10.3182/20120919-3-IT-2046.00014`. URL: `https://www.sciencedirect.com/science/article/pii/S1474667016312083`.

[42]   Fredrik Dukan and Asgeir J. Sørensen. "Sea floor geometry approximation and altitude control of ROVs". In: *Control Engineering Practice* 29 (2014), pp. 135–146. ISSN: 0967-0661. DOI: `https://doi.org/10.1016/j.conengprac.2014.04.006`. URL: `https://www.sciencedirect.com/science/article/pii/S0967066114001312`.

[43]   Xiaoming Nie, Jian Zhou, and Xingwu Long. "Velocity correction of the Janus configuration laser Doppler velocimeter". In: *Measurement* 46.2 (2013), pp. 938–941. ISSN: 0263-2241. DOI: `https://doi.org/10.1016/j.measurement.2012.10.029`. URL: `https://www.sciencedirect.com/science/article/pii/S0263224112004010`.

[44]   Kristin Y. Pettersen. "Snake robots". In: *Annual Reviews in Control* 44 (2017), pp. 19–44. ISSN: 1367-5788. DOI: `https://doi.org/10.1016/j.arcontrol.2017.09.006`. URL: `https://www.sciencedirect.com/science/article/pii/S1367578817301050`.

[45]   Jørgen Sverdrup-Thygeson, Eleni Kelasidi, Kristin Y. Pettersen, and Jan Tommy Gravdahl. "The Underwater Swimming Manipulator—A Bioinspired Solution for Subsea Operations". In: *IEEE Journal of Oceanic Engineering* 43.2 (2018), pp. 402–417. DOI: `10.1109/JOE.2017.2768108`.

[46]   Aws Abdulsalam Najm and Ibraheem Kasim Ibraheem. "Nonlinear PID controller design for a 6-DOF UAV quadrotor system". In: *Engineering Science and Technology, an International Journal* 22.4 (2019), pp. 1087–1097. ISSN: 2215-0986. DOI: `https://doi.org/10.1016/j.jestch.2019.02.005`. URL: `https://www.sciencedirect.com/science/article/pii/S2215098618318846`.

[47]   Igor Podlubny. "Fractional-order systems and fractional-order controllers". In: *Institute of Experimental Physics, Slovak Academy of Sciences, Kosice* 12.3 (1994), pp. 1–18.

[48]   Igor Podlubny, Lubomir Dorcak, and Imrich Kostial. "On fractional derivatives, fractional-order dynamic systems and PI/sup/spl lambda//D/sup/spl mu//-controllers". In: *Proceedings of the 36th IEEE Conference on Decision and Control*. Vol. 5. IEEE. 1997, pp. 4985–4990.

[49]   JA Tenreiro Machado. "Analysis and design of fractional-order digital control systems". In: *Systems Analysis Modelling Simulation* 27.2-3 (1997), pp. 107–122.

[50]   Tatiana Odzijewicz, Agnieszka B Malinowska, and Delfim FM Torres. "Fractional variational calculus with classical and combined Caputo derivatives". In: *Nonlinear Analysis: Theory, Methods & Applications* 75.3 (2012), pp. 1507–1515.

[51]   Tatiana Odzijewicz, Agnieszka B Malinowska, and Delfim FM Torres. "Fractional variational calculus of variable order". In: *Advances in Harmonic Analysis and Operator Theory: The Stefan Samko Anniversary Volume.* Springer. 2013, pp. 291–301.

[52]   Małgorzata Klimek and Maria Lupa. "Reflection symmetric formulation of generalized fractional variational calculus". In: *Fractional Calculus and Applied Analysis* 16 (2013), pp. 243–261.

[53]   Jitendra Kumar, Ahmad Taher Azar, Vineet Kumar, and Kamal Pal Singh Rana. "Design of fractional order fuzzy sliding mode controller for nonlinear complex systems". In: *Mathematical Techniques of Fractional Order Systems.* Elsevier, 2018, pp. 249–282.

[54]   D. B. Talange, S. D. Joshi, and Santosh Gaikwad. "Control of autonomous underwater vehicle using fractional order PI controller". In: *2013 IEEE International Conference on Control Applications (CCA).* 2013, pp. 1111–1116. DOI: 10.1109/CCA.2013.6662900.

[55]   Billel Meghni, Djalel Dib, Ahmad Taher Azar, and Abdallah Saadoun. "Effective supervisory controller to extend optimal energy management in hybrid wind turbine under energy and reliability constraints". In: *International Journal of Dynamics and Control* 6 (2018), pp. 369–383.

[56]   Hossam Hassan Ammar and Ahmad Taher Azar. "Robust path tracking of mobile robot using fractional order PID controller". In: *The International Conference on Advanced Machine Learning Technologies and Applications (AMLTA2019) 4.* Springer. 2020, pp. 370–381.

[57]   Øystein Sture, Martin Ludvigsen, Fredrik Sreide, and Lars Martin Sandvik Aas. "Autonomous underwater vehicles as a platform for underwater hyperspectral imaging". In: *OCEANS 2017 - Aberdeen.* 2017, pp. 1–8. DOI: 10.1109/OCEANSE.2017.8084995.

[58]   I. Podlubny. "Fractional-order systems and PI/sup /spl lambda//D/sup /spl mu//-controllers". In: *IEEE Transactions on Automatic Control* 44.1 (1999), pp. 208–214. DOI: 10.1109/9.739144.

[59]   Rasheed Abdulkader. "Non-integer Controller for Autonomous Underwater Vehicle Steering Control". In: *2021 IEEE International Conference on Robotics, Automation, Artificial-Intelligence and Internet-of-Things (RAAICON).* 2021, pp. 102–105. DOI: 10.1109/RAAICON54709.2021.9929838.

[60]   Jun-Yi Cao and Bing-Gang Cao. "Design of fractional order controllers based on particle swarm optimization". In: *2006 1st IEEE conference on industrial electronics and applications.* IEEE. 2006, pp. 1–6.

[61]   Steven Macenski, Tully Foote, Brian Gerkey, Chris Lalancette, and William Woodall. "Robot Operating System 2: Design, architecture, and uses in the wild". In: *Science Robotics* 7.66 (2022), eabm6074. DOI: 10.1126/scirobotics.abm6074. eprint: https://www.science.org/doi/pdf/10.1126/scirobotics.abm6074. URL: https://www.science.org/doi/abs/10.1126/scirobotics.abm6074.

[62] Francisco Martın Rico. *A Concise Introduction to Robot Programming with ROS2*. CRC Press, 2022.

[63] Liquid.ai. *Plankton*. URL: https://github.com/Liquid-ai/Plankton.

[64] UUV Simulator - Unmanned Underwater Vehicle Simulator. *uuv_simulator*. URL: https://github.com/uuvsimulator/uuv_simulator.

[65] Roy Featherstone. *Rigid Body Dynamics Algorithms*. Vol. vol. 49. Jan. 2007. ISBN: 978-1-4757-6437-6. DOI: 10.1007/978-0-387-74315-8.

[66] Asgeir J Sørensen. "Marine cybernetics, towards autonomous marine operations and systems". In: *Department of Marine Technology, NTNU* (2018).

[67] RE Toohey, W Brown, and JH Stebbings. "Systematic geographic sampling with UTM coordinates". In: *Environment International* 14.3 (1988), pp. 207–212.

[68] Chris Whitty and Mark Walport. "Satellite-derived Time and Position: A Study of Critical Dependencies". In: *Government Office for Science: London, UK* (2018).

[69] EIVA. *EIVA - Maritime survey and construction solutions*. URL: https://www.eiva.com.

[70] Ornella Tortorici, Cédric Anthierens, Vincent Hugel, and Herve Barthelemy. "Towards active self-management of umbilical linking ROV and USV for safer submarine missions". In: *IFAC-PapersOnLine* 52.21 (2019), pp. 265–270.

Appendices

Two papers that were written as part of the work on this master's thesis are appended below.

Paper 1

Risk Assessment of an Autonomous Underwater Snake Robot in Confined Operations

Abdelrahman Sayed Sayed

Risk Assessment of an Autonomous Underwater Snake Robot in Confined Operations

Abdelrahman Sayed Sayed

Abstract—The growing interest in ocean discovery imposes a need for inspection and intervention in confined and demanding environments. Eely's slender shape, in addition to its ability to change its body configurations, makes articulated underwater robots an adequate option for such environments. However, operation of Eely in such environments imposes demanding requirements on the system, as it must deal with uncertain and unstructured environments, extreme environmental conditions, and reduced navigational capabilities. This paper proposes a Bayesian approach to assess the risks of losing Eely during two mission scenarios. The goal of this work is to improve Eely's performance and the likelihood of mission success. Sensitivity analysis results are presented in order to demonstrate the causes having the highest impact on losing Eely.

Index Terms—Autonomous underwater vehicles, Bayesian Belief Network, Decision Network, Dynamic Bayesian Network, Eely, Risk Assessment

I. INTRODUCTION

The growing interest in ocean discovery imposes a need for inspection and intervention in confined and demanding environments. Underwater confined environments, such as shipwrecks and sunken caves, present unique challenges for exploration. These environments often have limited access points and tight spaces, making it difficult for divers and underwater vehicles to enter and maneuver [1]. Autonomous underwater vehicles (AUVs) are considered to be efficient sensor-carrying platforms for seabed mapping and monitoring [2]. The likelihood of the underwater vehicles being lost while performing these missions can under certain circumstances be high, and some AUVs have been lost during missions due to technical failures [3].

Underwater snake robots, like Eely which is a snake robot from Eelume [4], [5] is a promising option for these environments due to their slender shape and ability to change body configurations. Eely's articulated structure shown in Figure 1 combines the advantages of several types of underwater vehicles, as it has the range of AUVs, the ability to access challenging areas like small Remotely operated underwater vehicles (ROVs), and the intervention capabilities of ROVs [6]. Thereby, Eely covers a broad range of operational scenarios as the vehicle can be configured to follow a torpedo-shaped AUV for platforming missions requiring the robot to map a big area [7] or to vary the joint's modules to follow snake

Abdelrahman Sayed Sayed is with Department of Marine Technology, Norwegian University of Science and Technology (NTNU), Otto Nielsens veg 10, 7491 Trondheim, Norway; Université de Toulon, Toulon, France. `abdelrahman.s.s.e.ibrahim@ntnu.no`, `abdelrahman-ibrahim@etud.univ-tln.fr`

configuration to map confined or steep environments which can not be achieved by a normal AUV. However, operation of Eely in such environments imposes demanding requirements on the system, as it must deal with uncertain and unstructured environments, extreme environmental conditions, and reduced navigational capabilities [8].
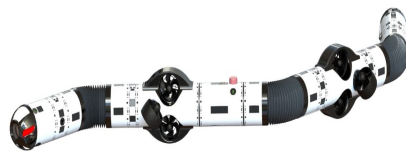

Figure 1. Triple joint snake robot from Eelume

Bayesian networks (BNs) have been widely used to assess the risks associated with Autonomous Underwater Vehicles (AUVs) in operational scenarios, as demonstrated in previous studies [9]–[12]. However, there has been no prior work that has specifically addressed the risks associated with modular underwater snake robots operating in confined environments.

The main scientific contribution in this paper, we present a novel approach to risk assessment for Eely, an underwater snake robot, in confined environments operations. Our aim is to improve Eely's performance and increase the likelihood of mission success. Relevant data are collected to perform a quantitative risk analysis to develop a Bayesian model that considers almost the entire system of Eely, thus avoiding potential risks. We demonstrate that our Bayesian model can be extended to a Decision network (DN), enabling Eely to adapt its behavior autonomously and maximize mission utility [13]. Although our model was developed specifically for Eely, it can be transferred to the operations of other AUVs. To the best of our knowledge, the topic of risk associated with modular underwater snake robots has not been previously explored in existing research. Therefore, our study presents a state of the art contribution to the field of risk assessment of underwater vehicles.

The paper is organized as follows: Section II presents the background on risk and Bayesian networks. In Section III, the application of the proposed BN risk model for the two case scenarios, including data collection for parameters for these models, dynamic simulation, and sensitivity analysis to identify the causes with the most significant influence on losing Eely. In Section IV the steps to extend the BN to a DN for autonomous risk-based decision making are presented. This is followed by Section V, which gives a brief discussion of the results. Finally, Section VI concludes this paper and presents suggestions for future work.

II. RISK MODELING USING BNs

A. Definition of Risk

The definition of risk related to a hazardous event e_i [14] can be represented by the following relation:

$$r = \{e_i, c_i, q\}|k \tag{1}$$

where c_i is the consequence of e_i, q is the measure of involved uncertainty, and k is the background knowledge for determining e_i, c_i and q. This is the most commonly used definition for Bayesian risk modeling. By accounting for previous knowledge about the operational conditions and mission scenarios, events with low background knowledge would not have a strong effect when making a decision in contrast to events with high background knowledge. According to [15], risk assessment is an overall process including risk identification, risk analysis, and risk evaluation. Risk identification identifies and illustrates the possible risks with respect to the mission objective. A common approach for risk identification is to identify the known hazards as a source[s] of prospective harm. These hazards can be later analyzed in the risk analysis step, where the known possible events and their expected outcomes are modeled. Therefore, risk identification is an essential step towards developing a control system with risk management and decision-making capabilities for Eely which is known as supervisory risk control [16]. There are many of risk identification methods, such as hazard identification (HAZID) and preliminary hazard analysis (PHA). In order to have effective supervisory risk control, the most significant mission and operation hazards should be identified and combined into a risk model to aid in the system's decision-making.

B. Bayesian Networks

A Bayesian network is a graphical model used to address problems involving uncertainty [11], [12]. It describes the dependencies between random variables in a directed acyclic graph, where nodes stand for random variables and directed arcs between nodes signify conditional dependencies between them. The Bayesian network, which is based on probability theory [17], allows for two-way reasoning by handling both causal reasoning, which derives posterior probabilities from prior probabilities, and diagnostic reasoning, which uses a

formula to derive prior probabilities from posterior probabilities. The traditional static Bayesian network (SBN) has limitations when it comes to evaluating variables that change over time, but it is useful for analyzing and forecasting data at a specific time. The dynamic Bayesian network was created to overcome this drawback. The dynamic Bayesian network (DBN) incorporates methods that take into account the relationship between moments in time, known as the state transition probability, in contrast to SBN [18]. By considering this relationship, the network can learn to effectively use changes in values over time, producing better results.

III. CONSTRUCTION OF BAYESIAN RISK MODEL

In the context of risk assessment, Definition (1) may imply a Bayesian approach to probabilities, and hence the use of BN is a suitable approach to estimate the probability of losing Eely during different operational scenarios. HAZID was performed for the two case scenarios: i. Seabed mapping and ii. Confined environments operations in the form of a preliminary hazard analysis (PHA) prior to the development of the Bayesian risk model. Using the five-step method described in [13], the Bayesian risk model is developed.

A. HAZID

HAZID aims to identify the hazards related to the operation of Eely for the two proposed case scenarios. Detectability is defined as Eely's ability to detect and monitor a specific hazard during its operation, where a high degree of detectability suggests a strong background knowledge, while a low degree of detectability suggests a weak background knowledge. The collection of hazards was mainly based on [19] as it offered a comprehensive compilation of potential risks and served as the foundation for the identification procedure, along with our own judgment and similar systems [13]. In addition to, previous field trials with Eely in Trondheim Fjord [20] and previous experiments in karstic exploration [21]–[23] were also taken into account.

Table I, adopted from [13] which was used for hazards in the context of AUV operation under ice, the same criteria was selected and modified based on hazards related to Eely's operation. Then, these hazards were assigned possible consequences depending on each case scenario, and the most noticeable hazards were identified. The risk priority number (rpn) for each hazard is obtained from the categories shown in Table I. The rpn is the product of the frequency rating, the consequence rating, and the detectability rating. To assess the risk, the worst-case scenario is assumed which is losing Eely. Note that this loss may be temporary, as in the case of seabed mapping and deploying a vessel may recover Eely [10], or it can be a permanent loss as in the case of underwater caves. Tables VII - VIII in the Appendix lists the hazards identified for the two case scenarios presented in the study. The assessment sheets design in the tables is based on the PHA sheet from [24].

Rating	Score	Description
Frequency		
Low	1	The event may occur less than once per mission
Medium	2	The event will be encountered, on average, once per mission
High	3	The event will be encountered several times per mission
Consequences		
Low/None	1	The event will have no negligible influence on the mission with respect to damage to Eely or loss of mission data
Medium	2	The event may lead to damages or delays that will minorly reduce the time available for the mission or affect the data collection
High	3	The event may lead to loss of Eely, early abortion of the mission, or significant loss of scientific data
Detectability		
Low/None	3	Eely is not able to detect or assess the hazardous event during the operation
Medium	2	Eely may infer information about the hazardous event. However, the inference will be associated with high uncertainty
High	1	Eely may collect and infer information about the hazardous event with high certainty

B. Failure Probabilities

Some of the issues related to conducting a quantitative risk assessment are obtaining the failure data of the sensors and components of the robot. Since Eely robot is in the early stages of experiments, the availability of its failure data is scarce. Different data sources were used, which include literature and technical specifications, etc. For the non-available data, assumptions based on overall knowledge were applied, which provides rough estimates for the scenarios.

The failure probabilities per year are given in Table II, which are used in the BN nodes. However, it should be noted that failure probabilities for some parts of the robot's sensors were taken as for the general parts and not for a product of a specific brand from a specific company. For example, the failure probability for the Underwater hyperspectral imager (UHI) sensor was taken as the same value for the general camera as the UHI is simply a more advanced camera as it combines a push-broom hyperspectral imager with an external light source [25]. The obtained data which is available is used as an initial attempt for quantitative risk assessment, but more proper assumptions and precise data could be extracted in future trials and for system suppress analysing own design.

C. Conditional Probability Tables

The conditional probability tables (CPT) III-VI are quantified based on the PHA. Table III shows the CPT for the failure of the propulsion system node. This table shows how

Table II
FAILURE PROBABILITIES

Sensor/Item	Failure Probability	Source
Joint module actuators	0.125	[1]
Thruster module actuators	0.1	[26]
DVL sensor	0.1	[27]
IMU sensor	0.01	[28]
UHI sensor	0.01	[29]
Cameras	0.01	[29]
LED lights	0.02	[30]
Leakage sensor	0.05	[31]
Batteries	0.000001	[32]

critical is it in case of the failure of thruster module actuators as shown in red in any case of failure of thruster module actuators the probability of losing Eely is true as in confined environments the robot can't use its neutral buoyancy to float back to the surface. This is further illustrated in the sensitivity analysis subsection. Due to the limit on the number of pages, the CPTs for other nodes are omitted from this version of the paper. Moreover, thrusters were one of the most susceptible components to failure as Eely operators at the Applied Underwater Robotics Laboratory (AUR Lab) have communicated that they have lost on average one thruster per year.

Table III
CPT FOR FAILURE OF PROPULSION SYSTEM

Failure of thruster module actuators	TRUE				FALSE			
Failure of joint module actuators	TRUE		FALSE		TRUE		FALSE	
Environmental complexity	T	F	T	F	T	F	T	F
TRUE	1	1	1	1	0.3	0.1	0.35	0
FALSE	0	0	0	0	0.7	0.9	0.65	1

Table IV
CPT FOR ENVIRONMENTAL COMPLEXITY

Ocean current	TRUE				FALSE			
Dusty sediments	TRUE		FALSE		TRUE		FALSE	
Absence of natural light	T	F	T	F	T	F	T	F
TRUE	0.95	0.9	0.6	0.4	0.7	0.6	0.15	0.01
FALSE	0.05	0.1	0.4	0.6	0.3	0.4	0.85	0.99

D. Launching the BN Model

After gathering the failure probabilities data, the BN model is constructed using the software GeNIe 4.0, which allows

Table V
CPT FOR REMOTE CONTROL

Failure of communication system	TRUE				FALSE			
Failure of operator intervention	TRUE		FALSE		TRUE		FALSE	
Environmental complexity	T	F	T	F	T	F	T	F
TRUE	0.4	0.3	0.3	0.2	0.1	0.01	0.05	0.01
FALSE	0.6	0.7	0.7	0.8	0.9	0.99	0.95	0.99

Table VI
CPT FOR LOSS OF EELY

Failure of autonomous control	TRUE		FALSE	
Failure of remote control	TRUE	FALSE	TRUE	FALSE
TRUE	1	0.75	0.1	0
FALSE	0	0.25	0.9	1

interactive model building and learning, developed by Bayes Fusion company [33].

E. Dynamic Simulation

Figure 2 shows one of the developed DBNs for the case of confined environments operations. The simulation results of the DBNs for the two case scenarios can be observed in Figures 3 - 4. The results indicate that the DBN can take into account changes over time and the likelihood of events occurring. In this regard, the probability of losing Eely in confined environments is higher than in seabed mapping due to various factors such as extreme pressures on the thrusters, poor communication with the vehicle, high mission complexity, and the complexity of the environment.

F. Sensitivity Analysis

The goal of sensitivity analysis is to identify the causes that have the most significant impact on the probability of losing Eely, and to limit these causes by introducing risk reduction measures. It also works as an indicator for adding more constraints and efforts for data collection. Decreasing the uncertainty of a cause that has little or no influence on the probability of losing Eely will result in a negligible change in the overall uncertainty value, making it of little importance. In our case, we aim to identify the top factors that influence the probability of losing Eely. Figures 5 - 6 show the sensitivity analysis results for losing Eely for the two case scenarios.

In the first case of seabed mapping operations shown in Figure 5, it can be seen that the probability of losing Eely is most sensitive to the failure of autonomous control. Other main factors are comprised of failure of thruster module, failure of altitude control, mission complexity, and DVL failure. The

second case of sensitivity analysis is performed for confined environment operations and is shown in Figure 6. It can be seen that the failure of autonomous control is the most sensitive factor for losing Eely as well. Environmental complexity, failure of propulsion system, failure of altitude control, and mission complexity account for the remaining factors to which the loss of Eely is sensitive.

G. Pros and Cons of the BN Model

The model looks upon almost Eely's entire system to avoid potential risks. Despite the fact that the model was built specifically for Eely, it can be transferred to the operations of other autonomous underwater vehicles. On the other hand, the model has some limitations, such as not including all of the possibilities with details which can cause the loss of Eely and not completely extending some nodes. For instance, nodes such as failure of communication system and failure of operator intervention, the latter being a non-technical node, could be further developed, and other non-trivial factors could have been included in the model. For such expansion, it would require searching for more data including human and organizational factors and their influence on mission risk, which would take a significant amount of time and resources, having the current model seem to be adequate for the two investigated case scenarios. Moreover, DBN is time dependent where the state of a variable at one time depends on its previous states and the states of other variables and it can be computationally expensive to compute more time steps, and GeNIe is only limited to 1000 time step [33].

IV. RISK-BASED DECISION MAKING

Bayesian probability theory is used by both DNs and DBNs to represent uncertain relationships between variables. The main difference is that DNs do not take into account time dependence and provide a snapshot of the system at a specific moment. DNs are employed to simulate the relationship between choices and results when making decisions. In contrast, DBNs can also include decision-making only as part of a dynamic system that changes over time.

For decision-making, the novel approach presented in [13] can be followed, in which the HAZID results of Eely's operations can be used as a basis for constructing the BN model. The BN model can then be extended to a DN to autonomously adapt Eely's behavior with decision nodes, i.e., by adjusting the altitude set point, speed set point, and control strategy [7]. In our case, the maximum joint angle for dynamically changing the robot's shape can be adjusted based on its belief about the current state of the risk.

A. Decision Nodes

The decision nodes that should be directly controlled by Eely are: altitude/depth set point, speed set point, the control strategy. In the articulated snake robot case, we can add one more node, "changing shape" based on mission category and
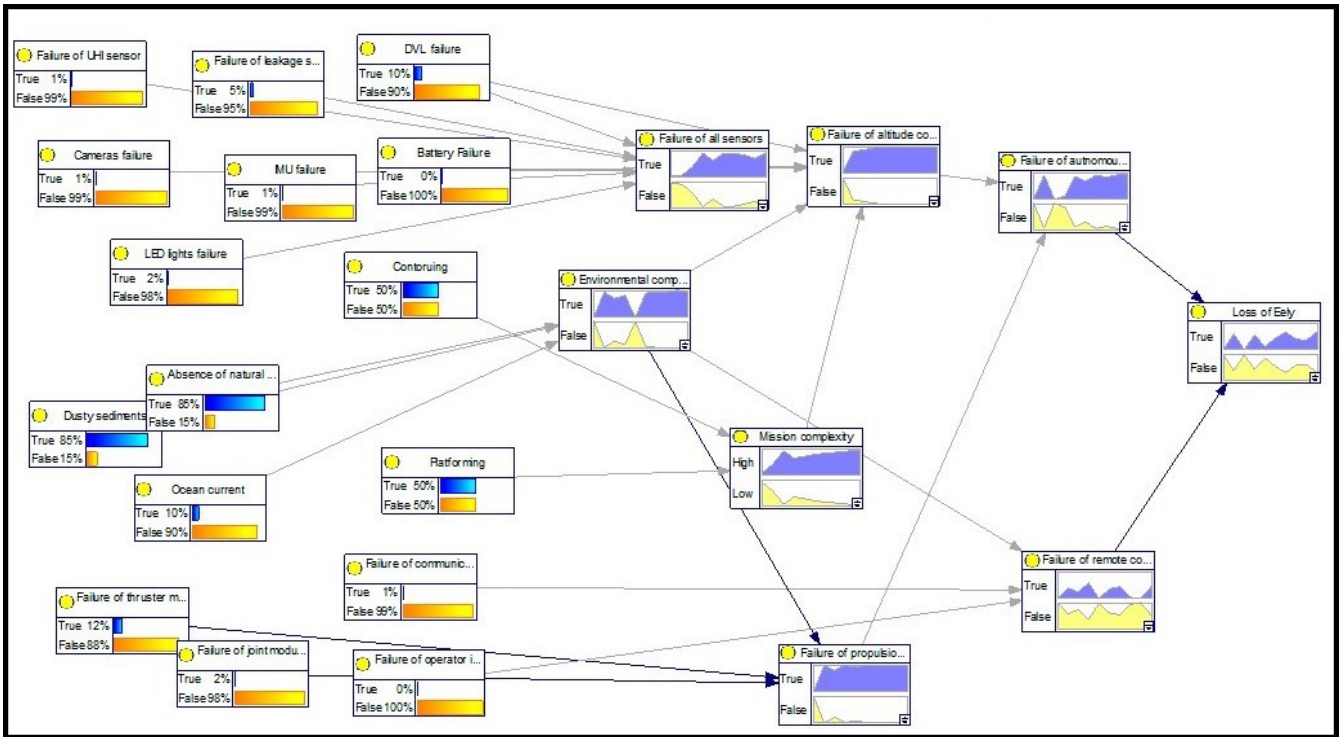
Figure 2. DBN for Losing Eely during Confined Environments Operations

(a) Environmental Complexity

(b) Mission Complexity

(c) Failure of Propulsion System

(d) Failure of Remote Control

(e) Loss of Eely

Figure 3. Dynamic Simulation Results for Seabed Mapping Operations

(a) Environmental Complexity

(b) Mission Complexity

(c) Failure of Propulsion System

(d) Failure of Remote Control

(e) Loss of Eely

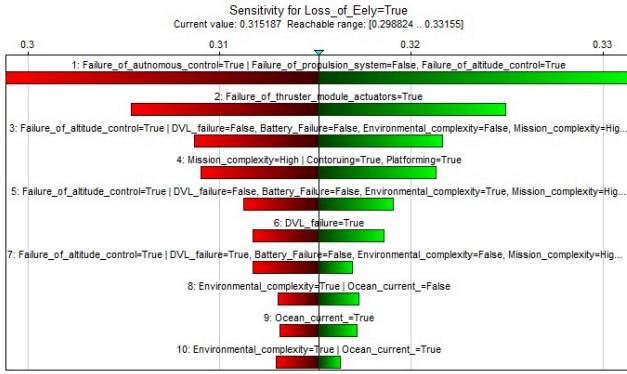Figure 4. Dynamic Simulation Results for Confined Environments Operations

Figure 5. Sensitivity tornado diagram for losing Eely during Seabed Mapping Operations
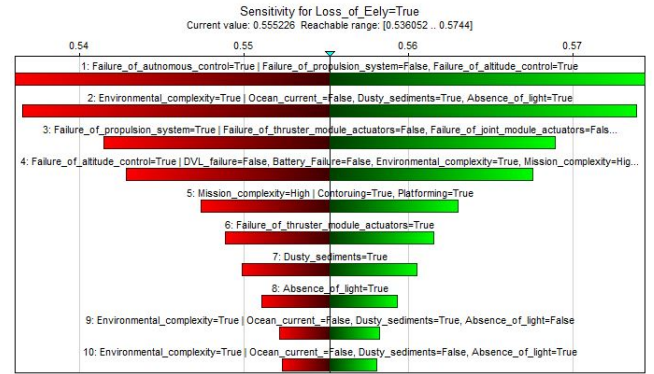

Figure 6. Sensitivity tornado diagram for losing Eely during Confined Environments Operations

environmental constraints. Therefore, our decision nodes could be as follows:

- D1 = a_s as the altitude set point
- D2 = v_s as the speed set point
- D3 = c_s as the control strategy
- D4 = s_c as the desired/optimum shape configuration

B. Online Reasoning

The DN continuously updates based on the sensory and temporal contexts. It is also important to include dwelling time based on the task to avoid rapid switching of states generated from sensor noise or in transient situations in-between state transitions. This can also help to avoid sensor outliers that bypassed the filtering process.

C. Hard Coding Safety/contingency Handling

This will impose predefined safety protocols that override the suggested control actions from the DN and perform strictly defined actions, such as Eely's preexisting safety functions, like collision avoidance.

V. DISCUSSION

From the results of the DBN and sensititity analysis, improving the robustness of the autonomous control part would significantly decrease the risk of losing Eely robot during different operations. Regarding the seabed mapping operations, from the sensitivity tornado graph in Figure 5 shows that improving the thruster module actuators and altitude control systems would also substantially reduce the risk of losing Eely. As for confined space operations, the sensitivity tornado graph in Figure 6 indicates that, except for environmental and mission complexity, improving the robustness of the thruster module actuators, propulsion system, and altitude control system would also significantly reduce the risk of losing Eely. The uncertainties associated with confined environments environmental complexity are reflected in the DBN in Figure 2 as they affect critical nodes, and in Tables VII - VIII as they are the main reason for a high rpn, mainly for DVL failure and Controller failure.

VI. CONCLUSION AND FUTURE WORK

In this paper, a BN model is developed for risk assessment of autonomous operations for Eely underwater snake robot. The model is populated with data to perform a specific quantitative probabilistic estimation of the loss of Eely during two challenging mission scenarios. The data is based on literature, PHA, and our own judgement based on similar systems. The results from the dynamic simulation and sensitivity analysis show that the highest risk of losing Eely was during confined environments operations, which is related to many factors, but the highest of them is the uncertainty of these environments compared to the other case scenario. In the future, this work can be build upon to include more mission scenarios. Also, implementing a behavior tree can allow for more complex mission scenarios and improve the modularity of Eely control systems [34] during different mission scenarios.

REFERENCES

[1] T. Dang, L. Lapierre, R. Zapata, B. Ropars, and G. Gourmelen, "A Dynamically Reconfigurable Autonomous Underwater Robot for Karst Exploration: Design and Experiment," *Sensors*, vol. 22, no. 9, p. 3379, 2022.

[2] A. J. Sørensen, M. Ludvigsen, P. Norgren, Ø. Ødegård, and F. Cottier, *Sensor-Carrying Platforms*. Cham: Springer International Publishing, 2020, pp. 241–275. [Online]. Available: https://doi.org/10.1007/978-3-030-33208-2_9

[3] X. Chen, N. Bose, M. Brito, F. Khan, B. Thanyamanta, and T. Zou, "A Review of Risk Analysis Research for the Operations of Autonomous Underwater Vehicles," *Reliability Engineering & System Safety*, vol. 216, p. 108011, 2021.

[4] Eelume AS, "Eelume - subsea intervention robots," https://eelume.com.

[5] NTNU Autonomous Underwater Vehicles Lab, "ROV/AUV Eely," https://www.ntnu.edu/aur-lab/rov/auv-eely.

[6] P. Liljebäck and R. Mills, "Eelume: A flexible and subsea resident IMR vehicle," in *OCEANS 2017 - Aberdeen*, 2017, pp. 1–4.

[7] J. E. Bremnes, P. Norgren, A. J. Sørensen, C. A. Thieme, and I. B. Utne, "Intelligent Risk-Based Under-Ice Altitude Control for Autonomous Underwater Vehicles," in *OCEANS 2019 MTS/IEEE SEATTLE*, 2019, pp. 1–8.

[8] I. B. Utne, A. J. Sørensen, and I. Schjølberg, "Risk Management of Autonomous Marine Systems and Operations," in *International conference on offshore mechanics and arctic engineering*, vol. 57663. American Society of Mechanical Engineers, 2017, p. V03BT02A020.

[9] M. Brito and G. Griffiths, "A Bayesian approach for predicting risk of autonomous underwater vehicle loss during their missions," *Reliability Engineering & System Safety*, vol. 146, pp. 55–67, 2016.

[10] G. Griffiths and M. Brito, "Predicting risk in missions under sea ice with Autonomous Underwater Vehicles," in *2008 IEEE/OES Autonomous Underwater Vehicles*, 2008, pp. 1–7.

[11] J. Hegde, I. B. Utne, I. Schjølberg, and B. Thorkildsen, "A Bayesian approach to risk modeling of autonomous subsea intervention operations," *Reliability Engineering & System Safety*, vol. 175, pp. 142–159, 2018.

[12] C. A. Thieme and I. B. Utne, "A risk model for autonomous marine systems and operation focusing on human–autonomy collaboration," *Proceedings of the Institution of Mechanical Engineers, Part O: Journal of Risk and Reliability*, vol. 231, pp. 446–464, 2017.

[13] J. E. Bremnes, C. A. Thieme, A. J. Sørensen, I. B. Utne, and P. Norgren, "A Bayesian Approach to Supervisory Risk Control of AUVs Applied to Under-Ice Operations," *Marine Technology Society Journal*, vol. 54, no. 4, pp. 16–39, 2020.

[14] T. Aven, "Practical implications of the new risk perspectives," *Reliability Engineering & System Safety*, vol. 115, pp. 136–145, 2013.

[15] ISO, "Iso 31000: Risk management-principles and guidelines," 2009.

[16] I. B. Utne, B. Rokseth, A. J. Sørensen, and J. E. Vinnem, "Towards supervisory risk control of autonomous ships," *Reliability Engineering & System Safety*, vol. 196, p. 106757, 2020.

[17] M. Krüger, J. Ziegler, and K. Heller, "A generic Bayesian Network for identification and assessment of objects in maritime surveillance," in *2012 15th International Conference on Information Fusion*, 2012, pp. 2309–2316.

[18] H. Yao, H. Wang, Y. Li, Y. Wang, and C. Han, "Research on Unmanned Underwater Vehicle Threat Assessment," *IEEE Access*, vol. 7, pp. 11387–11396, 2019.

[19] I. B. Utne and I. Schjølberg, "A Systematic Approach to Risk Assessment: Focusing on Autonomous Underwater Vehicles and Operations in Arctic Areas," ser. International Conference on Offshore Mechanics and Arctic Engineering, vol. Volume 10: Polar and Arctic Science and Technology, 2014.

[20] B. A. U. Jørgensen, "Methods for Visual Inspection and Mapping of Subsea Structures and Rough and Steep Underwater Terrain Using Articulated Underwater Robots," MSc dissertation, Norwegian University of Science and Technology, 2022.

[21] A. Lasbouygues, S. Louis, B. Ropars, L. Rossi, H. Jourde, H. Délas, P. Balordi, R. Bouchard, M. Dighouth, M. Dugrenot *et al.*, "Robotic mapping of a karst aquifer," in *IFAC: International Federation of Automatic Control*, 2017.

[22] B. Ropars, A. Lasbouygues, L. Lapierre, and D. Andreu, "Thruster's dead-zones compensation for the actuation system of an underwater vehicle," in *2015 European Control Conference (ECC)*. IEEE, 2015, pp. 741–746.

[23] A. Lasbouygues, L. Lapierre, D. Andreu, J. L. Hermoso, H. Jourde, and B. Ropars, "Stable and reactive centering in conduits for karstic exploration," in *2014 European Control Conference (ECC)*. IEEE, 2014, pp. 2986–2991.

[24] M. Rausand, *Risk assessment: theory, methods, and applications*. John Wiley & Sons, 2013, vol. 115.

[25] J. Tegdan, S. Ekehaug, I. M. Hansen, L. M. S. Aas, K. J. Steen, R. Pettersen, F. Beuchel, and L. Camus, "Underwater hyperspectral imaging for environmental mapping and monitoring of seabed habitats," in *OCEANS 2015 - Genova*, 2015, pp. 1–6.

[26] T. Dang, L. Lapierre, R. Zapata, B. Ropars, and P. Lepinay, "Over-Actuated Underwater Robots: Configuration Matrix Design and Perspectives," *Sensors*, vol. 21, no. 22, p. 7729, 2021.

[27] Ø. Hegrenæs, A. Ramstad, T. Pedersen, and D. Velasco, "Validation of a new generation DVL for underwater vehicle navigation," in *2016 IEEE/OES Autonomous Underwater Vehicles (AUV)*. IEEE, 2016, pp. 342–348.

[28] X. Liu, Y. Ju, X. Liu, S. Miao, and W. Zhang, "An IMU Fault Diagnosis and Information Reconstruction Method Based on Analytical Redundancy for Autonomous Underwater Vehicle," *IEEE Sensors Journal*, vol. 22, no. 12, pp. 12127–12138, 2022.

[29] H. OREDA, "Offshore and onshore reliability data," 2015.

[30] J. L. Casamayor, D. Su, and M. Sarshar, "Extending the lifespan of LED-lighting products," *Architectural Engineering and Design Management*, vol. 11, pp. 1–18, 2013.

[31] A. Khan, P. Widdop, A. Day, A. Wood, S. Mounce, and J. Machell, "Performance assessment of leak detection failure sensors used in water distribution systems," *J Water SRT - Aqua*, vol. 54, pp. 25–36, 2005.

[32] W. Adams, J. Blair, K. Bullock, C. Gardner, and L. Li, "Cost/benefit Analyses of a New Battery Pack Management Technique for Telecommunication Applications: Future Directions with Fuel Cell/Battery Systems," in *INTELEC 2004. 26th Annual International Telecommunications Energy Conference*. IEEE, 2004, pp. 73–82.

[33] BayesFusion, LLC, "GeNIe: A Tool for Graphical Decision-Analytic Modeling," https://support.bayesfusion.com/docs.

[34] C. I. Sprague, Özkahraman, A. Munafo, R. Marlow, A. Phillips, and P. Ögren, "Improving the Modularity of AUV Control Systems using Behaviour Trees," in *2018 IEEE/OES Autonomous Underwater Vehicle Workshop (AUV)*, 2018, pp. 1–6.

APPENDIX

Table VII
RELEVANT HAZARDS FOR SEABED MAPPING OPERATIONS OF EELY

Hazard	Hazardous Event	Cause	Consequence	Risk			
				Freq.	Conseq.	Detect.	Prod. (rpn)
Strong currents.	Currents are too strong for Eely to handle.	Currents are not accounted for in the mission plan.	Reduced mission duration. Reduced maneuverability in different configurations for Eely.	1 Low	2 Med	1 High	2
	Strong currents lead Eely to hit the seabed.	Eely is doing contouring for a steep area, wall.	Damage to Eely or one of its modules. Loss of Eely.	1 Low	3 High	2 Med	6
Contact with seabed.	Eely collides with seabed	Failure to detect the seabed. Failure to follow the safe distance between Eely and the seabed.	Damage to Eely or one of its modules. Loss of Eely.	1 Low	3 High	1 High	3
	Eely is stuck in soft sediment and algae in the seabed.	Failure to detect the seabed. Failure to detect algae or OOI. Failure to follow the safe distance between Eely and the seabed.	Damage to Eely or one of its modules. Loss of Eely.	1 Low	3 High	1 High	3
Power supply failure.	Eely losses its power supply	Short circuit in one of Eely's modules/sensors/thrusters. Lose cable. Water leakage. overheating of the batteries module.	Loss of Eely.	1 Low	3 High	2 Med	6
Propulsion system failure.	Thruster module failure	Wear of the thrusters blades. Failure of the electronic speed controller (ESC). Stucked algae and sediments over the thrusters/blades. Salt contamination over the thrusters	Loss of Eely.	1 Low	3 High	1 High	3
	Joint module failure	Wear of the mechanical components of the joint module. Wear of the joint module motors. Uncoordinated movements of the joint module. Leakage of oil from the cushions insulating the joint module.	Loss of Eely.	1 Low	3 High	2 Med	6
	Shape configuration failure	Uncoordinated movements of the joint module due to uncontrolled stiffness variance. Strong water pressure on the joint module.	Loss of Eely.	1 Low	3 High	3 Low	9
Controller failure.	Failure to supply the desired inputs to the thruster module and joint module. Failure to follow the safe distance between Eely and the seabed.	Software failure. Sensor failure. Hardware failure.	Loss of Eely. Reduced mission duration	2 Med	3 High	2 Med	12
	Failure to differentiate between contouring and platforming operations	Software failure. Sensor failure.	Inaccurate mapping of the seabed. Damage to Eely or one of its modules. Loss of Eely.	1 Low	3 High	1 High	3
DVL failure.	Failure to accurately detect the distance between Eely and the seabed.	Software failure. Sensor failure.	Inaccurate mapping of the seabed. Damage to Eely or one of its modules. Loss of Eely.	3 High	3 High	2 Med	18
	Poor detection of seabed features.	Software failure. Sensor failure.	Inaccurate mapping of the seabed. Reduced mission duration. Damage to Eely or one of its modules. Loss of Eely.	2 Med	1 Low	1 High	2
UHI failure.	Failure to accurately detect the distance between Eely and the seabed.	Software failure. Sensor failure.	Inaccurate mapping of the seabed. Reduced mission duration. Damage to Eely or one of its modules due to collision due to poor control decision of whether to map on a contouring or platforming manner.	1 Low	2 Mid	1 High	2
	Poor detection of seabed features.	Software failure. Sensor failure.	Inaccurate mapping of the seabed. Reduced mission duration. Damage to Eely or one of its modules due to collision due to poor control decision of whether to map on a contouring or platforming manner.	1 Low	2 Mid	1 High	2

Table VIII

RELEVANT HAZARDS FOR CONFINED ENVIRONMENTS OPERATIONS OF EELY

Hazard	Hazardous Event	Cause	Consequence	Risk			
				Freq.	Conseq.	Detect.	Prod. (rpn)
Strong currents.	Currents are too strong for Eely to handle.	Currents are not accounted for in the mission plan.	Reduced mission duration. Reduced maneuverability in different configurations for Eely.	1 Low	2 Med	1 High	2
	Strong currents lead Eely to hit the cave or tunnel.	Eely is doing contouring for the inside of a cave or tunnel.	Damage to Eely or one of its modules. Loss of Eely.	2 Med	3 High	2 Med	12
	Eely is stuck in soft sediment and algae in cave or tunnel.	Failure to detect the cave or tunnel. Failure to follow the safe distance between Eely and the inside of cave or tunnel. Loss of Eely	Damage to Eely or one of its modules. Loss of Eely.	2 Med	3 High	3 Low	18
Power supply failure.	Eely losses its power supply	Short circuit in one of Eely's modules/sensors/thrusters. Lose cable. Water leakage. overheating of the batteries module.	Loss of Eely.	1 Low	3 High	2 Med	6
Propulsion system failure.	Thruster module failure	Wear of the thrusters blades. Failure of the electronic speed controller (ESC). Stucked algae and sediments over the thrusters/blades. Salt contamination over the thrusters. High water pressure.	Loss of Eely.	1 Low	3 High	2 Med	6
	Joint module failure	Wear of the mechanical components of the joint module. Wear of the joint module motors. Uncoordinated movements of the joint module. High water pressure. Leakage of oil from the cushions insulating the joint module.	Loss of Eely.	1 Low	3 High	2 Med	6
	Shape configuration failure	Uncoordinated movements of the joint module due to uncontrolled stiffness variance. Strong water pressure on the joint module.	Loss of Eely.	1 Low	3 High	3 Low	9
Controller failure.	Failure to supply the desired inputs to the thruster module and joint module. Failure to follow the safe distance between Eely and the seabed.	Software failure. Sensor failure. Hardware failure.	Loss of Eely. Reduced mission duration	2 Med	3 High	2 Med	12
	Failure to differentiate between contouring and platforming operations	Software failure. Sensor failure.	Inaccurate mapping of the inside of cave or tunnel. Damage to Eely or one of its modules. Loss of Eely.	1 Low	3 High	1 High	3
DVL failure.	Failure to accurately detect the distance between Eely and the inside of cave or tunnel.	Software failure. Sensor failure.	Inaccurate mapping of the inside of cave or tunnel. Damage to Eely or one of its modules. Loss of Eely.	3 High	3 High	2 Med	18
UHI failure.	Failure to accurately detect the distance between Eely and the inside of cave or tunnel.	Software failure. Sensor failure.	Inaccurate mapping of the the inside of cave or tunnel. Reduced mission duration. Damage to Eely or one of its modules due to collision.	1 Low	2 Med	1 High	2
	Poor detection of the inside of cave or tunnel features.	Software failure. Sensor failure.	Inaccurate mapping of the the inside of cave or tunnel. Reduced mission duration. Damage to Eely or one of its modules due to collision.	1 Low	2 Med	1 High	2

Paper 2

Robust Altitude Controller for Underwater Snake Robot using Fractional Order PID Controller (FOPID)

Abdelrahman Sayed Sayed

Robust altitude controller for Underwater Snake Robot using Fractional Order PID Controller (FOPID)

Abdelrahman Sayed Sayed

Abstract—The growing interest in ocean discovery imposes a need for inspection and intervention in confined and demanding environments. Eely's slender shape, in addition to the ability to change its body configurations, makes the articulated underwater snake robot an adequate option for such environments. This paper presents an altitude controller of underwater snake robots based on a nonlinear Fractional Order PID (FOPID) controller. The proposed controller is evaluated through simulations to demonstrate its robustness and effectiveness in controlling the altitude of Eely underwater snake robot. The results show that the nonlinear FOPID controller is a promising solution for altitude control of underwater vehicles in various operational scenarios.

Index Terms—Altitude control; Eely; Underwater snake robots; Robot kinematics; PID; Fractional Order PID

I. Introduction

Autonomous underwater vehicles (AUVs) are considered to be efficient sensor-carrying platforms for seabed mapping and monitoring [1]. Eely articulated structure allows the vehicle to combine the functionality of several types of more conventional subsea vehicles and thereby cover a broad range of operational scenarios [2] as the vehicle can be configured to follow a torpedo-shaped AUV for platforming missions requiring the robot to map a big area or to vary the joint's module to follow snake configuration to map confined or steep environments which can't be achieved by a normal AUV.

Fractional calculus has emerged as an important tool in extending the ordinary calculus by introducing non-integer orders of derivatives and integrals [3]. This extension has enabled the development of fractional order controllers for various practical applications [4]. The Fractional Order PID controller (FOPID) includes parameters such as the integrator order λ and differentiator order μ, which have been shown to improve the performance of fractional dynamics. The application fields of fractional calculus are continually expanding, and it has found practical use in areas such as electrical engineering, automation and control engineering, robotics, biomedical engineering, and renewable energy domains [5], [6].

Recent advances in computer science and numerical tools have made fractional order operators and systems increasingly attractive for control applications due to their good

Abdelrahman Sayed Sayed is with Department of Marine Technology, Norwegian University of Science and Technology (NTNU), Otto Nielsens veg 10, 7491 Trondheim, Norway; Université de Toulon, Toulon, France. abdelrahman.s.s.e.ibrahim@ntnu.no, abdelrahman-ibrahim@etud.univ-tln.fr

performance and hereditary properties [7]. However, existing problems in altitude and motion control of underwater vehicles have prompted research into more effective control methods [8]. This paper introduces a simplified kinematic model of Eely underwater snake robot in a confined steep environment [9], along with an altitude controller that enables the robot to follow a specified sea mount and maintain a safe distance from the sea bed [10]. The paper proposes an effective altitude controller based on Fractional Order PID (FOPID) controller that provides better performance compared to conventional PID controllers. The FOPID controller gains are optimized using different tuning algorithms to adjust and correct the altitude for the Eely robot. The proposed controller is evaluated through simulations to demonstrate its robustness and effectiveness in controlling the altitude of the underwater snake robot.

The paper is structured as follows: Section II presents a simplified kinematic model of Eely underwater snake robot in II-A, the hydrodynamic model in II-B and the dynamic model in II-C. Section III present the two control methods applied to Eely, the nonlinear PID in III-A and the nonlinear FOPID in III-B. Section IV-A presents the altitude controller proposed in [11] applied to Eely. Section V details the simulation results and analysis. Lastly, section VI will present the concluding remarks with future directions.

II. Modeling of Underwater Snake Robots

A. Kinematic model of Eely

The position and orientation of a marine craft moving in six Degrees of Freedom (DOF) can be described using several reference frames. The most common reference frames for underwater vehicles are:

- North-East-Down (NED) frame $\{n\} = (x_n, y_n, z_n)$
- Body-fixed (BODY) frame $\{b\} = (x_b, y_b, z_b)$

Figure 1 illustrates the velocities in the BODY frame for Eely underwater vehicle. The generalized position and velocity coordinates are given by Equations 1 and 2 respectively:
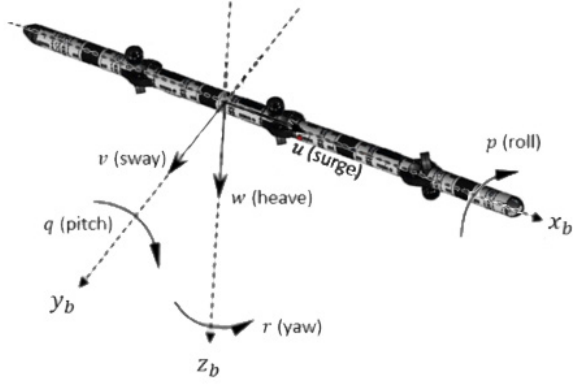
Fig. 1. Degrees of freedom for Eely Underwater Vehicle

$$\eta = [\eta_1^T \quad \eta_2^T]^T = [x \quad y \quad z \quad \phi \quad \theta \quad \psi]^T \quad (1)$$

$$\nu = [\nu_1^T \quad \nu_2^T]^T = [u \quad v \quad w \quad p \quad q \quad r]^T \quad (2)$$

In order to transform between the BODY and NED frames, a rotation matrix is used. A rotation matrix $\boldsymbol{R}$ is an element in *SO(3)*, which is the special orthogonal group of order 3, shown in Equation 3:

$$SO(3) := \left\{ \boldsymbol{R} \mid \boldsymbol{R} \in \mathbb{R}^{3 \times 3}, \ \boldsymbol{R}^{-1} = \boldsymbol{R}^\top, \det(\boldsymbol{R}) = 1 \right\} \quad (3)$$

The transformation between reference frames are based on the Euler angles of the vessel. These are roll (ϕ), pitch (θ) and yaw (ψ), they are defined as the orientation of the vehicle with respect to the NED frame. By using the Euler angles, it is possible to express the body fixed linear velocity vector, v_{nb}^b in the NED frame, according to the following Equation:

$$v_{nb}^n = R_b^n v_{nb}^b \quad (4)$$

where R_b^n is the rotation matrix from $\{b\}$ to $\{n\}$, $v_{nb}^n = \dot{p}_{nb}^n = [\dot{x}^n, \dot{y}^n, \dot{z}^n]$ is the velocity vector expressed in the NED-frame, and v_{nb}^n is the velocity vector expressed in the BODY-frame. R_b^n is calculated as:

$$R_b^n = R(\Theta_{nb}) = R_{z,\psi} R_{y,\theta} R_{x,\phi}$$
$$= \begin{bmatrix} c\psi c\theta & -s\psi c\phi + c\psi s\theta s\phi & s\psi s\phi + c\psi c\phi s\theta \\ s\psi c\theta & c\psi c\phi + s\phi s\theta s\psi & -c\psi s\phi + s\theta s\psi s\phi \\ -s\theta & c\theta s\phi & c\theta c\phi \end{bmatrix} \quad (5)$$

where Θ_{nb} is the vector containing the Euler angles.

Similarly, transformations can be carried out for the angular velocity. Let $w_{nb}^b = [p, q, r]^T$ be the BODY fixed angular velocities, and $T(\Theta_{nb})$ be the transformation matrix that relates BODY fixed angular velocities and Euler rates. The Euler rate vector $\dot{\Theta}_{nb}$ can be obtained as shown in Equation 6:

$$\dot{\Theta}_{nb} = T(\Theta_{nb}) w_{nb}^b \quad (6)$$

where,

$$T(\Theta_{nb}) = \begin{bmatrix} 1 & s\phi t\theta & c\phi t\theta \\ 0 & c\phi & -s\phi \\ 0 & \frac{s\phi}{c\theta} & \frac{c\phi}{c\theta} \end{bmatrix} \quad (7)$$

Incase of $\theta = 90°$, the robot would face a singularity. So, we avoid getting the joint angles to be exactly $90°$. Another possible solution to this problem is to use quaternions.

So, the 6-DOF kinematic equations becomes:

$$\dot{\eta} = J_\Theta(\eta)\nu \quad (8)$$

The Jacobian matrix that relates the linear and angular velocities in the NED frame and the BODY frame $J_\Theta(\eta)$ can be written as:

$$J_\Theta(\eta) = \begin{bmatrix} \dot{p}_{nb}^n \\ \dot{\Theta}_{nb} \end{bmatrix} = \begin{bmatrix} R(\Theta_{nb}) & 0_{3 \times 3} \\ 0_{3 \times 3} & T(\Theta_{nb}) \end{bmatrix} \begin{bmatrix} \nu_{nb}^n \\ w_{nb}^b \end{bmatrix} \quad (9)$$

where $\eta \in \mathbb{R}^6$ is the position and orientation in the NED frame, $J_\Theta(\eta) \in \mathbb{R}^{6 \times 6}$ is the Jacobian matrix that relates the linear and angular velocities in the NED frame and the BODY frame, and $\nu \in \mathbb{R}^6$ is the velocity in the BODY frame.

B. Hydrodynamics model of Eely

The hydrodynamic model of Eely combines linear and non-linear drag forces, added mass effect, fluid moments and current effect. The hydrodynamic model in Equation 10 is in closed-form to avoid numerical evaluations with drag forces [12] [13].

$$f = \begin{bmatrix} f_x \\ f_y \end{bmatrix} = \begin{bmatrix} f_{A_x} \\ f_{A_y} \end{bmatrix} + \begin{bmatrix} f_{D_x}^I \\ f_{D_y}^I \end{bmatrix} + \begin{bmatrix} f_{D_y}^{II} \\ f_{D_y}^{II} \end{bmatrix} \quad (10)$$

where f_{A_x} and f_{A_y} are the effects due to the added mass forces and are expressed as:

$$\begin{bmatrix} f_{A_x} \\ f_{A_y} \end{bmatrix} = - \begin{bmatrix} \mu (\boldsymbol{S}_\theta)^2 & -\mu \boldsymbol{S}_\theta \boldsymbol{C}_\theta \\ -\mu \boldsymbol{S}_\theta \boldsymbol{C}_\theta & \mu (\boldsymbol{C}_\theta)^2 \end{bmatrix} \begin{bmatrix} \ddot{\boldsymbol{X}} \\ \ddot{\boldsymbol{Y}} \end{bmatrix} - \\ \begin{bmatrix} -\mu \boldsymbol{S}_\theta \boldsymbol{C}_\theta & -\mu (\boldsymbol{S}_\theta)^2 \\ \mu (\boldsymbol{C}_\theta)^2 & \mu \boldsymbol{S}_\theta \boldsymbol{C}_\theta \end{bmatrix} \begin{bmatrix} \boldsymbol{V}_x^a \\ \boldsymbol{V}_y^a \end{bmatrix} \dot{\boldsymbol{\theta}} \quad (11)$$

where $\mu = diag(\mu_1, ..., \mu_n) \in \mathbb{R}^{nxn}$, $V_x^a = diag(V_{x,1}, ..., V_{x,n}) \in \mathbb{R}^{n \times n}$, $V_y^a = diag(V_{y,1}, ..., V_{y,n}) \in \mathbb{R}^{n \times n}$ and $[V_x, V_y]^T$ are the ocean current velocity expressed in the inertial frame, $S_\theta = diag(\sin \theta)^T \in \mathbb{R}^{n \times n}$ and $C_\theta = diag(\cos \theta)^T \in \mathbb{R}^{n \times n}$.

$f_{D_x}^I$ and $f_{D_y}^I$ are the linear drag effects, while $f_{D_x}^{II}$ and $f_{D_y}^{II}$ are the non-linear drag effects expressed in Equations 12 and 14:

$$\begin{bmatrix} f_{D_x}^I \\ f_{D_y}^I \end{bmatrix} = - \begin{bmatrix} c_t C_\theta & -c_n S_\theta \\ c_t S_\theta & c_n C_\theta \end{bmatrix} \begin{bmatrix} V_{r_k}^{link} \\ V_{r_y k}^{lin} \end{bmatrix} \quad (12)$$

$$\begin{bmatrix} f_{D_i}^{II} \\ f_{D_y}^{II} \end{bmatrix} = -\begin{bmatrix} c_t C_\theta & -c_n S_\theta \\ c_t S_\theta & c_n C_\theta \end{bmatrix} \mathrm{sgn}\left(\begin{bmatrix} V_{r_x}^{link} \\ V_{r_y}^{link} \end{bmatrix}\right) \\ \begin{bmatrix} \left(V_{r_x}^{link}\right)^2 \\ \left(V_{r_y}^{link}\right)^2 \end{bmatrix} \quad (13)$$

where $c_t = diag(c_{t,1}, ..., c_{t,n})$, $c_n = diag(c_{n,1}, ..., c_{n,n})$, while $V_{r_x}^{link}$ and $V_{r_y}^{link}$ are expressed as:

$$\begin{bmatrix} V_{r_x}^{\text{link}} \\ V_{r_y}^{\text{link}} \end{bmatrix} = \begin{bmatrix} C_\theta & S_\theta \\ -S_\theta & C_\theta \end{bmatrix}\begin{bmatrix} \dot{X} - V_x \\ \dot{Y} - V_y \end{bmatrix} \quad (14)$$

where $V_x = diag(V_{x,1}, ..., V_{x,n}) \in \mathbb{R}^{nxn}$ and $V_y = diag(V_{y,1}, ..., V_{y,n}) \in \mathbb{R}^{nxn}$ are the current velocities.

C. Dynamic model of Eely

The dynamic model of Eely is based on the forward dynamics algorithm proposed in [14]. The model also includes the effect of steady and uniform ocean current and motor and thruster forces.

III. CONTROL OF UNDERWATER SNAKE ROBOTS

During underwater inspections, Eely can be controlled by a human operator using a joystick. However, this can reduce the accuracy of the results due to less stable motion [15]. Path following can be a good choice for visual inspection and mapping, whether by following a pipeline or a lawnmower pattern. This can be achieved by defining multiple way-points along the path [16].

Path following can be accomplished by designing a line-of-sight guidance law [17]. This method relies on generating forward speed and changing the orientation of the vehicle based on the distance to the path. It's worth noting that path following is independent of time, which means there are no temporal constraints and no constraints on the commanded velocity of the vehicle. In some cases, such as paths with many sharp turns, it may be necessary to control the vehicle at a specific speed while moving along a curved path. In these situations, one can define a parameterized path that is time-dependent. The maneuvering problem becomes converging the position of the vehicle to the desired path and converging the speed of the vehicle to the desired speed [18].

A. Nonlinear PID Control

Let η_d denote the desired pose of the vehicle in the NED frame, which can be provided by a guidance law. The difference between the actual pose and the desired pose is represented by $e = \eta - \eta_d$. The control objective is to minimize e with a feedback loop that reaches the desired states. This can be accomplished with the following nonlinear Multiple Input Multiple Output (MIMO) PID control law:

$$\tau_c = -K_p J_\Theta^{-1} e - K_d J_\Theta^{-1} \dot{e} - K_i J_\Theta^{-1} \int_0^t e(t')\,dt' \quad (15)$$

where τ_c represents the control torque, J_Θ is the Jacobian matrix, K_p, K_d, and K_i are the proportional, derivative, and integral gain constants, respectively, e is the error between the reference signal and the system output, and $\dot{e}$ and $\int_0^t e(t')\,dt'$ represent the time derivative and the time integral of the error, respectively.

To achieve a more satisfactory response, a nonlinear PID controller has been developed. This controller replaces each term of the conventional PID controller with a nonlinear function $f(e)$, which is a combination of sign and exponential functions of the error signal [19]. The controller's derivative and integral are also modified using similar nonlinear functions and can be given as:

$$\begin{cases} U_{\text{NLPID}} = f_1(e) + f_2(e) + f_3\left(\int e\,dt\right) \\ f_i(\beta) = k_i(\beta)|\beta|^{\alpha_i}\,\mathrm{sign}(\beta) \\ k_i(\beta) = k_{i1} + \frac{k_2}{1+\exp(\mu_i \beta^2)}, i = 1,2,3 \end{cases} \quad (16)$$

where β could be e, $\dot{e}$, or $\int e\,dt$, $\alpha_i \in \mathbb{R}^+$, the function $K_i(\beta)$ is a positive function with coefficients $K_{i1}, K_{i2}, \mu_i \in \mathbb{R}^+$.

B. Nonlinear Fractional Order PID Controller (FOPID)

Fractional order PID (FOPID) controller was first introduced in [3]. Figure 2(a) shows a block diagram which represent the FOPID control structure.
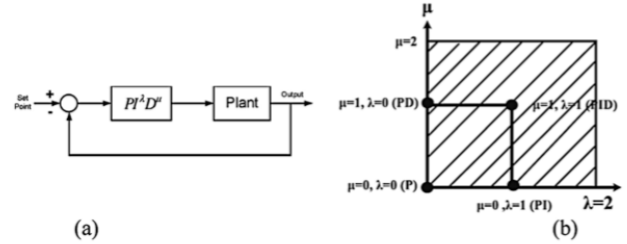

Fig. 2. FOPID controller block diagram and convergence graph

Figure 2(b) shows that by selecting $\lambda = 1, \mu = 1$, the nonlinear PID controller can be used. Using $\lambda = 1, \mu = 0$, and $\lambda = 0, \mu = 1$, is equivalent to PI PD controllers, respectively. These are all special cases for FOPID controller.

The nonlinear FOPID control law is expressed as:

$$\tau_c = -K_p J_\Theta^{-1} e - K_d J_\Theta^{-1} \dot{e}^\mu - K_i J_\Theta^{-1} \int_0^t \frac{e(t')\,dt'}{\lambda} \quad (17)$$

The difference between PID and FOPID controllers is that, FOPID provides extra degree of freedom not only for the controller gains (K_p, K_i, K_d) but also for the orders of integral λ and derivative μ [7]. FOPID will increase the disturbance rejection of the system especially that Eely is operating at a turbulent flow environment (water).

IV. ALTITUDE CONTROL AND TERRAIN FOLLOWING

In this section the altitude Control method for local sea floor geometry approximation from the DVL sensor measurements based on [20] and [21].

A. Altitude and Sea floor Gradient

Figure 3 shows Eely fully submerged above the seabed. Eely position in the $\{n\}$ frame is $p = [x_p, y_p, z_p]^T$
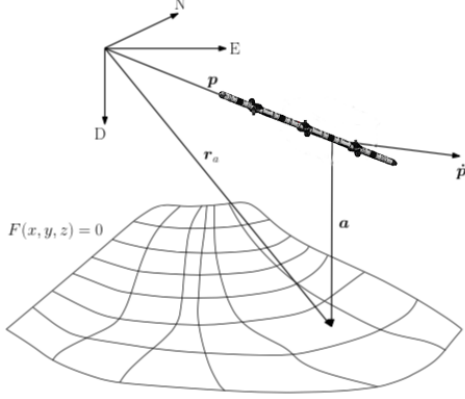

Fig. 3. Eely above the Seabed in the NED-frame. Adopted from [11]

The NED-frame velocity vector $\dot{p}$ can be expressed as:

$$\dot{p} = R_b^n(\Theta_{nb})v \tag{18}$$

where $\Theta_{nb} = [\phi, \theta, \psi]^T$ is the altitude vector, $R_b^n(\Theta_{nb})$ is the rotation matrix from $\{b\}$ to $\{n\}$ frame, and $v = [u, v, w]^T$ is the velocity vector in $\{b\}$ frame.

Seabead is assumed to be a surface expressed by the following equation:

$$F(x, y, z) = f(x, y) - z = 0, \quad \frac{\partial F}{\partial t} = 0 \tag{19}$$

The altitude is defined as the length of the vector from the center of origin (CO) of Eely to the point on the seabed with the same horizontal coordinates as the CO. Eely's depth z_p is the vertical distance from the sea surface to the CO of Eely. This should not be confused with the water depth or altitude. The altitude vector is expressed as:

$$a = r_a - p = \begin{bmatrix} x_p \\ y_p \\ f(x_p, y_p) \end{bmatrix} - \begin{bmatrix} x_p \\ y_p \\ z_p \end{bmatrix} = \begin{bmatrix} 0 \\ 0 \\ f(x_p, y_p) - z_p \end{bmatrix} \tag{20}$$

where r_a is is the NED position of the point on the seabed below the CO of Eely, as shown in Figure 3. The altitude length can be written as:

$$a = f(x_p, y_p) - z_p = F(x_p, y_p, z_p) \tag{21}$$

From Equation 21, the altitude can be expressed by the same function F as the seabed, when F is evaluated at Eely's position.

B. DVL Measurements

The DVL sensor is used to measure Eely's velocity over the seabed and to measure the altitude. DVL uses accoustic beams in a Janus configuration, these beams are transformed the DVL fixed frame $\{d\}$ to $\{b\}$ and finally to $\{n\}$.

The used DVL has 4 acoustic beams in a Janus configuration is proposed in order to decrease the influence of the vehicle inclination [11]. The DVL j^{th} beam with its paramters is shown in Figure 4a. The jth is represented by vector r_j^d expressed in Equation 22 and it goes from the DVL to the seabed.
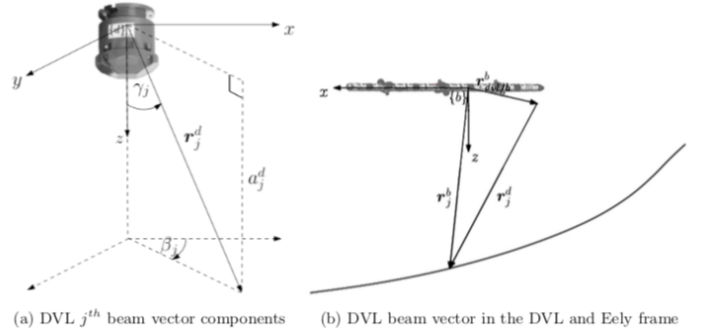

(a) DVL j^{th} beam vector components   (b) DVL beam vector in the DVL and Eely frame

Fig. 4. The DVL beam components and beam vectors in the DVL and Vehicle frame. Adopted from [11]

$$\boldsymbol{r}_j^d = \begin{bmatrix} x_j^d \\ y_j^d \\ a_j^d \end{bmatrix} = a_j^d \begin{bmatrix} \tan(\gamma_j)\cos(\beta_j) \\ \tan(\gamma_j)\sin(\beta_j) \\ 1 \end{bmatrix} \tag{22}$$

where γ_j is the angle of the jth beam from the DVL z-axis, and β_j is the angle from the DVL x-axis. a_d^j is the vertical component of r_d^j, and r_d^j is expressed in terms of a_d^j and the constant angles γ_j and β_j. a_d^j is the measurement output from the DVL, and the vector with all 4 altitude measurements is noted as a^d.

The vector r_d^j is transformed and shifted to $\{b\}$ frame in Equation 23, then transformed to $\{n\}$ frame in Equation 24. The first transformation and shift are illustrated in Figure 4b.

$$r_j^b = R_d^b(\Theta_{bd})r_j^d + r_{dvl/b}^b \tag{23}$$

$$r_j^n = R_b^n(\Theta_{nb})r_j^b \tag{24}$$

where Θ_{bd} is the orientation of $\{d\}$ relative to $\{b\}$. $r_{dvl/b}^b$ is the vector from CO of Eely to the DVL center in $\{b\}$ frame.

Finally, the 4 vectors from Eely CO to the seabed are given in $\{n\}$ as:

$$\boldsymbol{r}_j^n = \begin{bmatrix} x_j^n \\ y_j^n \\ a_j^n \end{bmatrix}, \quad j = 1, 2, 3, 4 \tag{25}$$

Equation 25 will be used to approximate the seabed geometry locally under Eely given that at least 3 DVL beams

measurements are available.

A linear approximation function of the seabed requires at least 3 points. The linear seabed function is $f(x,y) = a + bx + cy$. In case all of the 4 DVL beams measurements are available, 4 different approximations can be calculated by different combinations of 3 of 4 beams. But, only one of the approximations must be chosen. It is advised to use the combination which gives the most preview while going forward as the forward looking beam will give some collision avoidance feature [11]. The seabed approximation using 3 DVL beams is obtained by solving Equation 26 to compute a_j, b_j, c_j.

$$\begin{bmatrix} 1 & x_j^n & y_j^n \\ 1 & x_{j+1}^n & y_{j+1}^n \\ 1 & x_{j+2}^n & y_{j+2}^n \end{bmatrix} \begin{bmatrix} a_j \\ b_j \\ c_j \end{bmatrix} = \begin{bmatrix} a_j^n \\ a_{j+1}^n \\ a_{j+2}^n \end{bmatrix} \qquad (26)$$

V. SIMULATION RESULTS AND ANALYSIS

Simulations are carried out using Plankton open source simulator [22]. The simulator runs using Gazebo and UUV Simulator [23] plugin in ROS2. The two controllers were tested on Eely by maneuvering over a specified seamount as shown in Figure 5 while maintaining an altitude of 8.5 meters [10] from the seamount and to compare which controller had superior altitude regulation over the confined spaces in the seamount compared to the other.
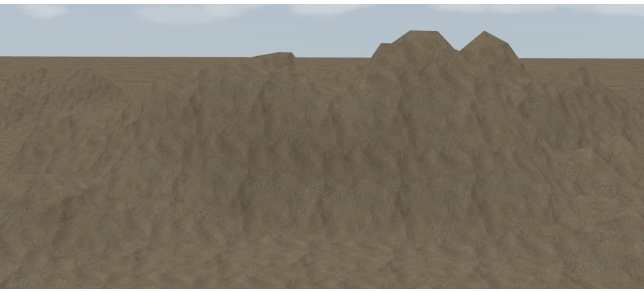

Fig. 5. Seamount to be mapped

Figure 6 shows the output results for Eely over the specified seamount for a period of 10 minutes with Proportional controller and PID controller.
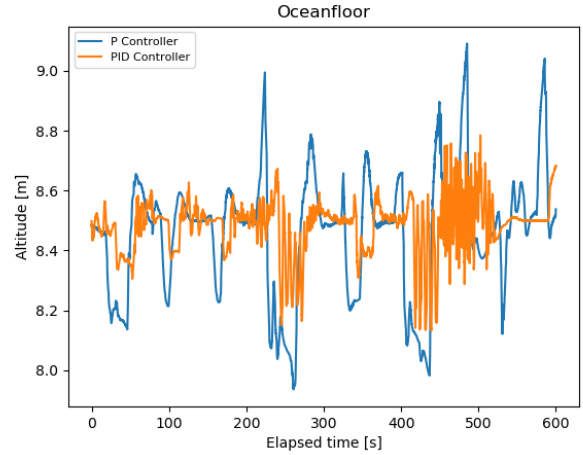

Fig. 6. Altitude control results with Proportional and PID controllers

Figure 7 shows the output results for Eely over the specified seamount for a period of 10 minutes with four different FOPID controllers.
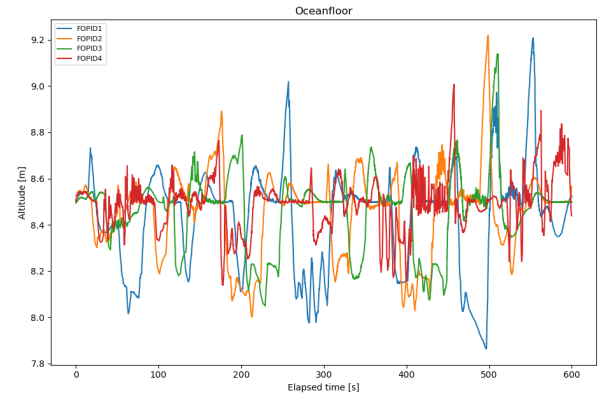

Fig. 7. Altitude control results with FOPID controllers

The performances of different controllers combined with the altitude controller for Eely and the tracking error for each controller are shown in Table I.

The nonlinear PID gave satisfactory performance with 20% error from the specified altitude. It is clearly evident that nonlinear FOPID had superior altitude regulation performance in confined environments with 1% error from the specified altitude for FOPID 4 controller. This was demonstrated in the simulation results, which showed Eely's ability to map a steep part of a seamount with greater detail and precision as shown in Figure 8 which gives a close look on Eely while mapping a steep part of the seamount.

TABLE I
PERFORMANCE COMPARISON OF CONTROLLERS AND ERROR

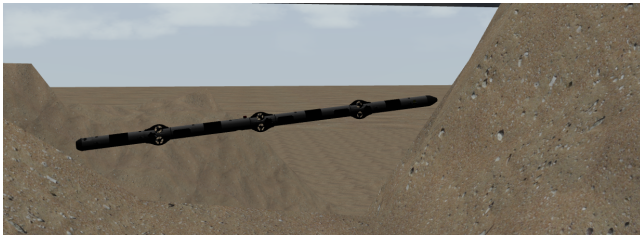| Controller	Controller Parameters					Error (%)
	Kp	Ki	Kd	lambda	mu	
Proportional	0.5	0	0	0	0	40
PID	0.5	0.2	0.05	1	1	20
FOPID 1	0.5	0.2	0.05	0.6	0.7	12
FOPID 2	0.5	0.2	0.05	0.4	0.7	5
FOPID 3	0.5	0.2	0.05	0.17	0.35	3
FOPID 4	0.5	0.2	0.05	0.2	0.6	1

Fig. 8. Eely mapping a confined part of the seamount with FOPID

VI. CONCLUSION

In this paper, a simulation model for the underwater snake robot Eely is proposed in order to analyze and visualize its behavior when subjected to various controllers. The main goal of the study is to enable the robot to perform visual mapping and investigation tasks. To achieve this, the necessary mathematical theory for modeling underwater snake robots was presented and an altitude controller model was designed and implemented. The developed model was then tested in a simulated environment using Gazebo and the UUV Simulator with ROS2 as the middleware. The results of the study are promising for the Fractional Order PID (FOPID) controller in regulating the altitude of Eely Underwater Snake Robot. Unlike classical PID controllers, FOPID controllers have five parameters that can be adjusted to optimize their performance. This flexibility allows them to achieve better results, particularly for higher order systems where classical PID controllers may struggle. Based on these findings, FOPID controllers can be recommend for achiving a robust altitude control of Underwater snake robots.

ACKNOWLEDGMENT

I would like to thank my previous bachelor thesis supervisor Hossam Hassan Ammar for his help with software implementation of FOPID, and my master thesis supervisor Asgeir J. Sørensen for his valuable comments on this paper.

REFERENCES

[1] A. Sørensen, M. Ludvigsen, P. Norgren-Aamot, Ødegård, and F. Cottier, *Sensor-Carrying Platforms*, 04 2020, pp. 241–275.

[2] P. Liljebäck and R. Mills, "Eelume: A flexible and subsea resident imr vehicle," in *Oceans 2017-Aberdeen*. IEEE, 2017, pp. 1–4.

[3] I. Podlubny, "Fractional-order systems and pi/sup /spl lambda//d/sup /spl mu//-controllers," *IEEE Transactions on Automatic Control*, vol. 44, no. 1, pp. 208–214, 1999.

[4] A. T. Azar, A. G. Radwan, and S. Vaidyanathan, *Mathematical techniques of fractional order systems*. Elsevier, 2018.

[5] D. B. Talange, S. D. Joshi, and S. Gaikwad, "Control of autonomous underwater vehicle using fractional order pi controller," in *2013 IEEE International Conference on Control Applications (CCA)*, 2013, pp. 1111–1116.

[6] H. H. Ammar, A. T. Azar, R. Shalaby, and M. I. Mahmoud, "Metaheuristic optimization of fractional order incremental conductance (foinc) maximum power point tracking (mppt)," *Complexity*, vol. 2019, pp. 1–13, 2019.

[7] H. H. Ammar and A. T. Azar, "Robust path tracking of mobile robot using fractional order pid controller," in *The International Conference on Advanced Machine Learning Technologies and Applications (AMLTA2019) 4*. Springer, 2020, pp. 370–381.

[8] K. Y. Pettersen, "Snake robots," *Annual Reviews in Control*, vol. 44, pp. 19–44, 2017.

[9] T. Dang, L. Lapierre, R. Zapata, B. Ropars, and G. Gourmelen, "A dynamically reconfigurable autonomous underwater robot for karst exploration: Design and experiment," *Sensors*, vol. 22, no. 9, p. 3379, 2022.

[10] Sture, M. Ludvigsen, F. Sreide, and L. M. S. Aas, "Autonomous underwater vehicles as a platform for underwater hyperspectral imaging," in *OCEANS 2017 - Aberdeen*, 2017, pp. 1–8.

[11] F. Dukan, "Rov motion control systems," PhD dissertation, Norwegian University of Science and Technology, 2014.

[12] E. Kelasidi, "Modeling, control and energy efficiency of underwater snake robots," PhD dissertation, Norwegian University of Science and Technology, 2015.

[13] E. Kelasidi, K. Y. Pettersen, J. T. Gravdahl, and P. Liljebäck, "Modeling of underwater snake robots," in *2014 IEEE International Conference on Robotics and Automation (ICRA)*, 2014, pp. 4540–4547.

[14] H. M. Schmidt-Didlaukies, A. J. Sørensen, and K. Y. Pettersen, "Modeling of articulated underwater robots for simulation and control," in *2018 IEEE/OES Autonomous Underwater Vehicle Workshop (AUV)*, 2018, pp. 1–7.

[15] G. Johnsen, M. Ludvigsen, A. Sørensen, and L. M. Sandvik Aas, "The use of underwater hyperspectral imaging deployed on remotely operated vehicles - methods and applications," *IFAC-PapersOnLine*, vol. 49, no. 23, pp. 476–481, 2016, 10th IFAC Conference on Control Applications in Marine SystemsCAMS 2016. [Online]. Available: https://www.sciencedirect.com/science/article/pii/S2405896316320390

[16] J. Mare, "Path following algorithm for minimally specified lawn-mower type auv missions," in *OCEANS'10 IEEE SYDNEY*, 2010, pp. 1–5.

[17] T. I. Fossen, "Handbook of marine craft hydrodynamics and motion control," 04 2021.

[18] R. Skjetne, T. I. Fossen, and P. V. Kokotović, "Robust output maneuvering for a class of nonlinear systems," *Automatica*, vol. 40, no. 3, pp. 373–383, 2004. [Online]. Available: https://www.sciencedirect.com/science/article/pii/S0005109803003467

[19] A. A. Najm and I. K. Ibraheem, "Nonlinear pid controller design for a 6-dof uav quadrotor system," *Engineering Science and Technology, an International Journal*, vol. 22, no. 4, pp. 1087–1097, 2019. [Online]. Available: https://www.sciencedirect.com/science/article/pii/S2215098618318846

[20] F. Dukan and A. J. Sørensen, "Altitude estimation and control of rov by use of dvl," *IFAC Proceedings Volumes*, vol. 45, no. 27, pp. 79–84, 2012, 9th IFAC Conference on Manoeuvring and Control of Marine Craft. [Online]. Available: https://www.sciencedirect.com/science/article/pii/S1474667016312083

[21] F. Dukan and A. Sørensen, "Sea floor geometry approximation and altitude control of rovs," *Control Engineering Practice*, vol. 29, pp. 135–146, 2014. [Online]. Available: https://www.sciencedirect.com/science/article/pii/S0967066114001312

[22] Liquid.ai, "Plankton." [Online]. Available: https://github.com/Liquid-ai/Plankton

[23] M. M. M. Manhães, S. A. Scherer, M. Voss, L. R. Douat, and T. Rauschenbach, "UUV simulator: A gazebo-based package for underwater intervention and multi-robot simulation," in *OCEANS 2016 MTS/IEEE Monterey*. IEEE, sep 2016. [Online]. Available: https://doi.org/10.1109%2Foceans.2016.7761080

A - Simulation Parameters

Parameter	Value	Unit	Description
N	5	$[-]$	Number of links
r	12	$[-]$	Number of thrusters
r_i	0.1	$[\text{m}]$	Radius of each link
l_1	494	$[\text{mm}]$	Length of link 1
l_2	1185	$[\text{mm}]$	Length of link 2
l_3	1435	$[\text{mm}]$	Length of link 3
l_4	1185	$[\text{mm}]$	Length of link 4
l_5	740	$[\text{mm}]$	Length of link 5
l_j	286	$[\text{mm}]$	Length of joint module
m	199	$[\text{kg}]$	Total dry mass
r_{bbi}^b	$(0, 0, 0.025)$	$[\text{m}]$	Distance from CO to CB
ρ	1025	$\left[\frac{\text{kg}}{\text{m}}\right]$	Density of sea water
C_D	0.3	$[-]$	Drag coefficient
v_{ref}	1	$[-]$	Reference velocity
β	0.1	$[-]$	Linear drag parameter in surge
γ	0.2	$[-]$	Linear drag parameter in roll
$\frac{\alpha}{3}$	0.0003	$[-]$	Ratio of thruster model parameters
C_t	0.5	$[-]$	Proportionality constant
γ	0.2	$[-]$	Linear drag parameter in roll
desired altitude	8.5	$[-]$	Distance between the robot and seabed
l_x	0.3	$[m/s]$	Linear velocity in x-direction
l_y	0.3	$[m/s]$	Linear velocity in y-direction
l_z	0.5	$[m/s]$	Linear velocity in z-direction
K_p	0.5	$[-]$	Proportional gain
K_i	0.2	$[-]$	Integral gain
K_d	0.05	$[-]$	Derivative gain
μ	0.6	$[-]$	Order of differentiation
λ	0.2	$[-]$	Order of integration
DVL sensor	10	$[Hz]$	DVL refresh rate

Table A.1: Simulation parameters of Eely